

**Influence of Structure and UV-Light
Absorption on the Electrical
Conductivity of TiO₂ and Comparison
with its Catalytic Activity**

Von der Naturwissenschaftlichen Fakultät
der Universität Hannover
zur Erlangung des Grades eines

Doktors der Naturwissenschaften

– Dr. rer. nat. –

genehmigte Dissertation

von

Lic. Quím. Roger Amade Rovira

geboren am 24. Oktober 1979 in Barcelona

2006

Referent: Prof. Dr. P. Heitjans

Korreferent: Prof. Dr. D. Hesse

Tag der Promotion: 2. Februar 2006

Erklärung an Eides statt

Hiermit erkläre ich, dass ich die vorliegende Arbeit selbstständig verfasst und nur unter Verwendung der angegebenen Quellen und Hilfsmittel angefertigt habe. Die Dissertation ist nicht schon als Diplomarbeit oder ähnliche Prüfungsarbeit verwendet worden.

Hannover, im November 2005

Roger Amade Rovira

*a la meva mare, Rosa-Hilda,
i a les meves germanes,
Marta, Diana i Sandra*

Abstract

The changes in the electrical properties of titanium dioxide upon high-energy ball milling and UV-light absorption have been studied by means of impedance spectroscopy.

The conductivity of the milled samples (rutile and anatase) was measured under oxygen atmosphere and vacuum in a temperature range from 298 K to 1073 K. The variations in the conductivity and activation energy of the conduction processes upon milling can be understood as a result of a phase transition near the surface of the grains. The effect of UV-light absorption on the surface conductivity of a titanium dioxide single crystal (rutile) was studied under oxygen and nitrogen atmospheres in a temperature range from 298 K to 573 K. Analogously to high-energy ball milling, the effect of UV-light absorption on the conductivity of the crystal can be explained by a photoinduced phase transition near the surface at about 475 K.

These results are compared with measurements of the catalytic activity of titanium dioxide under similar conditions. Both kinds of measurements, conductivity and catalytic activity measurements, correlate with each other and are in good agreement with the assumption mentioned above.

Keywords: Titanium dioxide, Impedance Spectroscopy, Photoconductivity

Kurzfassung

Die Änderungen der elektrischen Eigenschaften von Titandioxid, die durch Kugelmahlen und Absorption von UV-Licht hervorgerufen werden, sind mit der Impedanzspektroskopie untersucht worden.

Die Leitfähigkeit der gemahlenden TiO_2 -Proben (Rutil und Anatas) wurde unter Sauerstoffatmosphäre und im Vakuum in einem Temperaturbereich von 298 K bis 1073 K gemessen. Die Leitfähigkeitsänderungen und die Änderungen der Aktivierungsenergie der Leitungsprozesse lassen sich als eine Phasenumwandlung in der Nähe der Oberfläche der TiO_2 -Körner erklären. Der Einfluß von UV-Licht auf die Leitfähigkeit eines Rutil-Einkristalls wurde unter Sauerstoff- und Stickstoffatmosphäre in einem Temperaturbereich von 298 K bis 573 K studiert. Analog zum Kugelmahlen können die auftretenden Leitfähigkeitseffekte im Falle des Einkristalls durch eine photoinduzierte Phasenumwandlung in der Nähe der Oberfläche bei etwa 475 K erklärt werden.

Die Ergebnisse wurden mit Daten zur katalytischen Aktivität von Titandioxid unter ähnlichen Bedingungen verglichen. Beide Ergebnisse, die der Leitfähigkeitsmessungen und der Untersuchungen zur katalytischen Aktivität, korrelieren miteinander und sind in guter Übereinstimmung mit der oben erwähnten Annahme.

Schlagerworte: Titandioxid, Impedanzspektroskopie, Fotoleitfähigkeit

There are trivial truths and the great truths.
The opposite of a trivial truth is plainly false.
The opposite of a great truth is also true.

(Niels Bohr, 1885 – 1962)

The only laws of matter are those that our minds must fabricate and the
only laws of mind are fabricated for it by matter.

(James Clerk Maxwell, 1831 – 1879)

Contents

1	Introduction	1
1.1	Applications of titanium dioxide	1
1.2	Motivation	1
2	Fundamentals	3
2.1	Nanocrystalline materials	3
2.2	Dielectric relaxation	5
2.3	Impedance spectroscopy	9
2.3.1	Modulus and impedance representation	12
2.3.2	Models	15
2.4	Defect chemistry of TiO ₂	17
2.5	Surface conductivity	19
2.6	Photoconductivity	21
2.7	Heterogeneous catalysis	26
3	Materials and sample preparation	31
3.1	Titanium dioxide TiO ₂	31
3.2	High-energy ball milling	35
3.3	Sample preparation	36
4	Characterization	39
4.1	X-ray diffraction	39
4.2	Transmission electron microscopy	45
4.3	BET surface area	45
4.4	Thermal analysis	47
4.5	X-ray photoelectron spectroscopy	48
4.6	Electron paramagnetic resonance spectroscopy	49

4.7	Scanning electron microscopy	51
4.8	Density	52
5	Experimental setup	55
5.1	Equipment for impedance spectroscopy	55
5.2	Equipment for photoconductivity and surface conductivity . .	57
6	Results	61
6.1	Conductivity of micro-and nanocrystalline TiO ₂	61
6.1.1	Microcrystalline rutile	61
6.1.2	Microcrystalline anatase	66
6.1.3	Nanocrystalline anatase	70
6.2	Surface conductivity of TiO ₂ single crystal	74
6.2.1	Influence of atmosphere	75
6.2.2	Influence of temperature and measuring frequency . . .	75
6.3	Photoconductivity of TiO ₂ single crystal	77
6.3.1	Influence of atmosphere	77
6.3.2	Influence of time	78
6.3.3	Influence of temperature	80
6.3.4	Influence of light intensity	82
7	Discussion	85
7.1	Influence of milling time in micro- and nanocrystalline TiO ₂ .	85
7.2	Influence of illumination in TiO ₂ single crystal	89
7.3	Comparison with catalytic activity	90
8	Conclusion and outlook	95
A	Measurement bridge	97
B	Conductivity of Ta_xTi_(1-x)X₂, X = S, Se	101
C	List of publications and conferences	107
	Bibliography	109
	Curriculum vitae	117

Acknowledgment

I would like to express my deep gratitude to my advisor Herrn Prof. Dr. P. Heitjans for giving me the chance to work in such an interesting and promising material as it is titanium dioxide. I would also like to thank him for his support and attention throughout my work and for useful recommendations.

I would also like to express my deep gratitude to Herrn Prof. Dr. D. Hesse for his supervision and for very stimulating discussions related to titanium dioxide and photocatalysis.

I would like to thank Dr. S. Indris for his support and helpfulness in many different issues of my work, and for the BET and XRD measurements.

I thank Andreas Haeger and Mina Finger for their measurements on the catalytic activity of titanium dioxide, for their helpfulness and for several exciting discussions on the photocatalytical properties of TiO₂.

I thank Dr. S. Dultz for his supervision during the DSC/DTA measurements.

I thank Dr. A. Feldhoff for the SEM images, Dr. Grünert for the XPS measurements and Dr. Börger for the EPR measurements.

I thank Dr. Christian Kübel (FEI Company, Eindhoven) for the TEM micrographs.

I would also like to thank all the staff of the mechanical workshop; Mr. Bieder, Mr. Egly and Mr. Becker who helped me on constructing the photoconductivity cell, as well as to Herrn Rogge, from the electrical workshop, for his help with the UV-light source and with technical problems.

I wish to thank Dr. M. Wilkening and Muayad Masoud for plenty of scientific discussions and their helpfulness throughout my work.

I am also thankful to all the staff of the Institut für Physikalische Chemie und Elektrochemie for their help in many problems and questions.

Finally, my highest appreciation is addressed to my family, who helped me and motivated me in all circumstances.

Roger Amade

Chapter 1

Introduction

1.1 Applications of titanium dioxide

Titanium dioxide has a wide variety of different uses in everyday life. It is, for example, the most important constituent of paint, it is used for coloring food and cosmetics, and for sun-protection cremes.

There is a vast amount of literature about TiO_2 due to its applications as a catalyst, photocatalyst, photoanode in solar cells and gas sensor among others [1–8].

As a catalyst it is used, for instance, for the clean-up of waste-gas in power generating plants and motor vehicles, and for the production of organic products by means of selective oxidation processes. The wide band-gap (~ 3 eV) combined with the high oxidation potential of the valence bond enables titanium dioxide to oxidize virtually any organic molecule under absorption of UV light, *i.e.*, at wavelengths below 390 nm.

1.2 Motivation

Despite the large amount of literature available about the defect chemistry [9–27], surface science [28–34] and catalytic properties [1–4] of titanium dioxide some of its properties are not yet well understood. Particularly, the influence of temperature on the catalytic activity for the photocatalytic total oxidation of hydrocarbon species in the gas phase is unclear. From the experimental results it is reasonable to assume that the surface of the catalyst is changed under reaction conditions [35, 36]. However, this supposition is in

1.2 Motivation

disagreement with the usual mechanisms proposed in the literature [2].

Since the electrical conductivity of TiO_2 strongly depends on the stoichiometry of the material, impedance spectroscopy may help to prove the mentioned hypothesis.

Besides, in recent years, nanocrystalline materials are being intensively investigated due to their exceptional properties. Because of their small crystallite size, *i.e.*, large surface area, they show an increased catalytic activity relative to the coarse grained material. During the preparation of nanocrystalline materials, the structure of the catalyst may change affecting its performance. Modifications in the structure of the material may imply changes in the electrical properties of the solid, which can be analyzed by means of impedance spectroscopy.

A wide amount of work is available in the literature about the electrical properties and defects in TiO_2 [9–27]. However, most measurements are done at elevated temperatures (> 973 K) and oxygen partial pressures below one atmosphere. On the other hand, many studies on the photoelectrical properties of titania are concerned with thin films due to its applications in solar cells (see, *e.g.*, [37–40]) and gas sensing [6–8]. However, the photoconductivity of titanium dioxide has not been extensively studied up to now [3, 41]. Hence, there is a lack of measurements of the electrical properties of micro- and nanocrystalline TiO_2 powders under catalytic conditions, *i.e.*, temperatures between 298 K and 573 K, and oxygen partial pressures of about one atmosphere. Furthermore, there is also a lack of measurements on the photoconductivity of titanium dioxide under catalytic conditions.

Therefore, the aim of this work is to study the effect of UV-light absorption and the structure of the material under catalytic conditions on the electrical properties of titanium dioxide, and to correlate the obtained results with measurements of the catalytic activity done in cooperation with the Institut für Technische Chemie (University of Hannover) [35].

Chapter 2

Fundamentals

2.1 Nanocrystalline materials

Nanocrystalline materials are polycrystalline solids with an average grain size of some nanometers, typically 5 nm to 50 nm. The grains are surrounded by a network of interfaces, *i.e.* grain boundaries and pore surfaces (Figure 2.1) which exhibit short range order rather than long range order or periodicity as in the bulk region. Thus, these solids have a heterogeneously distributed disorder [42] due to the alternation of regions with periodicity (crystals) with regions with disorder (grain boundaries). The average width of the interfaces is often estimated to be in the range from 0.5 nm to 1 nm, which may lead to a volume fraction of grain boundaries as high as 50 % [43]. The volume fraction of pores in these materials can be as high as 20 % for ceramics to less than 5% for metals [44]. This porosity can be removed by sintering the material at elevated temperatures and pressures without resulting in a significant grain growth [45].

Nanocrystalline materials often present quite different properties from those of conventional materials that have grain structures on a coarser size scale [46]. The differences occur, in general, due to a larger volume fraction of grain boundaries. In many instances, diffusion in grain boundaries is orders of magnitude higher than the corresponding bulk diffusion [47–51]. This is due to the high level of disorder and high mobilities in the grain boundary regions. For crystallites smaller than about 10 nm quantum effects may play an important role and lead to an increase of the band gap. As a consequence, a blue shift of the absorption edge is observed as in, *e.g.*, nanocrystalline

2.1 Nanocrystalline materials

TiO₂ [1]. Due to the small size of the crystallites and the large fraction of grain boundaries some of these materials exhibit new electrical, magnetic, optical, mechanical, thermodynamic and catalytic properties [52–54].

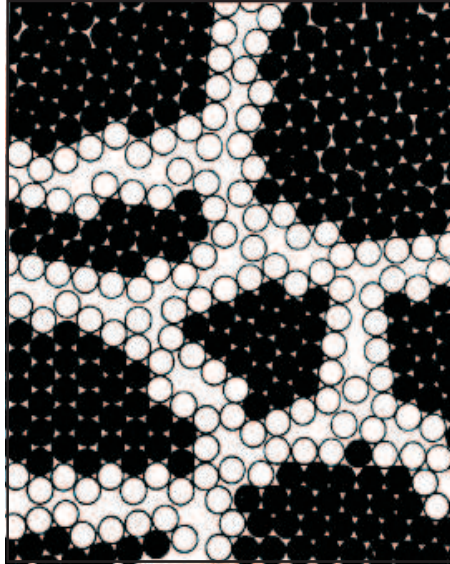


Figure 2.1: Sketch of a nanocrystalline material [52]. Open circles represent atoms in grain boundary regions and black circles atoms inside the crystals.

Synthesis

The physical and chemical properties of nanocrystalline materials depend on the shape, size and distribution of the particles and pores that form their structure [49]. Many of these parameters may be controlled by varying the process of synthesis and thus, desired structural characteristics may be tailored.

Several methods are used to obtain nanocrystalline materials. These can be divided into two groups [44]: On the one hand, methods which are based on the cluster assembly of atoms, such as chemical vapor synthesis (CVS), sol-gel processing or gas-phase synthesis. On the other hand, methods based on mechanical attrition of the coarse grained material are also used.

One of the synthesis processes that is based on mechanical attrition is high energy ball milling (see, *e.g.*, [55]). This preparation method will be explained in Section 3.2.

2.2 Dielectric relaxation

An ideal dielectric is a substance in which there exist only bound charges (electrons, ions) and therefore the dc conductivity is zero. When an ideal dielectric is placed in an electric field between the plates of a capacitor, two electric polarizations take place (Figure 2.2) [56]:

- Displacement polarization: the electrons and ions are displaced from their equilibrium positions inducing a dipole moment in each atom or between ion pairs.
- Orientational polarization: in molecular dielectrics the dipoles are preferably oriented in the direction of the field.

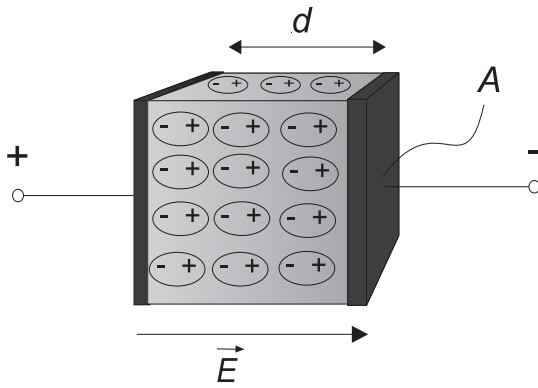


Figure 2.2: A dielectric under the action of an external electric field. \vec{E} is the macroscopic electric field, A is the area of the capacitor plates and d is the distance between the plates.

The induced dipole moments create an internal field \vec{E}_P in opposite direction to the external electric field. The resulting mean internal field is called the macroscopic electric field \vec{E} and is given by

$$\vec{E} = \vec{E}_0 - \vec{E}_P = \frac{\vec{E}_0}{\epsilon_r}, \quad (2.1)$$

where \vec{E}_0 is the electric field present between the plates of the capacitor when the dielectric is replaced by vacuum and the charge Q at the plates is not changed. ϵ_r is the relative permittivity or dielectric constant of the material.

The charge Q per unit area deposited on the electrodes is called the electric displacement \vec{D} and consists of the sum of the displacement charge in vacuum and the displacement due to polarization processes (Equation 2.2).

2.2 Dielectric relaxation

$$\vec{D} = \epsilon_0 \epsilon_r \vec{E} = \epsilon_0 \vec{E} + \vec{P} = \epsilon_0 \vec{E} + \epsilon_0 (\epsilon_r - 1) \vec{E}. \quad (2.2)$$

Here \vec{P} is the polarization of the dielectric, defined as dipole moment \vec{p} per unit volume:

$$\vec{P} = \frac{d\vec{p}}{dV} = (\epsilon_r - 1) \epsilon_0 \vec{E} = \chi \epsilon_0 \vec{E} \quad (2.3)$$

χ is the dielectric susceptibility of the material.

Under the action of an alternating field several processes occur in the dielectric:

- The displacement polarization leads to electric oscillations which follow the electric field almost immediately. The resonant frequencies of this process are 10^{15} to 10^{14} Hz for the electronic and 10^{13} to 10^{12} Hz for the ionic polarization.
- The orientational polarization leads to a retarded response and this process is called *dielectric relaxation*. The response is described by a characteristic time constant τ (the relaxation time) which is strongly temperature dependent. For crystals at room temperature the relaxation times are of the order of 10^{-11} to 10^{-9} s. However, in amorphous solids and polymers it may take some seconds or even hours, days and years, depending on temperature.
- Real dielectrics contain charge carriers which can be moved under the action of an external electric field. These processes are called *charge-carrier relaxations* or also *conductivity relaxations*. The relaxation time τ_c of a conductivity relaxation is given by

$$\tau_c = \frac{\epsilon_0 \epsilon_r}{\sigma_{dc}}, \quad (2.4)$$

where σ_{dc} is the dc conductivity of the material.

One can now rewrite Equation (2.2) as:

$$\vec{D} = \epsilon_0 \epsilon_r \vec{E} = \epsilon_0 \vec{E} + \epsilon_0 (\epsilon_\infty - 1) \vec{E} + \epsilon_0 (\epsilon_r - \epsilon_\infty) \vec{E} = \vec{D}_{Vac} + \vec{P}_{Res} + \vec{P}_{Rel}. \quad (2.5)$$

ϵ_∞ is the relative "high frequency" permittivity or unrelaxed permittivity. It is present nearly immediately after switching on the electric field or at very

2.2 Dielectric relaxation

high frequencies (infrared and optical), where the relaxation processes cannot follow the field changes. \vec{D}_{Vac} , \vec{P}_{Res} and \vec{P}_{Rel} are the vacuum contribution, the resonance contribution and the relaxation contribution to the electric displacement, respectively.

The limit $\epsilon_r(t \rightarrow \infty)$ is called the static permittivity ϵ_s and the static polarization is

$$\vec{P}_{\text{Rel,s}} = \epsilon_0 \Delta\epsilon \vec{E}. \quad (2.6)$$

Here, $\Delta\epsilon = \epsilon_s - \epsilon_\infty$ is called the relaxation strength. Equation 2.6 describes the polarization for a single relaxation process. In general, there are more than one relaxation processes in a given material, and the parameters ϵ_s , ϵ_∞ and $\Delta\epsilon$ have to be specified separately for each process.

Debye model

Consider a system consisting of a certain number of non-interacting dipoles. If a step-function field is applied to the system, there will be some delay between the polarization and the field. One may assume that the time-dependent response of the polarization under such an excitation is described by a simple exponential function. The response of the polarization to an arbitrarily time-varying field $E(t)$ may be expressed by the convolution integral [56]

$$P(t) = \epsilon_0 \int_0^\infty f(\tau) E(t - \tau) d\tau \quad (2.7)$$

where $f(t)$ is the dielectric response function. Applying the convolution theorem [57] to Equation (2.7) one has

$$P(\omega) = \epsilon_0 \tilde{\chi}(\omega) E(\omega). \quad (2.8)$$

The real and imaginary parts of this function are

$$\chi' = \chi(0) \frac{1}{1 + \omega^2 \tau^2}, \quad (2.9)$$

$$\chi'' = \chi(0) \frac{\omega \tau}{1 + \omega^2 \tau^2}. \quad (2.10)$$

Here $\chi(0)$ is the value of the static dielectric susceptibility ($\omega = 0$) and τ the time constant of the process. Figure 2.3a shows a schematic representation of the frequency dependency of the real and imaginary parts of

2.2 Dielectric relaxation

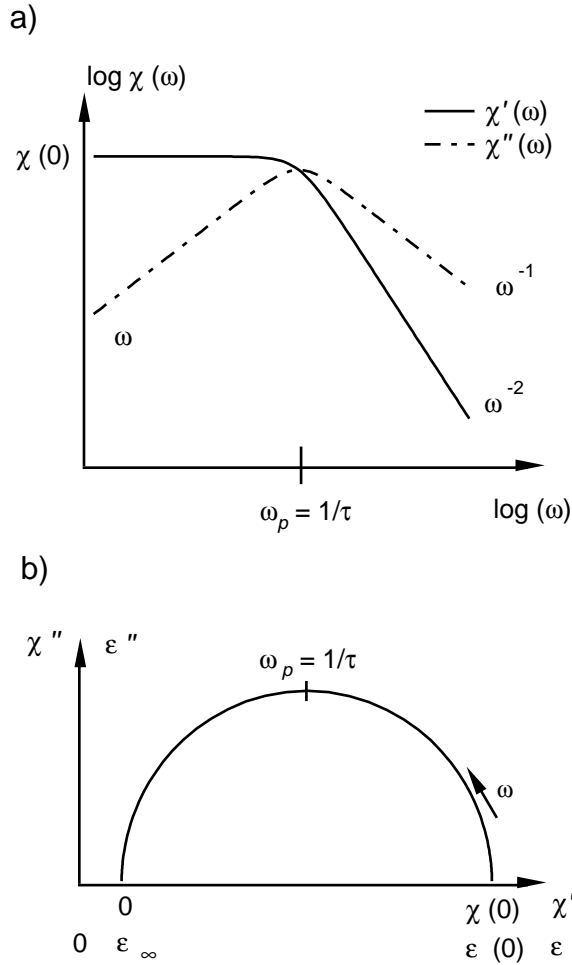


Figure 2.3: Frequency dependence of the real and imaginary components of the dielectric susceptibility (a) and complex plane representation of the dielectric susceptibility (b) of an ideal Debye system. The arrow in diagram (b) indicates the direction of increasing frequency.

the dielectric susceptibility, whereas Figure 2.3b shows the complex plane representation of this function.

This is the same result as that obtained for a circuit consisting of a capacitance C_∞ , which describes the resonant processes, in parallel with a capacitance and resistance in series which describe the dielectric relaxation of the dipoles.

In practice, the Debye behavior is observed in very few systems. It is often found, that the Debye peak, which appears in Figure 2.3a, is considerably broadened over its theoretical full width at half height (FWHM) of 1.144 decades, and the semicircle in Figure 2.3b is depressed so that its center lies below the real axis. A number of empirical relaxation functions have

2.3 Impedance spectroscopy

been proposed to parameterize these observations [58], usually interpreted in terms of a distribution of relaxation times.

2.3 Impedance spectroscopy

Impedance spectroscopy allows the study of the electrical phenomena occurring in the bulk and at the interfaces of a system. This is possible due to the different dynamics that govern in these regions.

An alternating voltage \tilde{U} is applied to the sample and the alternating current \tilde{I} generated is measured. A small excitation is used in order to obtain a linear response. This means that the frequency of the voltage and of the current generated are the same. The impedance \tilde{Z} is given by the following equation:

$$\tilde{Z} = \frac{\tilde{U}}{\tilde{I}} = Z' + iZ'' = Z_0 \cdot \exp(i\theta), \quad (2.11)$$

where Z' and Z'' are the real and the imaginary part of the impedance, respectively, and $i = \sqrt{-1}$. Z_0 is the magnitude of the impedance and θ the phase shift between the excitation and the response (Figure 2.4).

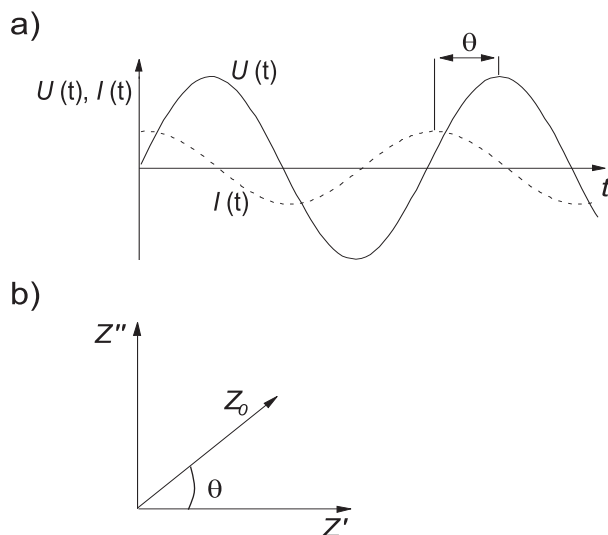


Figure 2.4: Representation of an alternating voltage and the corresponding generated current with a phase shift of θ (a). Impedance Z in the complex plane (b).

Other magnitudes related to the impedance provide further information

2.3 Impedance spectroscopy

Table 2.1: Relation between the impedance and other dielectric functions

Magnitude	Relation
Admittance	$\tilde{Y} = \tilde{Z}^{-1}$
Dielectric constant	$\tilde{\epsilon}_r = \tilde{Y}\mu^{-1}$
Modulus	$\tilde{M} = \mu\tilde{Z}$
Complex capacitance	$\tilde{C} = \tilde{Y}(i\omega)^{-1}$
Dielectric susceptibility	$\tilde{\chi} = \tilde{\epsilon}_r - \epsilon_\infty$

$\mu = i\omega C_0$, where C_0 is the capacitance of the empty cell.
 $C_0 = \epsilon_0 \frac{A}{d}$

about the dielectric processes in the system. These are summarized in Table 2.1.

Usually an equivalent circuit can be found, which has the same impedance as the sample. Such a circuit may be composed by capacitors, resistances, inductances or constant-phase elements (CPE). Each of these circuit elements is related to some physical process in the material, *e.g.*, polarization, bulk conductivity or a chemical step in an electrode reaction. If the equivalent circuit of the sample is found, the properties of each process may be analyzed separately. The frequency dependence of the impedance for each of these simple elements is given by:

$$Z_R = R, \tag{2.12}$$

$$Z_C = 1/(i\omega C), \tag{2.13}$$

$$Z_L = i\omega L, \tag{2.14}$$

$$Z_{\text{CPE}} = A_{\text{CPE}}(i\omega)^{-n}, \tag{2.15}$$

2.3 Impedance spectroscopy

where R is the impedance of an ohmic resistance, C the capacitance of a capacitor, L the inductance of a solenoid, A_{CPE} and n is a pre-exponential factor and an exponent of a constant-phase element, respectively, with $0 < n < 1$. The CPE is an empirical impedance function which has proved of considerable value in data fitting. It is found [59] that an exponential distribution of activation energies and an Arrhenius behavior for τ :

$$\tau = \tau_0 \exp(E_A/kT), \quad (2.16)$$

lead directly to CPE behavior.

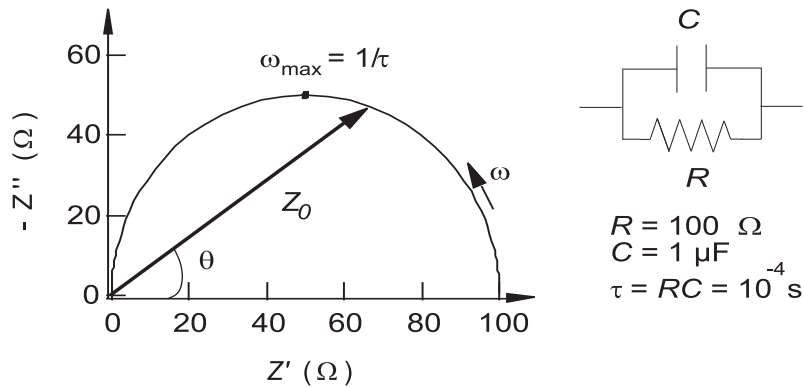


Figure 2.5: Complex plane representation of the impedance of a Voigt element (a resistance R and capacitance C in parallel). The arrow indicates the direction of increasing frequency.

Many solid electrolytes can be described by a series of the so called Voigt elements [59]. Figure 2.5 shows the impedance for such an element in a complex plane representation.

If the relaxation times of these elements are different enough, one obtains separate semicircles lying one next to the other. Each of these semicircles describes the response at some region of the sample. In polycrystalline materials one has the impedance of the electrode-electrolyte interface (el), of the grain boundaries (gb) and of the bulk (b). The slower response is that of the electrode-electrolyte interface and, therefore, is found at low frequencies. With increasing frequency one first finds the response of the grain boundaries and at high frequencies that of the bulk (Figure 2.6).

Because of the smaller volume fraction of grain boundaries in the material it is possible that $R_{\text{gb}} > R_{\text{b}}$ or $\rho_{\text{gb}} > \rho_{\text{b}}$ in the complex impedance or resistivity representation, respectively, even though $\sigma_{\text{gb}} > \sigma_{\text{b}}$.

2.3 Impedance spectroscopy

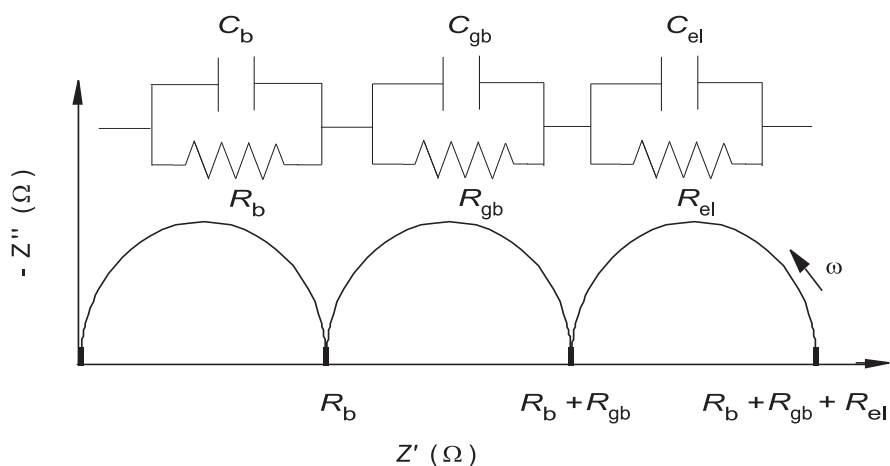


Figure 2.6: Schematic representation of the complex plane impedance diagram of a polycrystalline sample with $\omega_b \gg \omega_{gb} \gg \omega_{el}$, and the corresponding equivalent circuit. ω_b , ω_{gb} and ω_{el} are the inverse of the relaxation time in each region.

The differentiation of the semicircles is rarely found in practice and one usually observes just one or two overlapping semicircles. By representing other dielectric functions it is sometimes possible to obtain information about the different responses that are not seen in the impedance representation.

2.3.1 Modulus and impedance representation

A comparison between the modulus and the impedance representation has been proven to be advantageous when studying the electrical properties of polycrystalline materials [60]. From the complex plane diagrams information about the properties of the bulk and grain boundaries can be obtained.

Lets consider a system described by a series array of two parallel RC elements (Figure 2.7), one representing the response of the bulk and the other one that of the grain boundaries. In general their capacitances are comparable but their resistance may differ by many orders of magnitude.

The impedance of this system is given by

2.3 Impedance spectroscopy

$$Z' = \frac{R_b}{1 + \omega^2\tau_b^2} + \frac{R_{gb}}{1 + \omega^2\tau_{gb}^2} \quad (2.17)$$

$$-Z'' = \frac{\omega\tau_b R_b}{1 + \omega^2\tau_b^2} + \frac{\omega\tau_{gb} R_{gb}}{1 + \omega^2\tau_{gb}^2} \quad (2.18)$$

where Z' and Z'' are the real and imaginary part of the impedance, respectively, and τ is the corresponding relaxation time in the bulk or at the grain boundaries. For the modulus one has

$$M' = \frac{\omega^2 C_0 \tau_b R_b}{1 + \omega^2 \tau_b^2} + \frac{\omega^2 C_0 \tau_{gb} R_{gb}}{1 + \omega^2 \tau_{gb}^2} \quad (2.19)$$

$$M'' = \frac{\omega C_0 R_b}{1 + \omega^2 \tau_b^2} + \frac{\omega C_0 R_{gb}}{1 + \omega^2 \tau_{gb}^2} \quad (2.20)$$

where M' and M'' are the real and imaginary part of the modulus, respectively. In the complex plane representation of the modulus the two semicircles are resolvable provided that the relaxation times of the parallel RC elements differ sufficiently, and in particular, these differences occur in R rather than in C (see Figure 2.8, circuit A).

In contrast, a single semicircle is observed in the complex impedance plane, when only the relaxation of the grain boundaries can be seen. The maximum in the impedance representation occurs at $\omega R_{gb} C_{gb} = 1$. But in the modulus representation the maxima do not occur at $\omega = (RC)^{-1}$, because the semicircles overlap.

In the case of similar resistances and different capacitances (circuit B in Figure 2.7) the diagrams are reversed. A single semicircle is found in the modulus representation and two overlapping semicircles can be distinguished in the impedance representation (Figure 2.8).

Nevertheless, one may have a system with different resistances and similar capacitances presenting only one semicircle in the modulus representation. This occurs when one of the resistances is much bigger than the other one, so that only the contribution of one parallel RC element is seen in both the complex impedance and modulus representations.

2.3 Impedance spectroscopy

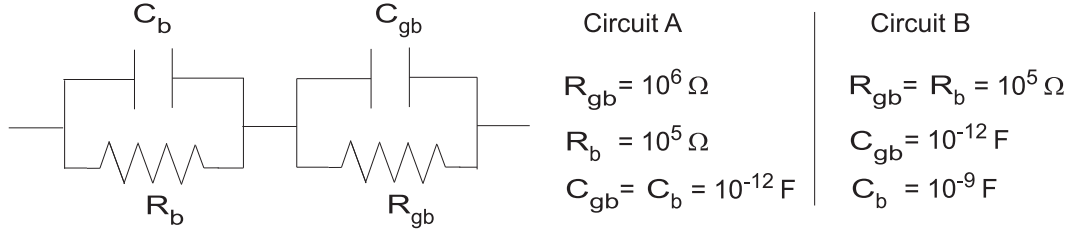


Figure 2.7: Equivalent circuit of a system showing bulk and grain boundary relaxation. The complex modulus and impedance planes are represented in Figure 2.8 for circuit A and B.

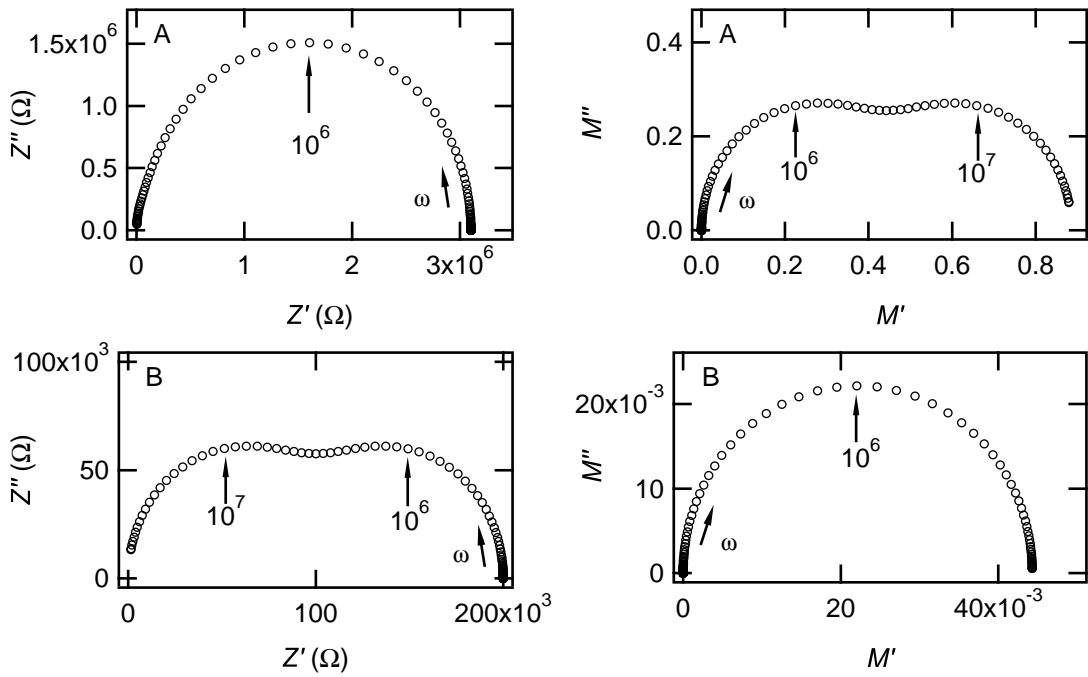


Figure 2.8: Simulated complex plane diagrams of the modulus and impedance of circuit A and B (see Figure 2.7) and calculated from Equation (2.17) to (2.20). The arrows indicate the position at $\omega = (RC)^{-1}$. The value of this frequency is also indicated.

2.3 Impedance spectroscopy

Temperature dependence of the conductivity

In addition to frequency-dependent measurements of the conductivity, one may study its temperature dependence and obtain further information about the dynamic processes in the system.

The dc conductivity σ_{dc} usually shows an Arrhenius behavior below the glass transition temperature:

$$\sigma_{\text{dc}}T = A_{\text{dc}}\exp(-E_{\text{A}}/kT), \quad (2.21)$$

where E_{A} is the activation energy of the conductivity process, k is Boltzmann's constant and T the absolute temperature. The pre-exponential factor A_{dc} contains several constants related to the type of conduction [61].

In a semiconductor several charge carriers may contribute to the overall conductivity. Therefore, one has, in general:

$$\sigma' = \sigma_{\text{e}'} + \sigma_{\text{h}'} + \sigma_{\text{ion}}, \quad (2.22)$$

where $\sigma_{\text{e}'}$, $\sigma_{\text{h}'}$ and σ_{ion} are the conductivities of the electrons, holes and ions, respectively. The sum of the electron and hole conductivities is called electronic conductivity. Depending on the mobilities of these charge carriers one speaks about electronic, ionic or mixed conductors. In the case of an electronic conductor, E_{A} corresponds to the band-gap energy between the valence band and the conduction band (in the high temperature region) or to the energy needed to excite an electron from a defect state to the conduction band (in the low-temperature region). In contrast to that, in the case of an ionic conductor, E_{A} is related to the activation energy for migration of defects (in the low-temperature region) or to the formation and migration of these defects (in the high-temperature region).

2.3.2 Models

Some models have been developed in order to derive microstructural information of the system from impedance measurements [59]. A useful quantity in expressing models is the complex conductivity, described below.

The complex conductivity

The complex conductivity of a system is simply given by its admittance and geometry:

2.3 Impedance spectroscopy

$$\tilde{\sigma} = \tilde{Y} \frac{l}{A}. \quad (2.23)$$

One may express the complex (or total) conductivity ($\tilde{\sigma} = \sigma_{\Sigma}$) as the sum of the conductivity relaxation and the dipolar relaxation of the system (see section 2.2):

$$\sigma_{\Sigma} = \sigma_{\text{dc}} + i\epsilon_0\omega\tilde{\chi}(\omega) = \sigma'(\omega) + i\epsilon_0\omega\chi'(\omega), \quad (2.24)$$

where $\sigma'(\omega)$ and $\chi'(\omega)$ are the real part of the complex conductivity and the dielectric susceptibility, respectively. σ_{dc} is the dc conductivity of the sample.

It is empirically found that σ' may be approximated by the power law [58]

$$\sigma' = \sigma_{\text{dc}} + A_p\omega^n, \quad (2.25)$$

where A_p is a pre-exponential factor and n an exponent with $0 < n < 1$. The exponent n is responsible for the dispersion region found in many ceramic materials at high frequencies which results from correlated back-and-forth hopping processes induced by the repulsive Coulomb interaction between the mobile ions in the system [62].

The models usually consider two phases present in the system. The complex conductivity of each phase may be defined as

$$\tilde{\sigma}_j = \sigma_j + i\omega\tilde{\epsilon}_j, \quad (2.26)$$

where σ_j is the dc conductivity and $\tilde{\epsilon}_j$ the permittivity of phase j .

The brick layer model

The brick layer model considers the microstructure as an array of cubic-shaped grains separated by flat grain boundaries (Figure 2.9a). The thickness of the grains is D and that of the grain boundaries d , where $d \ll D$, so that the volume fraction of the grain boundary region is $3d/D$. Two paths are possible for the current flow (Figure 2.9b). In path 1 the current flows through grain interiors¹ and across grain boundaries and in path 2 it flows along the grain boundaries.

¹The terms grain interior, bulk and volume, will be treated indistinctly to refer to the region inside the grains.

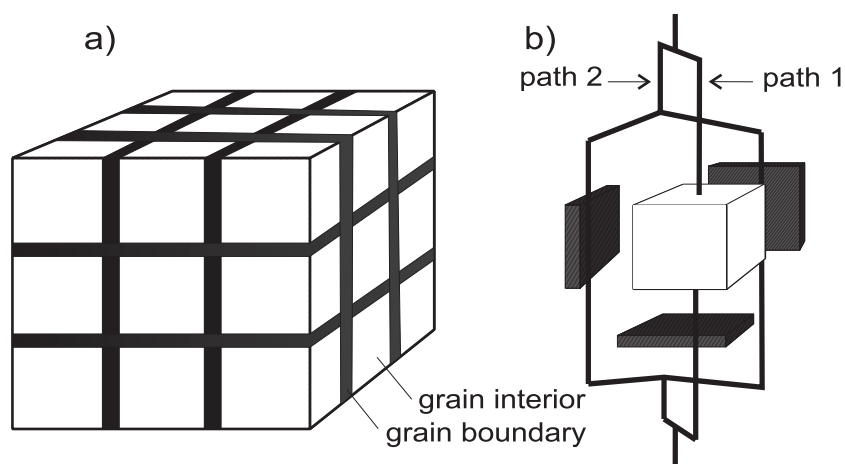


Figure 2.9: Brick layer model for a solid electrolyte with two phases. The solid is assumed to be composed of an array of cubic grains separated by flat grain boundaries (a). Sketch of the two possible paths for current flow (b). Path 1, through grain boundaries and grain interiors, and path 2, along grain boundaries.

The model can be used to fit experimental data and microstructural parameters as, for example, the capacitance and thickness of the grain boundaries, may be obtained.

Easy path model

In many instances where the bulk conductivity is greater than the conductivity of the grain boundaries, it is empirically found that the corresponding activation energies are very similar. This observation may be explained by the presence of regions of good intergranular contact (easy paths) (Figure 2.10a). This model was suggested by Bauerle [63], who proposed the circuit shown in Figure 2.10b. The oxygen ions in the ceramic material are sequentially partly blocked when they migrate both through grain boundaries or grain interiors. R_{ep} is the resistance through the constricted ionic paths [59].

2.4 Defect chemistry of TiO_2

By studying the effect of the oxygen partial pressure (P_{O_2}) on the conductivity, one can obtain information about the defects present in the oxide [64].

2.4 Defect chemistry of TiO₂

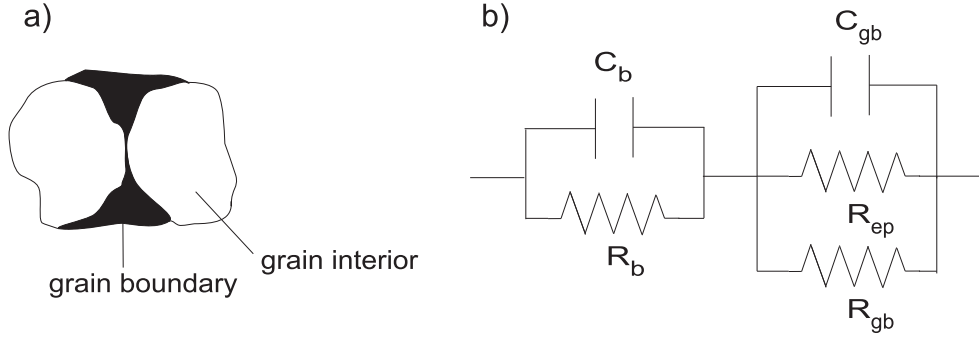
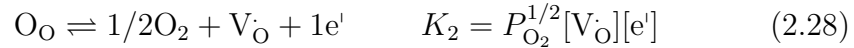


Figure 2.10: Easy path model for a solid electrolyte with two phases. Sketch of the grains separated by a discontinuous grain boundary phase (a). Equivalent circuit proposed by Bauerle [63] to describe the model (b).

A large amount of literature is available referring to the defect chemistry of TiO₂ [9–27]. There are four main types of defects in titanium dioxide, namely (using the Kröger-Vink notation) $V_{\text{O}}^{\bullet\bullet}$, V_{O}^{\bullet} , $\text{Ti}_{\text{i}}^{4\bullet}$ and $\text{Ti}_{\text{i}}^{3\bullet}$. In the region of low oxygen partial pressures the following reactions may be written:



The terms between brackets are the corresponding concentrations of each species. The equilibrium constants K_1 , K_2 , K_3 and K_4 are obtained applying the law of mass action.

If $V_{\text{O}}^{\bullet\bullet}$ is the majority defect one finds, from Equation (2.27), that $[e'] \propto P_{\text{O}_2}^{-1/6}$, since $V_{\text{O}}^{\bullet\bullet} \propto [e']$. Thus a slope of $-1/6$ in the representation of $\log \sigma_{\text{dc}}$ versus $\log P_{\text{O}_2}$ is expected. Analogously, one expects a slope of $-1/4$ if V_{O}^{\bullet} or $\text{Ti}_{\text{i}}^{3\bullet}$ is the majority defect, from Equation (2.28) and (2.29), respectively, and a slope of $-1/5$ if $\text{Ti}_{\text{i}}^{4\bullet}$ is the majority defect (Equation (2.30)).

The above equations describe the regime of n-type conductivity (low oxygen partial pressures) represented schematically in Figure 2.11. For the p-type conductivity regime (high oxygen partial pressures) one may write the following equation:



2.5 Surface conductivity

In this case the slope in Figure 2.11 would be $+1/4$. In the region between the p- and the n-type regimes one has ionic conductivity when the Gibbs free energy necessary to create a defect, is lower than the band gap of the oxide, *i.e.*, when the concentration of defects is larger than the concentration of intrinsic electronic defects (electrons and holes) [64]. In the middle of this region the crystal is stoichiometric.

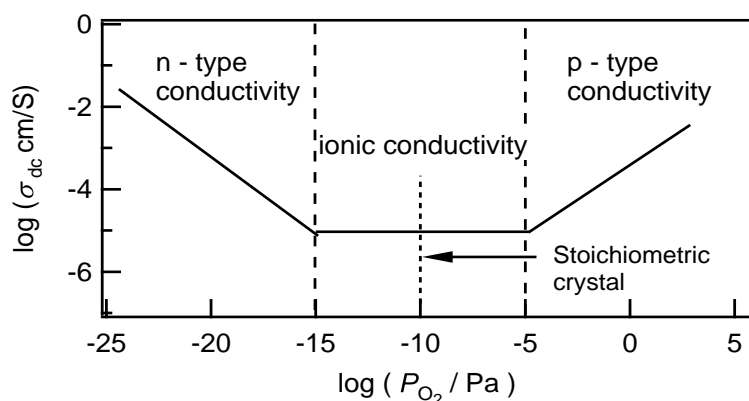


Figure 2.11: Schematic representation of the oxygen partial pressure dependence of the conductivity of a metal oxide at a constant temperature. Ionic conductivity predominates in the region of oxygen partial pressures between n- and p-type conductivity. In general the contribution of electrons and holes to the conductivity at lower temperatures is larger than that of the ions for all partial pressures. Exceptions are pure ionic conductors like, *e.g.*, ZrO_2 .

Of course, this is very schematic and in practice one may have aliovalent impurities and/or a mixture of defects contributing to the overall conductivity.

2.5 Surface conductivity

The surface conductivity σ'_{\square} is defined as specific conductivity per unit area. The electrode configuration used for surface conductivity measurements in this work is represented in Figure 2.12.

The surface conductivity σ'_{\square} (in S) is related to the surface conductance G (in S) according to the equation

2.5 Surface conductivity

$$\sigma'_{\square} = Ga/b, \quad (2.32)$$

where a is the distance between the electrodes and b is the length of the electrode [65]. The surface area (A) between the contacts is given by $A = ab$ (see Figure 2.12). The conductance G is calculated using Ohm's law

$$G = I/U, \quad (2.33)$$

where U is the voltage applied between the electrodes and I the current generated.

The surface conductivity often shows a low frequency dispersion (LFD) which involves two fractional power law terms [58]

$$\sigma'(\omega) = A_1\omega^{n_1} + A_h\omega^{n_2}, \quad (2.34)$$

where ω is the angular frequency ($\omega = 2\pi\nu$); the exponent n_1 and the pre-exponential factor A_1 describe the relaxation at low frequencies, while n_2 and A_h describe the relaxation at high frequencies.

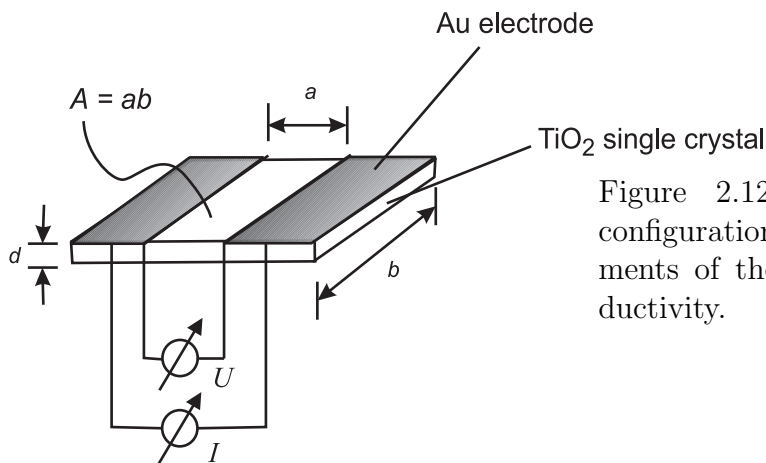


Figure 2.12: Electrode configuration for measurements of the surface conductivity.

In conductivity measurements n_1 is in general close to zero and one obtains a dc plateau at low frequencies with $A_1 = \sigma_{dc}$ and a dispersion region at high frequencies related to n_2 (cf. Equation (2.25)). However, surface conductivity measurements often show values in the range $0.1 \leq n_1 \leq 0.4$ and one obtains a dispersion at low frequencies (LFD)(Figure 2.13).

2.6 Photoconductivity

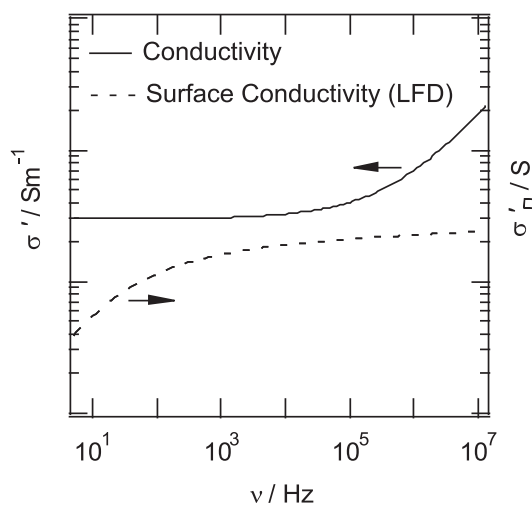


Figure 2.13: Schematic plot of the frequency dependence of the real part of the conductivity for a system with LFD and for one showing usual conductivity with a dc plateau at low frequencies. The curves are calculated using the circuits represented in Figure 2.14.

The physical meaning of the LFD in the literature is not clear [58] but is often related to the presence of moisture in surface conductivity measurements of low conductive materials [66]. It is also found in systems dominated by hopping of charge carriers [67].

Equivalent circuits used to model the response of a system without and with LFD are shown in Figures 2.14a and 2.14b, respectively. The difference between the two circuits is an additional constant phase element (CPE) in series with the resistor. This new constant phase element is responsible for the dispersion at low frequencies. The equivalent circuit shown in Figure 2.14b is completely empirical and therefore it is difficult to assign a physical meaning to each element.

2.6 Photoconductivity

The increase in the electrical conductivity of certain materials due to the absorption of photons is called photoconductivity. The energy of the photons must be sufficient to overcome the band gap of the material.

2.6 Photoconductivity

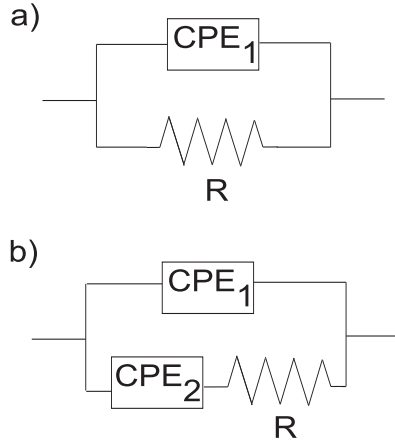


Figure 2.14: Equivalent circuit for a system without LFD (a) and one with LFD (b).

During the absorption process a certain concentration of excess electrons (Δn) and excess holes (Δp) are generated in the conduction and valence band, respectively. The concentration of electrons in the conduction band n and holes in the valence band p , may be written as

$$n = n_e + \Delta n \quad (2.35)$$

$$p = p_e + \Delta p, \quad (2.36)$$

where n_e and p_e are the equilibrium concentrations (without illumination) of electrons and holes in the conduction band and in the valence band, respectively [68]. The amount of absorbed light energy propagated in the x direction per unit time and volume is equal to

$$-\frac{dI}{dx} = \alpha I, \quad (2.37)$$

where I is the light intensity and α the light absorption coefficient. The rates of change of Δn and Δp with time have to be proportional to αI

$$\frac{d\Delta n}{dt} = \frac{d\Delta p}{dt} = \beta \alpha I, \quad (2.38)$$

where β is a proportionality constant. If one expresses I as the number of absorbed quanta per second, then β has the meaning of a quantum yield, *i.e.*, β determines the number of electron-hole pairs generated through the absorption of one photon². If one assumes that the generation of charge carriers through light absorption is the only process taking place in the solid, it

²Normally β is not greater than one. However, if the energy of the quantum corresponds

2.6 Photoconductivity

is clear that the concentration of excess charge carriers will increase continuously as

$$\Delta n = \Delta p = \beta \alpha I t. \quad (2.39)$$

However, in practice, one obtains a stationary value of the photoconductivity σ_0 after a certain time. Obviously, a recombination process also takes place in the material which, under steady-state conditions, has the same velocity as the generation process.

The value of the steady-state concentration of excess charge carrier depends on the number of excess charge carriers generated per unit volume and unit time (Equation (2.38)), and on the mean lifetime of the excess charge carrier. The mean lifetime of the excess electrons τ_n is defined as the average time that an electron, generated by the absorption of light, remains in the conduction band. Analogously, τ_p represents the average time of holes in the valence band. In general, the magnitude of the mean lifetime can take values between $\sim 10^{-2}$ s and 10^{-7} s. The steady-state concentration of excess charge carriers can therefore be expressed by the following equations:

$$\Delta n_0 = \beta \alpha I \tau_n \quad (2.40)$$

$$\Delta p_0 = \beta \alpha I \tau_p. \quad (2.41)$$

For the steady-state conductivity one has

$$\sigma_0 = e \mu_n \Delta n + e \mu_p \Delta p = e \beta \alpha I (\mu_n \tau_n + \mu_p \tau_p), \quad (2.42)$$

where e is the elementary charge, μ_n and μ_p are the mobility of electrons and holes, respectively. If one of the two terms between brackets is much bigger than the other one, due to a higher mobility or to a longer lifetime, then one speaks about unipolar photoconductivity:

$$\sigma_0 = e \beta \alpha \mu \tau I. \quad (2.43)$$

In this case, the steady-state photoconductivity is described by four parameters. α and β describe the interaction between light and matter, related to the generation of excess charge carriers. μ and τ describe the interaction between the charge carriers and the material, and are related to recombination and transport processes.

to twice the energy of the band gap, the generated charge carriers have a kinetic energy that may be sufficient to generate another charge carrier through impact ionization. In this case β is smaller than 1.

2.6 Photoconductivity

Occupation of energy states

The concentration of electrons in the conduction band can be calculated from the density of states $N(E)$ as a function of the energy E and the Fermi function $f(E)$

$$n_e = \int_{E_c}^{\infty} f(E)N(E)dE, \quad (2.44)$$

where E_c is the energy of the bottom of the conduction band. The distribution function $f(E)$ is the probability that a state with energy E will be occupied, and is expressed as

$$f(E) = \frac{1}{e^{\frac{(E-F)}{kT}} + 1}, \quad (2.45)$$

where F is the Fermi energy, also called chemical potential [69].

Assuming Boltzmann distribution, *i.e.*, for $E - F \gg kT$, one has

$$n_e = \frac{2}{h^3}(2\pi m_e kT)^{3/2} e^{-(E_c-F)/kT} = N_c e^{-(E_c-F)/kT}, \quad (2.46)$$

where h is Planck's constant, m_e is the effective mass of electrons and N_c is the effective density of states in the conduction band. Similarly for holes in the valence band

$$p_e = \frac{2}{h^3}(2\pi m_p kT)^{3/2} e^{-(F-E_v)/kT} = N_v e^{-(F-E_v)/kT}, \quad (2.47)$$

where m_p is the effective mass of holes and N_v is the effective density of states in the valence band.

Under illumination the overall concentration of charge carriers is often described by quasi Fermi levels (F_n for electrons and F_p for holes)

$$n = n_e + \Delta n = N_c e^{-(E_c-F_n)/kT} \quad (2.48)$$

$$p = p_e + \Delta p = N_v e^{-(F_p-E_v)/kT}. \quad (2.49)$$

In contrast to the value of the Fermi level F in equilibrium conditions, the values of the Fermi level for electrons F_n and holes F_p are different, even under steady-state conditions.

2.6 Photoconductivity

In the following paragraphs two special cases of recombination processes will briefly be considered.

Linear recombination

Let us assume that the velocity of the recombination process is proportional to the first power of the excess concentration of charge carriers. This may be the case when, *e.g.*, the concentration of holes is very high and independent of illumination. Then, τ_n is constant and after switching on the light one has

$$\frac{d\Delta n}{dt} = \beta\alpha I - \frac{\Delta n}{\tau_n}. \quad (2.50)$$

This yields a exponential curve with a time constant equal to the mean lifetime τ_n . When the light is switched off the following equation is valid:

$$\frac{d\Delta n}{dt} = -\frac{\Delta n}{\tau_n}. \quad (2.51)$$

Both curves (rise and decay) show an exponential behavior and are symmetric because they are characterized by the same time constant (Figure 2.15). The value of the excess charge carrier concentration under steady-state conditions is $\Delta n_0 = \tau_n \beta \alpha I$.

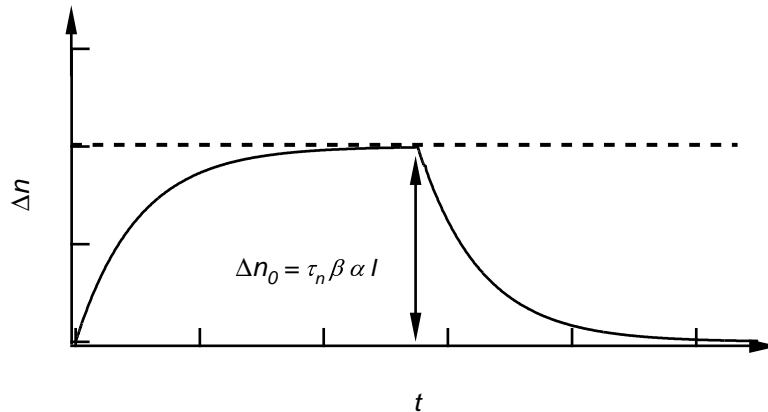


Figure 2.15: Rise and decay curves after switching on and off, respectively, the light for a system showing linear recombination. Δn_0 is the value of the concentration of excess electrons under steady-state conditions.

2.7 Heterogeneous catalysis

Quadratic recombination

One may as well assume, that the recombination velocity is proportional to the square of the excess concentration of charge carriers. This happens *e.g.*, when the concentration of charge carriers in equilibrium is zero. Then the concentration of excess electrons and excess holes is the same. So the recombination velocity can be expressed as $\gamma\Delta n\Delta p = \gamma(\Delta n)^2$, where γ is the so-called recombination coefficient.

Solving the equations

$$\frac{d\Delta n}{dt} = \beta\alpha I - \gamma(\Delta n)^2 \quad (2.52)$$

and

$$\frac{d\Delta n}{dt} = -\gamma(\Delta n)^2, \quad (2.53)$$

one obtains two different curves for the rise and the decay. In contrast to linear recombination, the curves are not symmetric and the time constant is a function of time.

More complicated equations are found when traps (recombination centers) are present in the band gap. In general one has to consider only the fastest transitions between electrons in the conduction band, in the valence band and in the traps present. Therefore, only approximated functions of the relaxation curves (rise and decay) can be calculated.

2.7 Heterogeneous catalysis

A catalyst is defined as a substance that increases the rate of reaction without being appreciably consumed in the process [70]. In general, this occurs by lowering the height of an activation barrier. However, the catalyst does not change the properties of the equilibrated state, *i.e.*, the relative energetic positions of the initial and final states.

Another important property of a catalyst is its selectivity. The catalyst should not only accelerate reactions, but also select them, so that the desired products are obtained.

The main steps in heterogeneous catalysis are:

1. Diffusion of the reactants from the fluid phase (gas or liquid) to the surface.

2.7 Heterogeneous catalysis

2. Adsorption of at least one of the reactants.
3. Reaction in the adsorbed phase.
4. Desorption of the products.
5. Diffusion of the products to the fluid phase.

Heterogeneous photocatalysis

The same steps are valid for heterogeneous photocatalysis, but in contrast to conventional catalysis, the catalyst is activated by the absorption of photons instead of being thermally activated. The catalysts used are chalcogenides (oxides and sulfides) such as TiO_2 , ZnO , CeO_2 , ZrO_2 , SnO_2 , CdS , ZnS , etc [2]. Among these, the best performance is achieved with TiO_2 .

The energy of the incident photons has to be equal or greater than the band-gap energy E_G of the semiconductor ($h\nu \geq E_G$). After excitation, the generated electrons and holes can follow several pathways. Figure 2.16 shows schematically some of the de-excitation processes that occur in the catalyst. The photogenerated electrons and holes may migrate to the semiconductor surface and there react with organic or inorganic species from the fluid phase (gas or liquid). A photoinduced electron can be transferred to an electron acceptor (A) at the surface of the catalyst. Similarly, a photoinduced hole can be transferred to an electron donor (D) at the surface of the catalyst. Other processes, which decrease the efficiency of the catalyst, are, *e.g.*, recombination at the surface and in the volume of the solid of electrons and holes.

The catalytic activity, *i.e.* efficiency, of a catalyst is measured as a quantum yield (QY) which is defined as the ratio of the rate of conversion of molecules to the rate of absorption of photons:

$$QY = \frac{\text{number of converted molecules}}{\text{number of absorbed photons}} \quad (2.54)$$

Due to scattering of light by the semiconductor surface, it is difficult to measure the actual absorbed light in heterogeneous systems. Hence, it is usually assumed that all the light is absorbed and the efficiency is given as an apparent quantum yield [1].

2.7 Heterogeneous catalysis

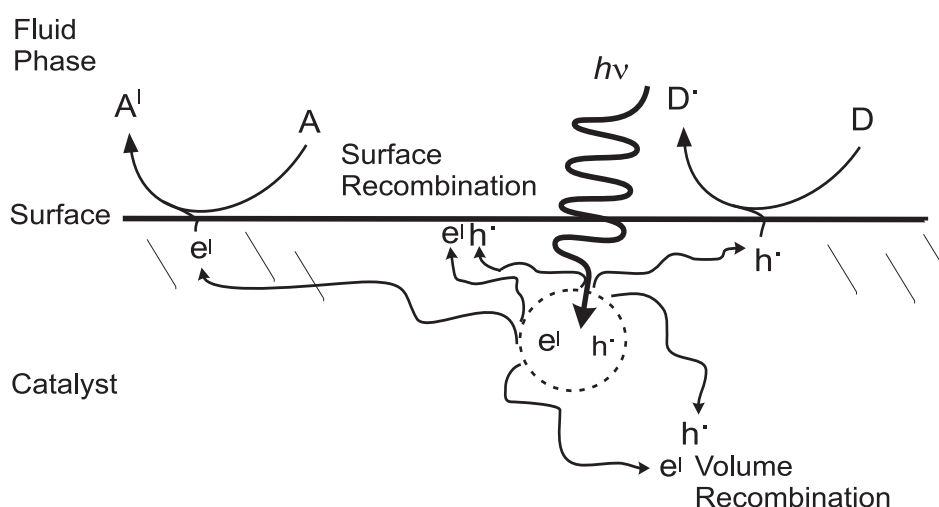


Figure 2.16: Scheme of the photoexcitation in the catalyst. After the absorption of a photon the generated electron may react with an acceptor (A) and the hole with a donor (D) at the surface of the catalyst. Volume recombination and surface recombination processes may also occur [1].

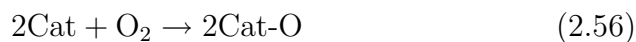
Mars-van Krevelen mechanism

In 1954 Mars and van Krevelen developed a model to explain the catalytic oxidation of hydrocarbons [70,71]. They postulated two steps:

1. Reaction between the catalyst and the hydrocarbon, in which the latter is oxidized and the former reduced:



2. Reaction of the reduced oxide with oxygen from the gas phase to restore the initial state:



No assumption is made about the type of oxygen in the catalyst, *i.e.*, it can be either chemisorbed or lattice oxygen. However, this model is generally followed by systems involving lattice oxygen, whereas chemisorbed oxygen systems present other kinetic behaviors that can be explained in terms of Langmuir-Hinshelwood or Rideal models. For lattice oxygen systems the active species is the O^{2-} ion.

2.7 Heterogeneous catalysis

Heterogeneous photocatalysis in TiO_2

Titanium dioxide has been extensively investigated due to its potential application as a photocatalyst for the total mineralization of environmentally harmful organic compounds in air and water [72, 73]. However, the mechanism governing the photo-catalyzed redox reactions is still unclear. Several reactive species are proposed in the literature such as O^- , O_2^- , O_3^- , and $\bullet\text{OH}$ [1–4, 72, 73].

In conventional catalysis lattice oxygen is the most important species [70], as explained above by the Mars-van Krevelen mechanism.

Chapter 3

Materials and sample preparation

3.1 Titanium dioxide TiO_2

Natural titanium dioxide has three crystalline modifications: rutile (tetragonal), the most common form, and anatase (tetragonal) and brookite (orthorhombic), both of which convert to rutile at elevated temperatures (above 973 K). All contain six-fold coordinated titanium atoms, which form TiO_6 octahedra. In rutile the octahedra are not regular, showing a slight orthorhombic distortion, in anatase and brookite the octahedra of oxygen atoms are significantly distorted, so that their symmetry is lower than orthorhombic. The modifications differentiate in the number of sharing edges of the TiO_6 octahedra. Rutile shares two, brookite three and anatase four edges with neighboring octahedra [74].

Rutile and anatase have different atomic distances. The Ti-Ti distance is bigger in anatase (3,79 and 3,04 Å vs. 3,57 and 2,96 Å in rutile), however, the Ti-O distance is smaller in anatase (1,934 and 1,980 Å vs. 3,57 and 2,96 Å in rutile).

Due to these structural differences they show different densities (see Tab. 3.1) and other physical properties. The absorption edge, depending on the modification, takes values between 380 nm and 420 nm (about 3 eV).

From these modifications, anatase shows the highest photocatalytic activity, followed by rutile. Brookite is photocatalytically not relevant.

At elevated pressures titanium dioxide transforms to a high pressure phase

3.1 Titanium dioxide TiO₂

TiO₂-II with α -PbO₂ structure (space group P bcn) (see, *e.g.*, [75,76]).

Table 3.1: Structural properties of the three modifications of TiO₂. a , b and c are lattice constants.

modification	anatase	rutile	brookite
density (g/cm ³)	3.89	4.25	4.23
a (Å)	3.785	4.5937	5.456
b (Å)			9.182
c (Å)	9.514	2.9618	5.143
space group	I 4 ₁ /amd	P 4 ₂ /mm	P bca
formula units/cell (Z)	4	2	8

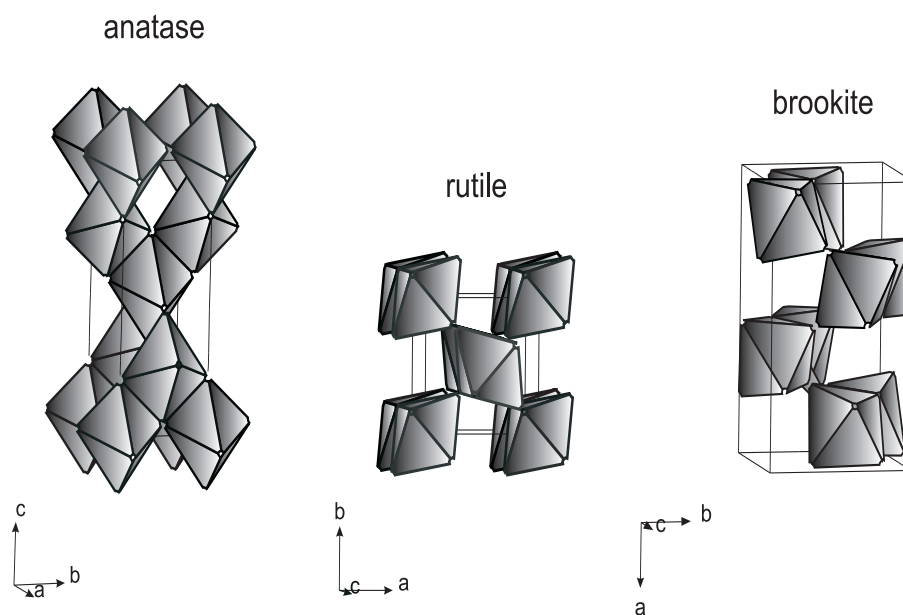


Figure 3.1: TiO₆ octahedra representing the different modifications of TiO₂: anatase, rutile and brookite.

Phase diagram

The phase diagram of titanium with oxygen presents several compounds. It is found that titanium dioxide has some oxygen deficit and it may be

3.1 Titanium dioxide TiO_2

written as TiO_{2-x} with x ranging between 0 and 0.05 [77]. For lower oxygen contents one observes the "Magnéli phases", which are a homologous series of triclinic phases of compositions $\text{Ti}_n\text{O}_{2n-1}$, with $4 \leq n \leq 10$ [78], the broad nonstoichiometric phases TiO_x ($0.7 \leq x \leq 1.3$), and the lower oxides Ti_3O_5 and Ti_2O_3 . With decreasing oxygen content of TiO_{2-x} the color changes from white ($x = 0$) to yellow, grey and finally black.

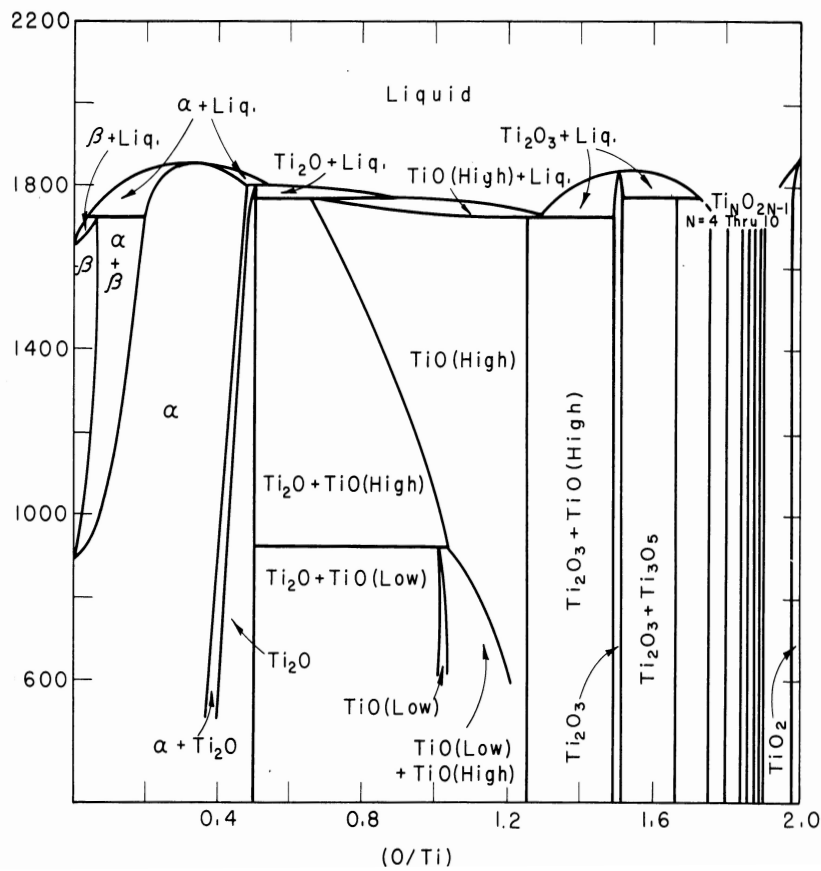


Figure 3.2: Phase diagram of the system Ti-TiO₂ [79].

Rutile surfaces

The ideal structures of the low-index faces of rutile, *i.e.*, (100), (110) and (001), are shown in Figure 3.3.

3.1 Titanium dioxide TiO_2

The (110) plane is the most stable of the low-index faces of rutile. The ideal structure of this surface contains equal numbers of five- and six-fold coordinated cations [65]. The (100) plane would ideally have five-fold coordinated cations and it is found to reconstruct upon annealing to generate several surface structures. The (001) plane is the least stable of these surfaces. Its ideal structure exposes cations which are all four-fold coordinated. Due to this high degree of coordinative unsaturation, reconstruction is observed upon quite mild annealing [80].

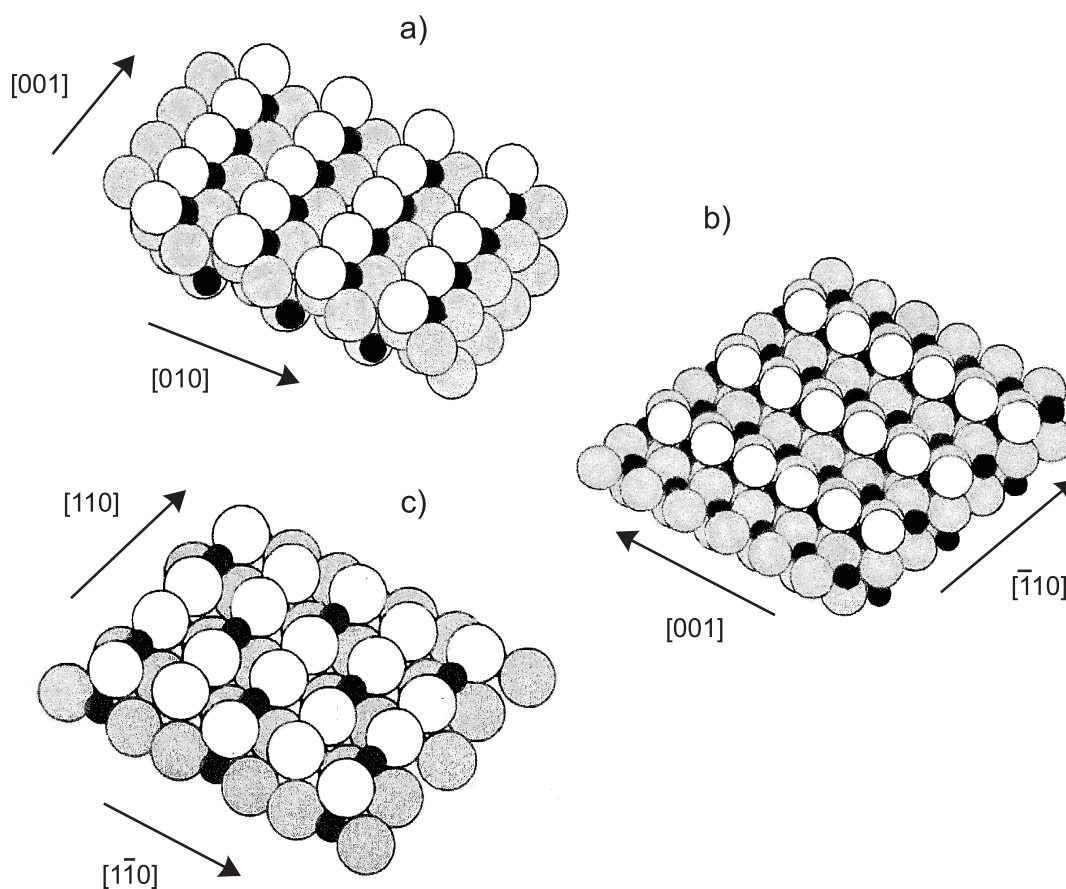


Figure 3.3: The ideal TiO_2 (100) (a), the TiO_2 (110) (b) and TiO_2 (001) (c) surfaces. Open circles represent top layer oxygen ions, solid circles are titanium ions and shaded circles are second (and deeper) layer oxygen ions [80].

3.2 High-energy ball milling

Production

Large amounts of titanium dioxide are produced from ilmenite FeTiO_3 using both the sulfate and the chloride routes [81].

The sulfate process consists of sulphation of the raw material by agitation with concentrated sulfuric acid. The resultant solution is treated to ensure that only ferrous-state iron is present. The solution is then cooled to crystallize coarse ferrous sulfate heptahydrate (known as "copperas", $\text{FeSO}_4 \cdot 7\text{H}_2\text{O}$) which is separated from the process. The titanium sulfate solution is then evaporated to a precise composition and hydrolyzed to produce a suspension ("pulp") consisting predominantly of clusters of colloidal hydrous titanium dioxide. Precipitation leads to titanium dioxide. This process can either produce anatase or rutile crystals.

For the chloride process ilmenite or natural titanium dioxide¹ are mixed with coke and chlorine in order to obtain titanium tetrachloride TiCl_4 . Distillation of this intermediate yields extremely pure titanium tetrachloride, which is oxidized at high temperature with oxygen giving only the rutile crystal form.

Extremely fine titanium dioxide (nanocrystalline) can be produced by the aerosol process from Degussa-AG. This process consists in the flame hydrolysis of TiCl_4 . By changing the conditions, temperature of the flame and time of residence of TiO_2 in the reaction chamber, one can control the particle size, particle distribution and surface conditions. The sol-gel process is another possibility for the production of fine titanium dioxide. Titanium tetrachloride or titanium alcoxides (usually titanium tetra-isopropoxide or titanium n-butyloxyde) are hydrolyzed and condensed to form a gel which is dried and sintered giving titanium dioxide.

3.2 High-energy ball milling

High-energy ball milling (HEBM) is an attractive alternative for the production of nanocrystalline materials. Unlike the above mentioned procedures HEBM is much easier to be carried out. It can be used for a wide range of materials and one can produce larger quantities [48, 82].

¹Natural titanium dioxide contains mostly iron impurities and is therefore dark or black and has to be purified.

3.3 Sample preparation

The sample is placed in a container with one or more grinding elements. The containers are usually cylindrical and the grinding elements are often balls but may be also cylinders, rods, or other shapes. The container with the sample and the grinding elements inside is placed in the high-energy ball mill and shaken. The inertia of the grinding elements causes them to move into each other and against the container wall, grinding the sample. HEBM may be used not only to grind materials but also to bond metal compounds in a process called mechanical alloying.

A high-energy ball mill SPEX 8000 was used for grinding the microcrystalline and the nanocrystalline samples of titanium dioxide. This high-energy ball mill shakes the container back and forth several thousand times a minute. The vials and the grinding element (one ball) were made of alumina ceramic. The ball has a diameter of 8 mm and a mass of about 4 g. The sample to ball ratio used was 2:1. These parameters are optimized to minimize the attrition of the grinding tools during the milling process. The milling time was varied between 15 minutes and 4 hours.

3.3 Sample preparation

Impedance spectroscopy

Microcrystalline² (Acros, Germany) and Nanocrystalline (Sachtleben, Germany) samples of titanium dioxide for impedance spectroscopy were made by conventional room temperature compression under 1 GPa. With this method we obtained pellets with a diameter of 8 mm and thickness between 0.5 mm and 2 mm.

The electrodes used for the microcrystalline samples were made of platinum powder (Merck, > 99,9%) in a parallel plate configuration. To prepare the sample we proceed as follows: first some platinum powder is slightly pressed under 200 MPa. Then the titanium dioxide powder is added and pressed again under 200 MPa. Finally some platinum powder is thrown on top of the sample so that the area is completely covered with platinum and pressed under 1 GPa for about five minutes.

²Although the microcrystalline samples become nanocrystalline after a certain milling time, the term microcrystalline or 'milled microcrystalline' will be used in order to distinguish between the originally microcrystalline from the originally nanocrystalline samples.

3.3 Sample preparation

This procedure was not successful for preparing the nanocrystalline samples which broke easily and did not have a good contact with the platinum electrode. Hence, the nanocrystalline powder was pressed under 1 GPa for about five minutes without adding platinum powder neither above nor below the pellet. In this case we used physical vapor deposition (PVD) of gold to produce the electrodes.

Surface conductivity and photoconductivity

The surface conductivity and photoconductivity was measured for a TiO₂ (100) (rutile) single crystal (10 x 10 x 0.4 mm) (Crystec, Germany) only. The preparation of polycrystalline samples was not successful.

The titanium dioxide single crystal was heated up to 873 K during 1 hour in air in order to remove organic impurities which may cause a bad contact with the electrodes. The sample is left to cool down to room temperature and then gold is evaporated on the surface by PVD. Care was taken to leave a small area of 100 μm wide free of Au coverage. Following this procedure one obtains a surface with two electrodes and a 1 mm² region without electrodes through which the single crystal may interact with the atmosphere and/or absorb UV light (see Figure 2.12). After this procedure the surface conductance of the sample was not higher than 10^{-10} S at room temperature which is the lowest measurable value with our equipment. Moreover, it was found that titanium dioxide is only reduced at very low oxygen partial pressures.

Chapter 4

Characterization

4.1 X-ray diffraction

The phase composition of the samples was analyzed by X-ray diffraction (XRD). The measurements were performed with a Philips X'Pert MPD system using Cu-K α_1 radiation ($\lambda = 0.154056$ nm).

The average grain size L_0 of the samples can be determined from the line broadening of XRD profiles. The observed line broadening is due to the combined effects of a number of instrumental and physical factors, resulting in a net profile $g(\theta)$, where θ is the diffraction angle. If these effects are eliminated one obtains the pure diffraction line profile $f(\theta)$ whose broadening is determined by the mean crystallite size and strain $\epsilon_s = \Delta d/d$, where d is the lattice spacing [83]. The experimental profile $h(\theta)$ can be expressed by the following convolution relationship:

$$h(\theta) = \int_{-\infty}^{+\infty} g(\eta)f(\theta - \eta)d\eta. \quad (4.1)$$

In order to determine the crystallite size we have to firstly extract the pure profile $f(\theta)$ from the experimental $h(\theta)$ and secondly extract the size information from the profiles $f(\theta)$ of suitable lines of the XRD-pattern. The function $g(\theta)$ is determined by measuring the intensity distribution in the line profile of a strain-free material of sufficiently large crystallite size so that a pure diffraction broadening is effectively absent. The determination of $f(\theta)$ is done by unfolding equation (4.1). The two most applied methods to do this operation are the method of Stokes (or Fourier-transformation

4.1 X-ray diffraction

method) and the iterative method of successive folding of $h(\epsilon)$ with $g(\epsilon)$, where $h(\epsilon)$ is the experimental intensity of the line in point ϵ and $g(\epsilon)$ is the corresponding instrumental line broadening when no distortions from the sample are present [84]. However, simplified methods provide numerical results which are useful in many analytical and routine applications.

A standard procedure for determining the grain size is given by the Scherrer equation [85]:

$$L_0 = \frac{K \cdot \lambda}{\beta \cdot \cos\theta}, \quad (4.2)$$

where K is a constant, which depends on the shape of the crystallite (0.89 for spherical particles), λ is the wavelength of the x-ray source, θ the diffraction angle and β the pure line breadth at half maximum of the peak.

If Gaussian line shapes are assumed for h , g and f , the convolution integral, Equation (4.1), shows that

$$B^2 = b^2 + \beta^2 \quad (4.3)$$

where B is the experimental line breadth and b the instrumental line breadth. If Cauchy profiles are assumed for all functions we have

$$B = b + \beta. \quad (4.4)$$

The influence of lattice imperfections (strain) on the line breadth is dominant in materials with large crystallite sizes. For fine powders (crystallite sizes below 100 nm), the line broadening is mainly dominated by the small grain sizes rather than by the strain.

Microcrystalline titanium dioxide

Figures 4.1a and 4.1b show the XRD patterns of microcrystalline rutile and anatase, respectively, milled for different milling times. In addition, the XRD pattern for the nanocrystalline anatase powder is also shown. As expected, the line broadening increases with increasing milling time for both rutile and anatase samples. As already mentioned above, this increase is related to a decrease in the average crystallite size. A broad peak appears during milling the anatase samples at a diffraction angle of about 31.4° . This peak belongs to a high-pressure phase of titanium dioxide TiO₂-II with α -PbO₂ type structure (see Section 3.1).

4.1 X-ray diffraction

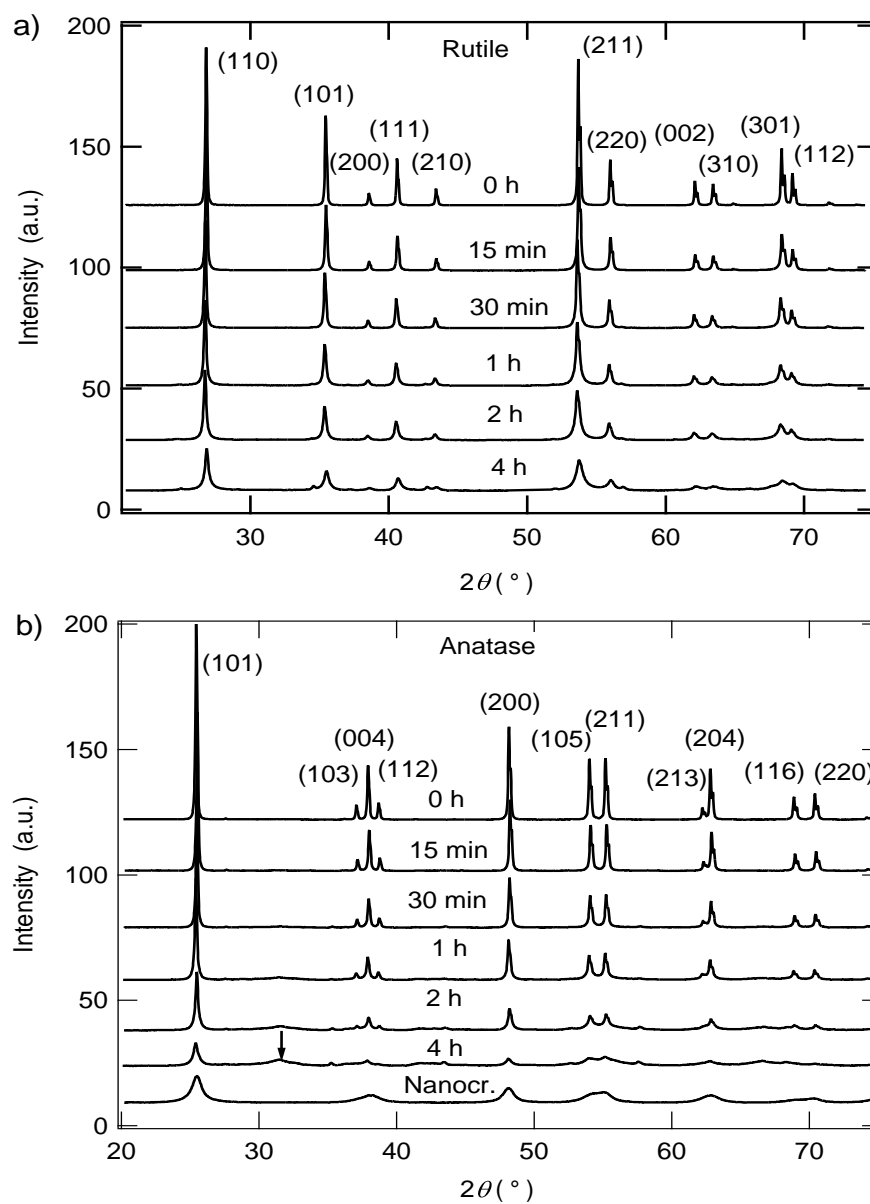


Figure 4.1: XRD pattern for the microcrystalline rutile samples with milling times between 0 and 4 hours (a). XRD pattern for the anatase samples milled up to 4 hours (b). The arrow indicates the presence of a high-pressure phase. The XRD pattern for the nanocrystalline sample (Sachtleben) is also shown for comparison.

4.1 X-ray diffraction

Table 4.1: Literature values for rutile [86] of the relative intensity I of each peak which corresponds to a crystallographic plane (hkl). The spacing d between planes is calculated using Bragg's law.

$2\theta^\circ$	I	hkl	$d(\text{\AA})$
27.19	1000	110	3.27686
35.69	443	101	2.51352
38.83	66	200	2.31712
40.81	181	111	2.20942
43.64	65	210	2.07251
53.76	522	211	1.70366
56.08	153	220	1.63844
61.98	72	002	1.49589
63.42	70	310	1.46547
64.82	6	221	1.43706
68.27	175	301	1.37257
68.95	86	112	1.36081
71.64	9	311	1.31606
73.64	2	320	1.2853

Table 4.2: Literature values for anatase [87]. I and d have the same meaning as in Table 4.1. The spacing d between planes is calculated using Bragg's law.

$2\theta^\circ$	I	hkl	$d(\text{\AA})$
25.343	1000	101	3.51134
37.920	19	103	2.37067
38.849	26	112	2.31609
39.627	148	004	2.27239
47.740	296	200	1.90344
52.045	0	202	1.75566
54.813	163	211	1.67336
56.007	158	105	1.64049
62.525	11	213	1.48422
63.723	101	204	1.45917
69.819	64	220	1.34593
71.383	51	116	1.32023

4.1 X-ray diffraction

Such a phase transformation has already been observed in the literature [88,89] and it was concluded that the new phase forms a thin cover layer at the surface of the particles. Phase transformations during high energy ball milling have also been observed in other ceramic materials [90].

In Tables 4.1 and 4.2 (rutile and anatase, respectively) the literature values of θ and the relative XRD-peak intensities I are given for each crystallographic plane (hkl), as well as the d spacing between them.

Therefore, from the broadening of the lines one can calculate the grain size for each milling time. This is shown in Figure 4.2. Milling times between 15 min and 4 h result in particle sizes between 1 μm and 20 nm and thus, to a decrease of about 3 orders of magnitude. A saturation value of the grain size is found at about 20 nm, which does not decrease even after 8 hours of milling. Such a behavior has already been observed in other ceramic materials [82] and metals [91].

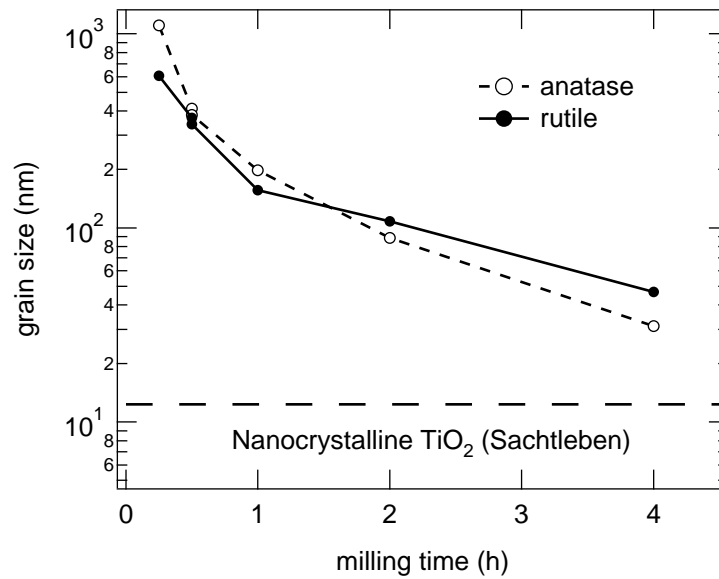


Figure 4.2: Grain size of milled microcrystalline rutile and anatase for different milling times. With increasing milling time the particle size decreases down to about 20 nm. Further milling does not change the grain size considerably [92].

4.1 X-ray diffraction

Nanocrystalline titanium dioxide

The XRD pattern of the milled nanocrystalline anatase samples are shown in Figure 4.3. Neither big changes in the width or height of the lines during milling, nor the formation of new phases during milling can be recognized. A particle size of about 10 nm is obtained from the breadth of the peaks. The slight decrease in the intensity of the lines with milling time indicates the formation of some amorphous phase.

A surface area of about $200 \text{ m}^2\text{g}^{-1}$ is obtained for all the samples from BET-surface area measurements [93] which agrees with the XRD results.

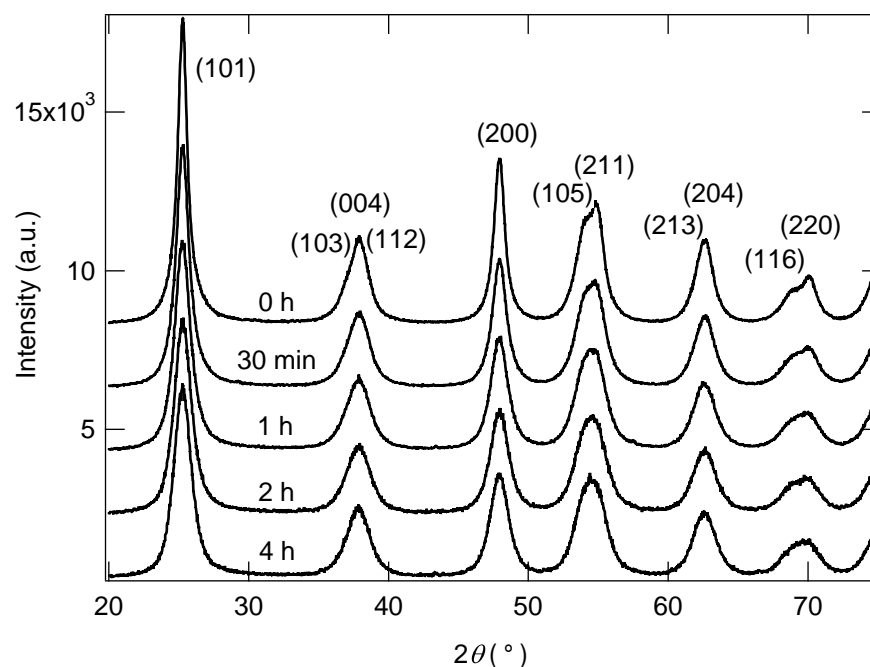


Figure 4.3: XRD pattern for the nanocrystalline anatase samples milled up to 4 hours. Neither the formation of a new phase nor a broadening of the lines with milling can be recognized. The slight decrease of the peak intensities with milling indicates the formation of amorphous regions in the material.

4.2 Transmission electron microscopy

The particle size obtained from the XRD patterns was verified by Transmission electron microscopy (TEM). The TEM pictures were taken on a Tecnai F20STEM (FEI company) equipped with an S-TWIN objective lens and a field emission gun.

Figure 4.4 shows a TEM micrograph with atomic resolution of microcrystalline rutile milled for 4 hours. A crystallite size of about 20 nm, in accordance with the XRD results, can be seen.

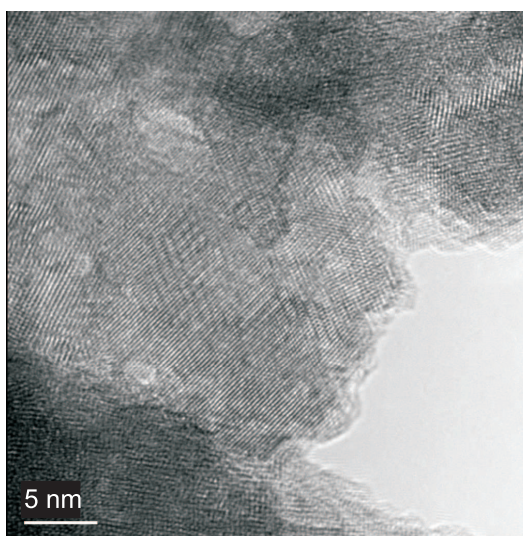


Figure 4.4: TEM micrograph of microcrystalline rutile milled for 4 hours [92].

4.3 BET surface area

Measurements of gas adsorption isotherms are widely used for determining the surface area and pore size distribution of solids. The most commonly used is the Brunauer-Emmett-Teller (BET) isotherm [94]:

$$\frac{p}{n(p_0 - p)} = \frac{1}{n_m c} + \frac{c - 1}{n_m c} \cdot \frac{p}{p_0}. \quad (4.5)$$

Here p is the pressure of the gas, p_0 is the saturated vapor pressure of the liquid at the operating temperature, n is the amount of gas adsorbed at the

4.3 BET surface area

relative pressure p/p_0 and n_m is the monolayer capacity. c is the so-called BET constant given by

$$c = \exp\left(\frac{H_1 - H_L}{RT}\right), \quad (4.6)$$

where H_1 is the heat of adsorption of the first layer of adsorbate and H_L is the latent heat of evaporation. The latter characterizes the adsorption of the second and subsequent layers [71].

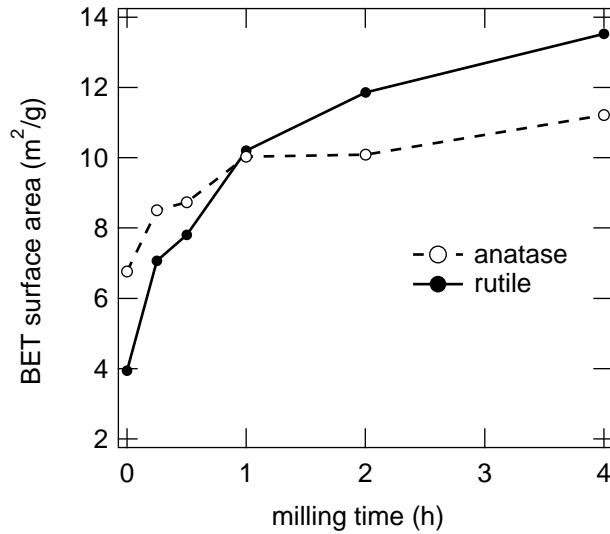


Figure 4.5: BET surface area of microcrystalline rutile and anatase for different milling times [92].

The surface area of the powder samples was measured with a Gemini III 2375 Surface Area Analyzer by the isothermal adsorption of nitrogen. Multi-point surface area was calculated for relative pressures of 0.01 to 0.25 using Equation (4.5).

Figure 4.5 shows a representation of the BET surface area versus milling time. The increase in the BET surface area with milling time is in agreement with the decrease in particle size obtained from the XRD measurements. The surface area increases by a factor of four. Since the grain size was found to decrease three orders of magnitude during milling, this is an indication that compacted agglomerates are formed.

4.4 Thermal analysis

The BET surface area of the nanocrystalline sample (anatase) was about $200 \text{ m}^2\text{g}^{-1}$ independent of milling time [93].

4.4 Thermal analysis

The thermal stability of the milled nanocrystalline samples was characterized with a Netzsch STA 429 device in cooperation with the Institut für Bodenkunde (Hannover University). The method consists in heating the sample and an inert reference substance or empty pan at a constant rate. By analyzing the difference in temperature between the sample and the reference, it is possible to determine thermal events, such as melting, decomposition or change in the crystal structure. Furthermore, one can also detect changes in the sample weight as a function of temperature or time which is known as Thermogravimetry (TG).

We used the method of Differential Scanning Calorimetry (DSC) and Thermogravimetry (TG) to characterize the nanocrystalline samples. The samples were dried overnight in a desiccator. The sample weight was about 40 mg and an empty pan was used as a reference. The reference pan and the sample pan weighed about 165 mg. The measurements were carried out under a constant flow of dry air (100 ml/min) and a heating rate of $5 \text{ }^\circ\text{C}/\text{min}$.

Since all the milled samples gave similar results, only the sample milled for two hours will be discussed. Figure 4.6a and 4.6b show the results of the unmilled sample and of the sample milled for two hours, respectively, in a temperature range between 298 and 773 K. The DSC curve presents a broad endothermic peak with a maximum at about 373 K which is related to the loss of adsorbed water from the sample. This peak is found in all samples. The TG curve shows an enormous weight loss of about 9 % which is also present in all samples. Again, this is due to the loss of adsorbed water. This result can be explained by the high surface area of the samples and denotes a high hydrophilicity.

For the unmilled sample a second peak (exotherm) in the DSC curve shows up at about 580 K without a corresponding weight change in the TG curve at the same temperature. Up to now the reason for the appearance of this peak in the unmilled sample is not clear. It may be due to the oxidation of some hydrocarbon at the surface of TiO_2 giving CO_2 and H_2O . The corresponding weight loss could be superimposed with the water loss and therefore not be visible in the TG curve.

4.5 X-ray photoelectron spectroscopy

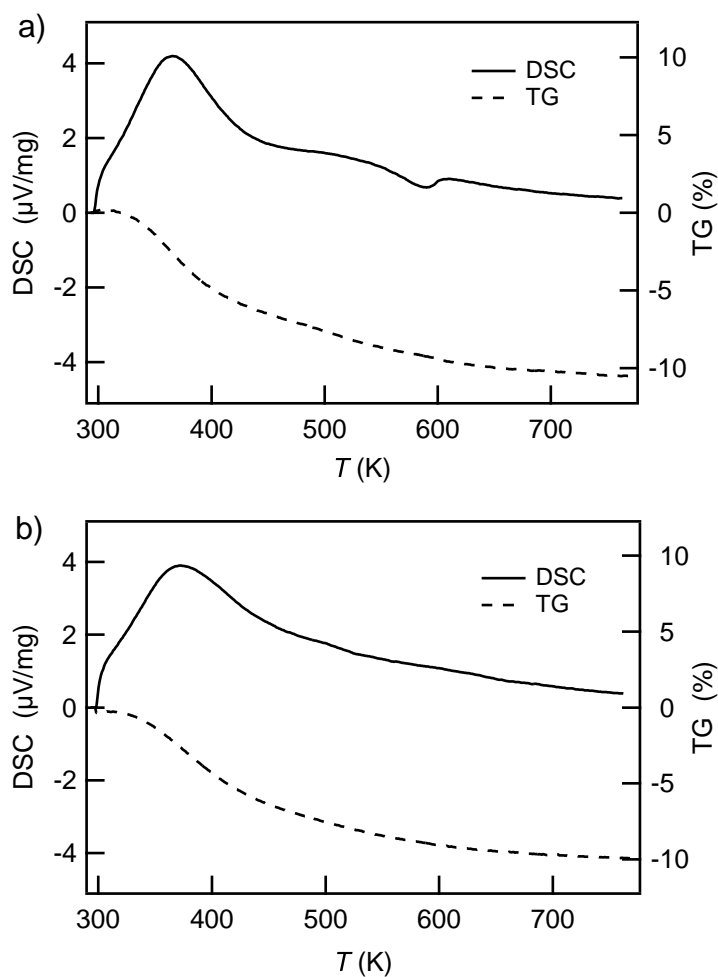


Figure 4.6: DSC and TG curves for the un-milled nanocrystalline anatase sample (a). DSC and TG curves for 2 hours milled nanocrystalline anatase sample (b). A strong weight lost and a broad endothermal peak are observed in both samples, related with water desorption.

4.5 X-ray photoelectron spectroscopy

The electronic structure of the samples was studied by x-ray photoelectron spectroscopy (XPS) in cooperation with the Ruhr-Universität Bochum [92]. Basically, the absorption of a photon from an x-ray source causes the emission of a photoelectron from either a valence or an inner shell of an atom, whose

4.6 Electron paramagnetic resonance spectroscopy

kinetic energy (E_k) is equal to the energy of the absorbed photon ($h\nu$) minus its binding energy (E_b) in the solid:

$$E_k = h\nu - E_b. \quad (4.7)$$

Thus, by measuring the kinetic energy of the emitted photoelectron we may obtain information about the atoms present in the sample. This is particularly interesting in our case since one can analyze the effect of milling on the oxidation state of titanium.

A LeyboldLH 10 spectrometer equipped with a EA10/100 multichannel detector (Specs) was used to measure the spectra. The excitation applied was $\text{MgK}\alpha$ (1253.6 eV, 10 kV \times 20 mA). As a reference the binding energy of adventitious carbon (C1s = 284.5 eV) was used.

Figure 4.7 shows the Ti2p doublet of rutile and anatase, both unmilled and milled for 4 hours. The milled samples are slightly shifted towards lower binding energies. An additional signal is required to reproduce the signal shape (dashed line) which has a binding energy 0.9 eV below that of Ti^{4+} (457.8 eV). This signal may be assigned to Ti^{3+} . From this result we can conclude that the samples are partially reduced during milling.

4.6 Electron paramagnetic resonance spectroscopy

The formation of Ti^{3+} during milling was also confirmed with electron paramagnetic resonance spectroscopy (EPR) measurements in cooperation with the Technische Universität Braunschweig [92].

This technique provides information about the presence of unpaired electrons in the sample, such as those found in many transition metal ions. EPR is closely related to nuclear magnetic resonance (NMR) [95]. The spectra are obtained by varying the magnetic field at constant frequency.

The spectra (Figure 4.8) were recorded at 100 K with a Bruker EMX X-band spectrometer between 100 G and 6900 G using a modulation amplitude of 10 G, a modulation frequency of 100 kHz, and a time constant of 20.48 ms. The intensity of the narrow line centered at $g = 1.96$ increases with milling time and can be attributed to the presence of Ti^{3+} [96,97] whose concentration increases monotonically with milling time. The reason for the

4.6 Electron paramagnetic resonance spectroscopy

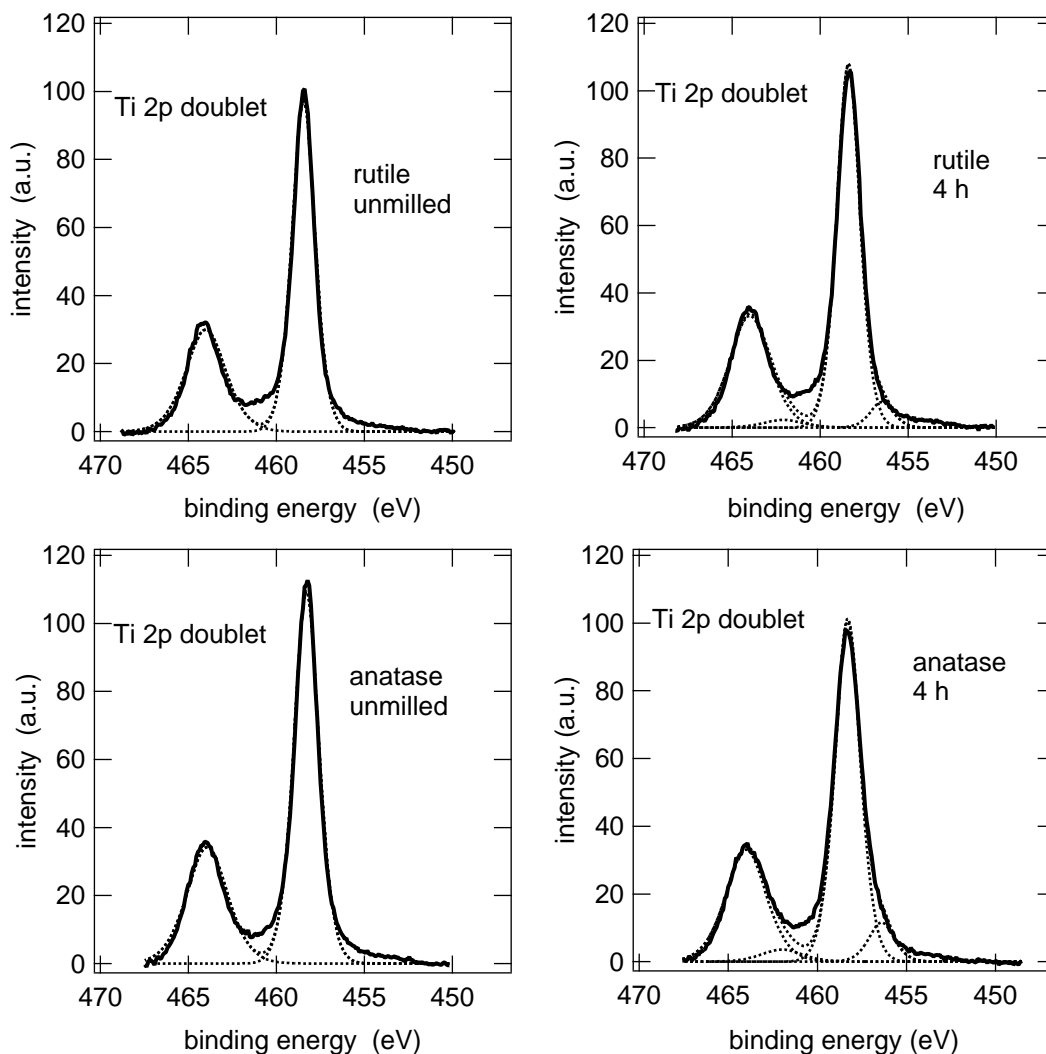


Figure 4.7: XPS spectra for unmilled and 4 hours milled rutile (above) and for unmilled and 4 hours milled anatase (below). The milled samples require an additional signal to reproduce the spectra which may be attributed to the presence of Ti^{3+} in the samples.

broad signal centered at $g = 2.42$ that appears after 2 hours of milling is not clear.

This result corresponds with the one found with XPS and, thus, confirms the formation of Ti^{3+} during milling.

4.7 Scanning electron microscopy

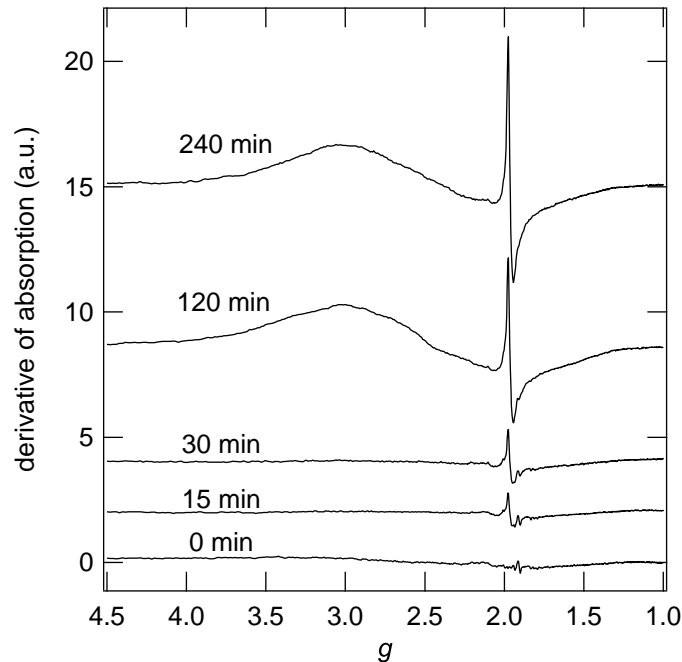


Figure 4.8: EPR signal of milled microcrystalline rutile for different milling times at 100 K. The signal intensities are normalized to the sample weight.

4.7 Scanning electron microscopy

The morphology of the powders was analyzed with scanning electron microscopy (SEM) by Dr. Feldhoff at the Institut für Physikalische Chemie und Elektrochemie (Hannover University). The images were obtained with a JEOL JSM-6700F Field-Emission Scanning Electron Microscope.

SEM images of unmilled and 4 hours milled microcrystalline rutile are shown in figure 4.7. The milled sample present a smaller crystallite size according to the methods mentioned above. During milling the crystallites agglomerate and form bigger particles as expected from the XRD and BET surface area measurements. At the surface of these secondary particles small crystallites can be observed. Both samples present a high porosity.

4.8 Density

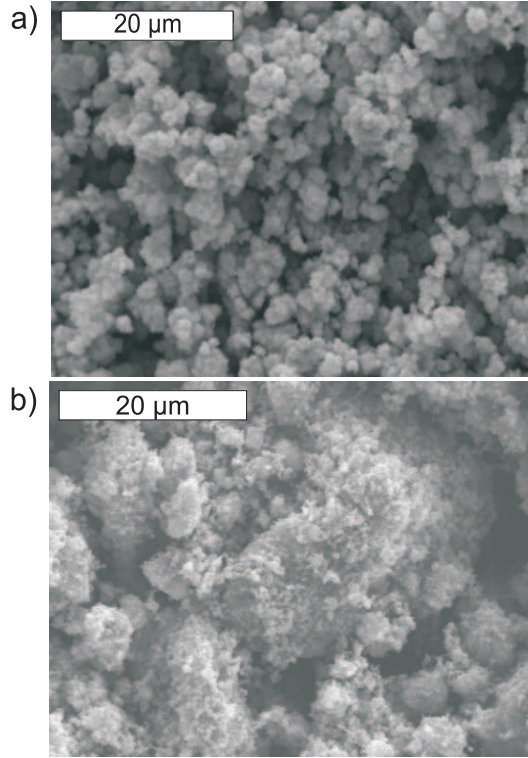


Figure 4.9: SEM images of unmilled rutile (a) and rutile milled for 4 hours (b).

4.8 Density

The density ρ of the micro- and nanocrystalline samples was calculated from their geometry and weight m using the following equation:

$$\rho = m/V = m/(\pi \cdot r^2 \cdot d), \quad (4.8)$$

where V is the volume, r the radius and d the thickness of the pellet. The density of rutile single crystal is $\rho_{\text{rut}}=4.25 \text{ g/cm}^3$ and that of anatase single crystal is $\rho_{\text{ana}}=3.89 \text{ g/cm}^3$. From these values the relative density of the rutile $\rho_{\text{rel}} = \rho/\rho_{\text{rut}}$ and the anatase $\rho_{\text{rel}} = \rho/\rho_{\text{ana}}$ samples can be calculated. The porosity of the sample is given by:

$$\text{Porosity (\%)} = (1 - \rho_{\text{rel}}) \cdot 100. \quad (4.9)$$

4.8 Density

It was found that the microcrystalline samples have a porosity of about 40 % for all milling times. The nanocrystalline samples have a porosity between 40 % and 30 % which decreases with milling time. The density of the pellets can be increased by pressing them at elevated temperatures. However, this process would increase the grain size and modify the properties of the material. Since the measurements have to be compared with measurements on the catalytic activity, the treatment of the samples should not differ much from the one done for catalytic measurements. For this reason the pellets were pressed at room temperature despite the low density obtained.

The porosity of the samples is intergranular which can be seen from the SEM images. Such a high porosity has an effect on the diameter of the grain boundary semicircle in the impedance spectrum. Nevertheless, it does not introduce new semicircles or other properties [59].

Chapter 5

Experimental setup

5.1 Equipment for impedance spectroscopy

Measurements of impedance spectroscopy were carried out with an HP 4192 A impedance analyzer (see Appendix A). This device can apply alternate voltages from 5 mV to 1 V in a frequency range between 5 Hz and 13 MHz to the sample.

Coaxial cables are used to connect the impedance cell to the impedance analyzer. The impedance cell is placed inside a homemade oven [98] which consists of a ceramic tube wrapped with a kandthal wire. Glass wool is used to isolate the oven from the surrounding. The temperature in the cell is measured with a Ni/CrNi thermocouple and it can be varied from room temperature up to 800 °C by an Eurotherm controller. The measurements can be done under vacuum conditions (~ 5 mbar) or in an atmosphere with a given gas composition under atmospheric pressure. The impedance analyzer calculates the conductance (G) and capacitance (C) of the sample at each frequency and the values are recorded on a computer (see Figure 5.1).

Impedance cell

For measuring the samples in parallel plate configuration (as described in Section 3.3) a cell built in the mechanical and electrical workshop of the institute was used (Figure 5.2). The materials used to build the cell are quartz glass and corundum in order to be able to measure at high temperatures. For the same reason the wires used were made of platinum and they are shielded to minimize stray capacitance between them and the ground. The impedance

5.1 Equipment for impedance spectroscopy

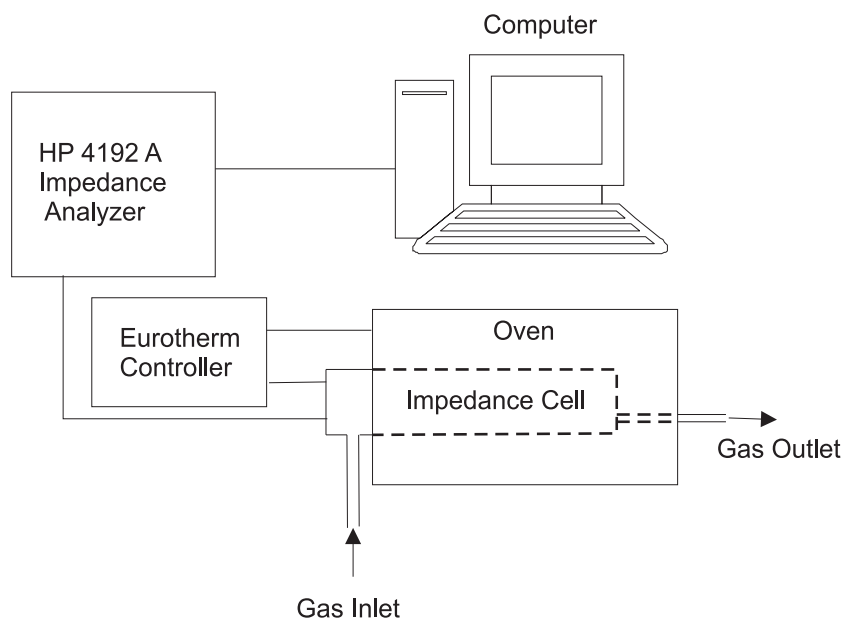


Figure 5.1: Experimental setup for measurements of impedance spectroscopy.

is measured with a four-terminal-pair configuration which combines the advantages of the four terminal method in low impedance measurements (the cable impedance is not measured) while providing the shielding required for high impedance measurements [99]. The cell is about 55 cm long and 35 mm wide (diameter of the outer tube). It consists of three concentric tubes made of quartz glass. The sample is placed between two ceramic cylinders with platinum contacts. Each cylinder is attached to one of the two interior tubes which are joined with each other by two springs so that the sample is tightly held. The outer tube serves as a shell and allows to adjust the atmosphere inside the cell. The platinum wires pass through shielded ceramic tubes (painted with platinum) and are spot-welded with the two platinum contacts (8 mm diameter) at one end and soldered with the BNC cables at the other end of the cell. The temperature of the sample is measured with a device made in the workshop of the institute connected to a Ni/Cr-Ni thermocouple placed near the sample. The temperature is controlled through another Ni/CrNi thermocouple (placed inside the oven) and an Eurotherm controller.

5.2 Equipment for photoconductivity and surface conductivity

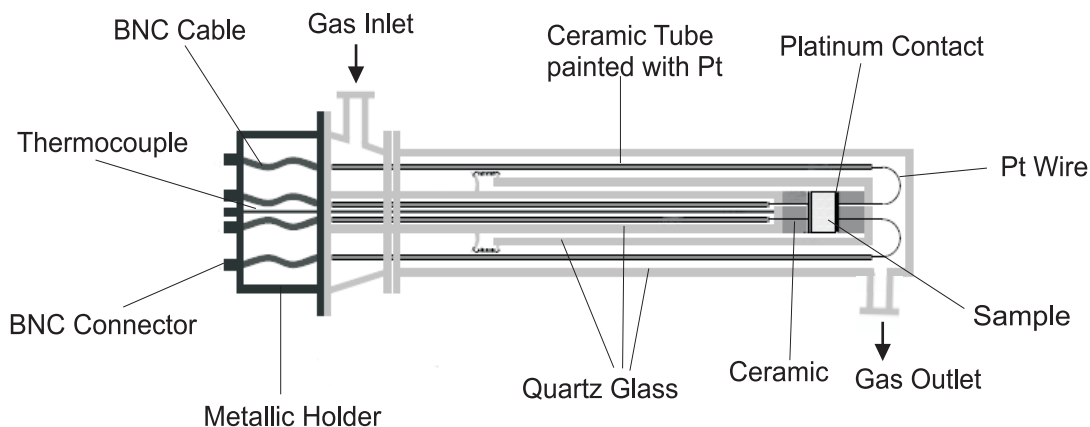


Figure 5.2: Representation of the impedance cell for measuring samples in parallel plate configuration.

5.2 Equipment for photoconductivity and surface conductivity

The experimental setup (Figure 5.3) for photoconductivity and surface conductivity measurements is similar to the one described above. In this case, another impedance cell and an additional light source were used. The HP 4192 A Impedance Analyzer is connected with coaxial cables to the cell. Inside the cell there is a heating element connected to the Eurotherm controller and a Ni/CrNi thermocouple is in contact with the sample in order to measure and control its temperature. Because the cell contains soldered parts and o-rings made of teflon, it can only work in a temperature range between room temperature and $\sim 300^\circ\text{C}$.

The cell is provided with a quartz window that allows illumination of the sample with UV light (300 nm–400 nm). The light source used was a Hg Philips lamp (HPA 400/30 S). The intensity of the light was varied by changing the distance between the lamp and the cell. During these measurements a light intensity between 0.05 and 1 W/cm^2 was used. The atmosphere in the cell can be adjusted to a given composition under atmospheric pressure. Since surface conductivity measurements are very sensitive to moisture, the incoming and leaving gases are dried with phosphor pentoxide before entering and after leaving the cell. For this purpose two desiccators made of glass and brass were used.

5.2 Equipment for photoconductivity and surface conductivity

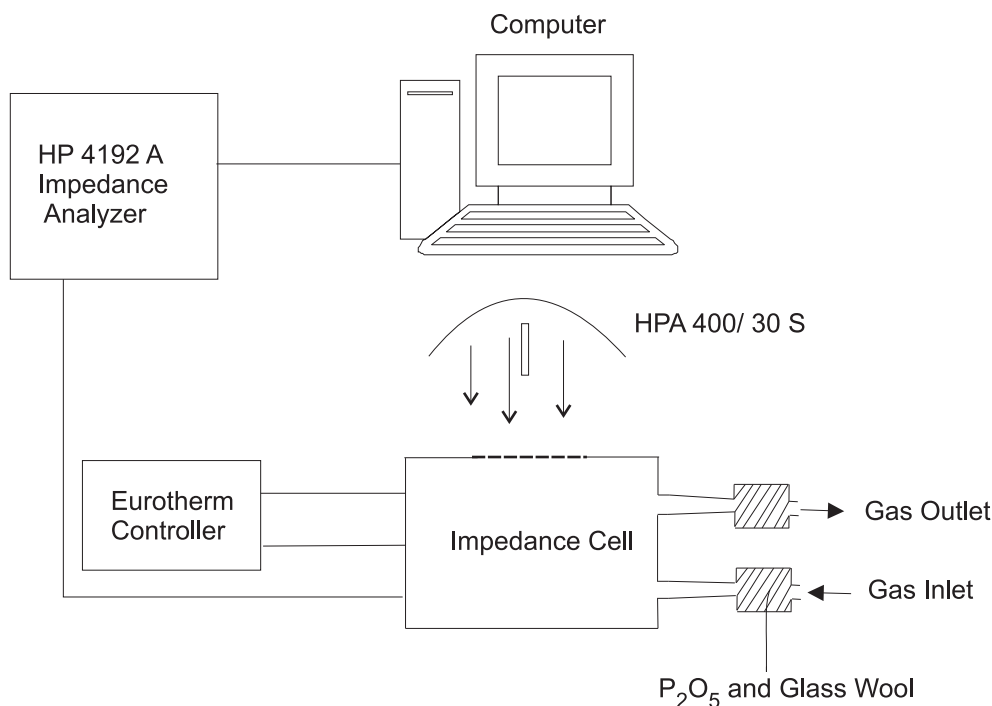


Figure 5.3: Experimental setup for photoconductivity and surface conductivity measurements.

Under steady-state conditions the frequency dependence of the conductivity can be recorded on a computer. In addition, when the system is found away from equilibrium (*e.g.*, after switching on or off the light) the time dependence of the conductivity at a given frequency can also be recorded on a computer.

Photoconductivity and surface conductivity cell

An impedance cell for photoconductivity and surface conductivity measurements was designed and built in the workshop of the institute. The cell consists of a closed stainless steel cylinder (16 cm diameter and 10 cm height) provided with a quartz window on the top (6 cm diameter) so that the sample inside can be illuminated with UV light from above (Figure 5.4). Inside the cylinder there is a table (4 cm diameter) made of stainless steel with a corundum piece attached on the top (2.5 cm diameter) where the sample is placed. A heating element is introduced inside the table and a Ni/CrNi ther-

5.2 Equipment for photoconductivity and surface conductivity

thermocouple is in contact with the sample in order to control its temperature. The cell is provided with a gas inlet and outlet so that the atmosphere inside the cell can be adjusted.

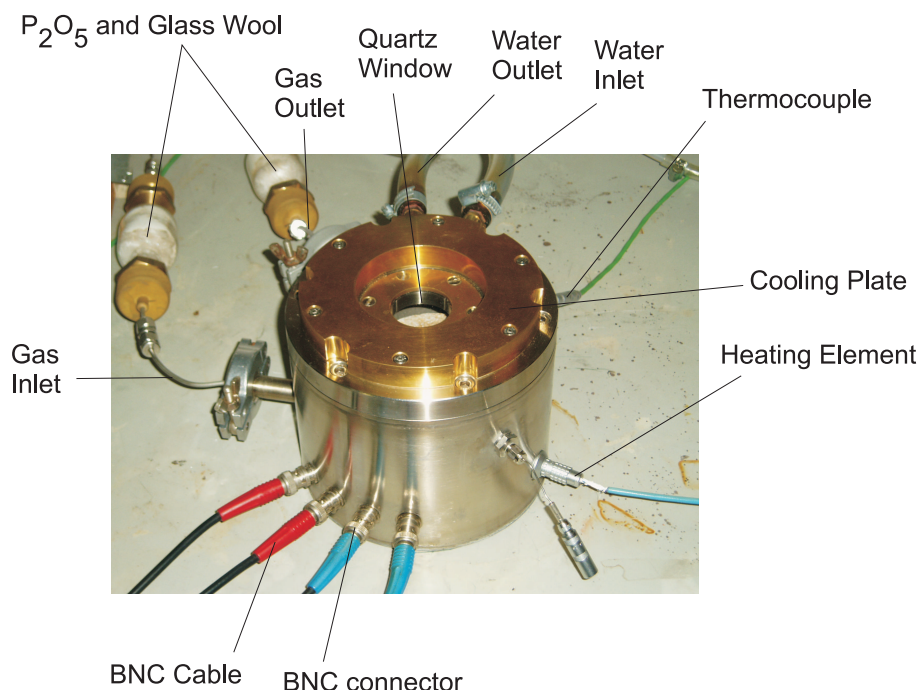


Figure 5.4: Picture of the photoconductivity cell. Inside the cell there is a table made of stainless steel with a corundum piece on top of which the sample is placed (see Fig 5.5).

The table inside the cell is isolated from the surrounding with glass wool (Figure 5.5). Four platinum wires are soldered to the BNC connectors of the cell and are separated as much as possible in order to avoid induced currents. However, the wires pass through a single corundum tube (3 cm long) with four holes before contacting the sample. The possible induced currents in this part of the cell are compensated with an open/short calibration [100]. The corundum tube is forced downwards by means of two springs, so that the wires inside the tube are pressed on the sample. The top cover of the cylinder has a cooling plate which serves to reduce the change in the temperature of the cell after switching on/off the UV light.

The high pressure mercury lamp (HPA 400/30 S) and a quartz reflector (17.5 cm diameter) are held in a stand. The lamp is placed at a distance

5.2 Equipment for photoconductivity and surface conductivity

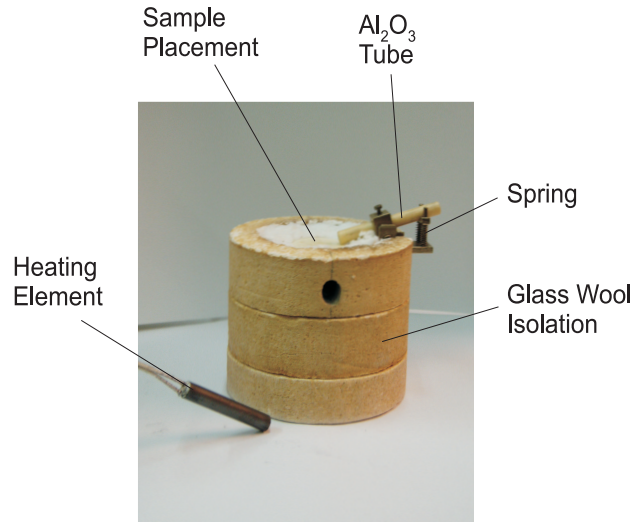


Figure 5.5: Picture of the table placed inside the photoconductivity cell made of stainless steel and isolated with glass wool. The sample is placed on top of a corundum piece. The heating element is introduced inside the table through a hole and a thermocouple is posed in contact with the sample, so that its temperature can be controlled.

coinciding with the focal point of the reflector. By changing the distance of the lamp and reflector from the cell, different light intensities can be achieved.

Chapter 6

Results

6.1 Conductivity of micro-and nanocrystalline TiO_2

Microcrystalline rutile (Acros, 99.95 %) and anatase (Acros, 99 %), and nanocrystalline anatase (Sachtleben, 99.99 %) powders were milled in a high-energy ball mill for milling times between 30 minutes and 4 hours. During the milling process the size of the crystallites decreases down to the nanocrystalline regime and their structure may change (see Chapter 4) affecting the electrical and other properties of the material [52]. The conductivity spectra of the samples were recorded in a temperature range from 298 K up to 973 K and a frequency range from 5 Hz up to 13 MHz. Two different oxygen pressures ($P_{\text{O}_2} = 10^5$ Pa and $P_{\text{O}_2} = 10^2$ Pa) were used. At low temperatures moisture is adsorbed on the surface of the grains and the conductivity increases with decreasing temperature. Therefore, only the high-temperature regime, from 673 K up to 973 K, is shown in the following

6.1.1 Microcrystalline rutile

Figure 6.1 shows the conductivity spectra at high temperatures of microcrystalline rutile, milled for four hours, recorded under vacuum conditions. Similar spectra were recorded for other milling times and atmospheres. As already pointed out by Jonscher [58] the frequency dependence of the conductivity may be expressed with the power law (Equation (2.25))

6.1 Conductivity of micro- and nanocrystalline TiO₂

$$\sigma' = \sigma_{\text{dc}} + A_p \omega^n. \quad (6.1)$$

In the case of microcrystalline rutile the exponent n takes values in the range $0.5 < n < 0.9$ as usual in systems with carrier transport (*e.g.*, electronic hopping, movement of ions) [101].

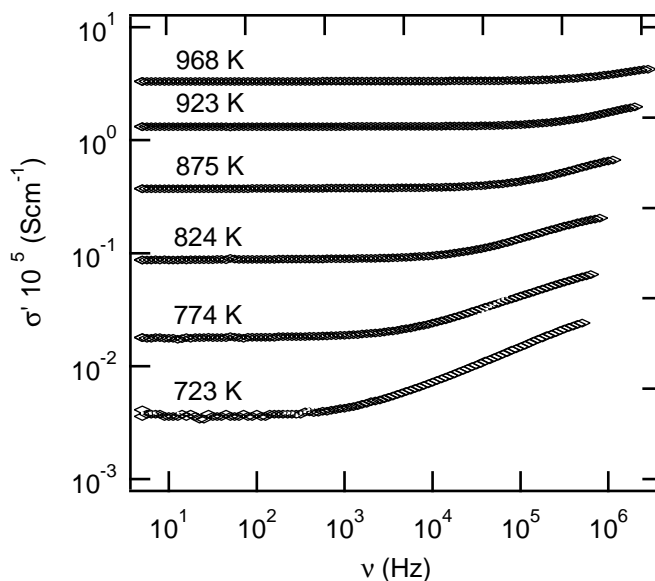


Figure 6.1: Conductivity spectra of microcrystalline rutile milled for 4 hours in a temperature range from 723 K to 966 K and under vacuum conditions ($P_{\text{O}_2} = 10^2$ Pa).

From the Arrhenius plots (Figure 6.2) the activation energies of the conduction process can be calculated. The values are listed in table 6.1.1 for each sample. The unmilled sample has an apparent activation energy of about 2 eV. A similar value for rutile single crystals was found by Blumenthal *et. al.* [12] for the following reaction:



The corresponding apparent activation energy is $E_{\text{A}} = \Delta H_{\text{red},1}/5$ which corresponds to (2.16 ± 0.04) eV. Hence, such a defect model may be assumed for the unmilled sample. Under the oxygen partial pressures used rutile shows

6.1 Conductivity of micro-and nanocrystalline TiO₂

an n-type conductivity and, therefore, there is a loss of lattice oxygen with increasing temperature. At lower oxygen partial pressures the conductivity is higher than under oxygen since there is less oxygen adsorbed on the surface of the particles, which may trap electrons and re-oxidize the material.

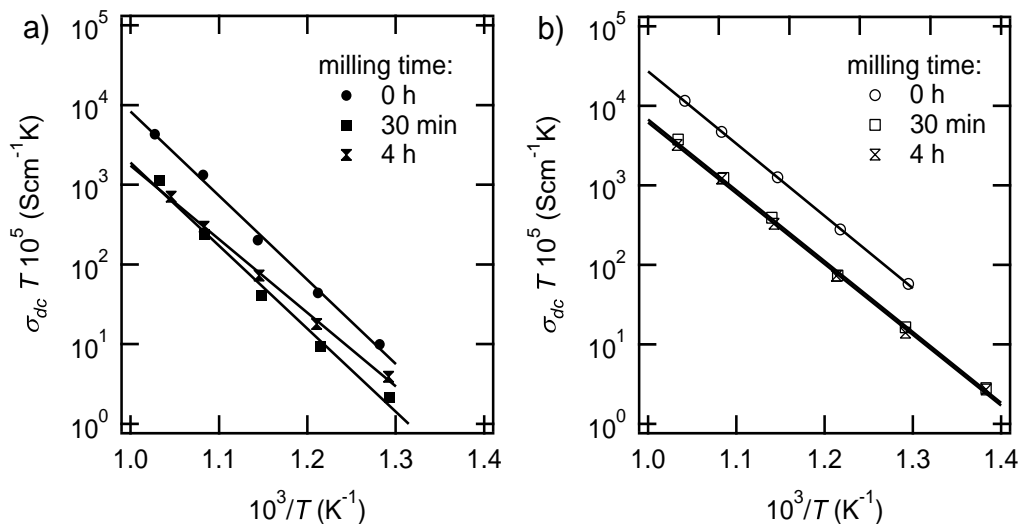


Figure 6.2: Arrhenius representation of the dc conductivity of unmilled and milled microcrystalline rutile under oxygen ($P_{\text{O}_2} = 10^5 \text{ Pa}$) (a) and under vacuum ($P_{\text{O}_2} = 10^2 \text{ Pa}$) (b).

Table 6.1: Activation energies of the microcrystalline rutile samples for different milling times and atmospheres calculated from the Arrhenius plots.

milling time (h)	E_A , oxygen (eV)	E_A , vacuum (eV)
0	2.1 ± 0.1	1.8 ± 0.1
0.5	2.0 ± 0.1	1.76 ± 0.03
4	1.83 ± 0.05	1.76 ± 0.04

The milled samples show a decreasing activation energy with milling time. In this case the generation of titanium interstitials ($\text{Ti}_i^{\bullet\bullet}$) increases the number of defects in the band gap of the material resulting in a decrease of the activation energy. Moreover, the conductivity of the milled samples is low compared to that of the unmilled sample. Since the volume fraction of grain

6.1 Conductivity of micro- and nanocrystalline TiO_2

boundaries is increased with milling time, one may conclude that the grain boundaries act as blocking paths for the conduction (see Section 2.3.2). This result has already been observed in other ceramic materials [48, 63].

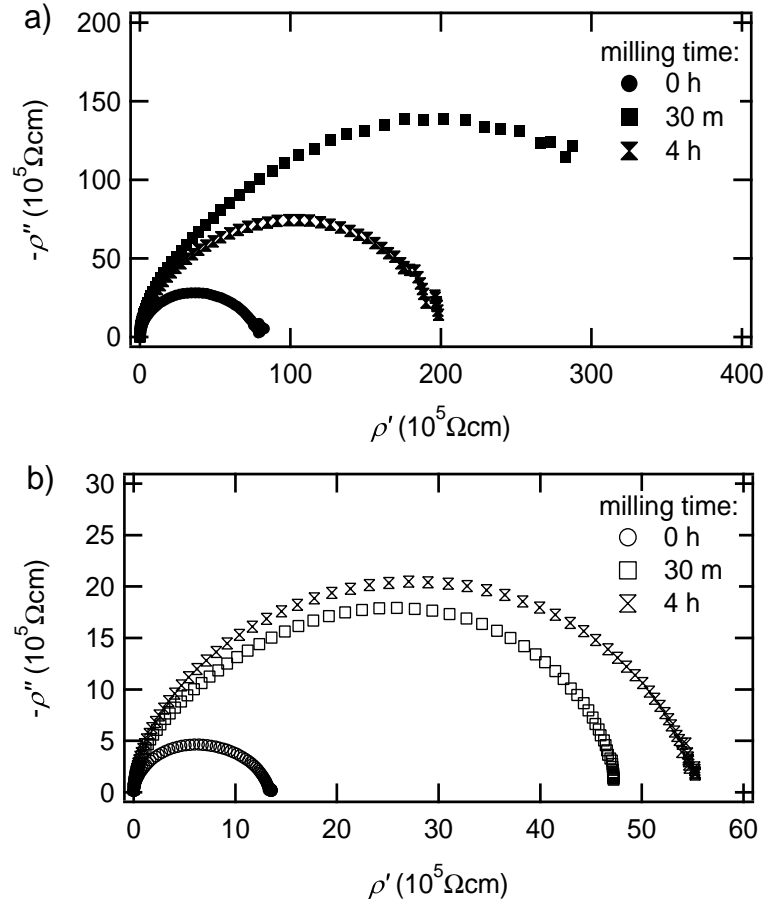


Figure 6.3: Complex plane representation of the resistivity of microcrystalline rutile for different milling times under oxygen ($P_{\text{O}_2} = 10^5 \text{ Pa}$) (a) and under vacuum ($P_{\text{O}_2} = 10^2 \text{ Pa}$) (b) at 773 K.

The complex plane representation of the resistivity is shown in Figure 6.3. The value of the dc conductivity can also be obtained from this representation and is given by the axis intercept of the semicircle. Under oxygen (Figure 6.3a) the conductivity is higher after four hours of milling than after thirty minutes. This result cannot be explained by an increase of the volume

6.1 Conductivity of micro-and nanocrystalline TiO₂

fraction of blocking paths (grain boundaries) and therefore, may be related to a change in the crystalline structure. The semicircles are broader than expected for an ideal semicircle which indicates the overlap of two semicircles. One semicircle corresponds to the response of the bulk and the other one to that of the grain boundaries. However, their capacities are similar since it is not possible to distinguish between them (see Section 2.3).

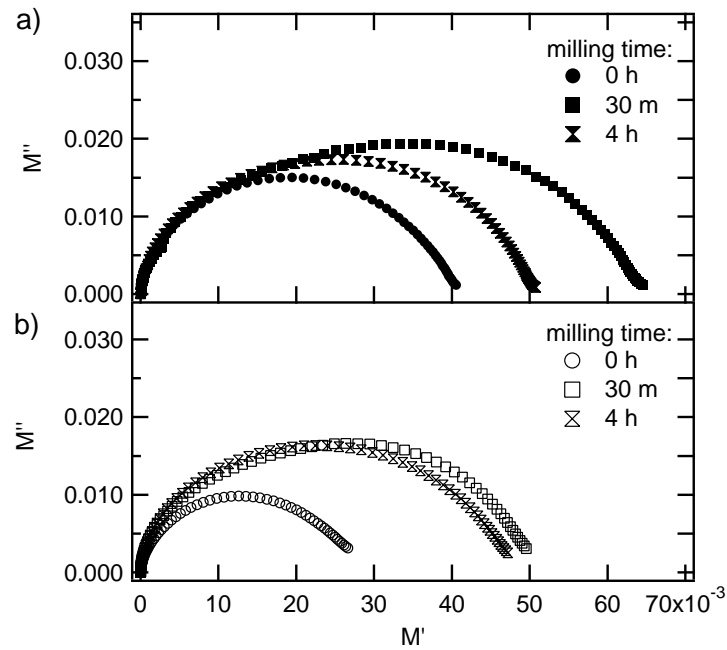


Figure 6.4: Complex plane representation of the modulus of microcrystalline rutile milled for different times oxygen ($P_{O_2} = 10^5$ Pa) (a) and under vacuum ($P_{O_2} = 10^2$ Pa) (b) at 773 K.

The modulus representation (Figure 6.4) also shows a typical response for two overlapping semicircles. Since the relaxation times for the bulk and the grain boundary processes are not so much different, it is not possible to differentiate between them. In particular, the resistance of the bulk and the grain boundaries are very similar.

6.1.2 Microcrystalline anatase

Analogous measurements were done for the microcrystalline anatase samples. Figure 6.5 shows the conductivity spectra, recorded under vacuum conditions, of the sample milled for four hours. The exponent n takes values between 0.8 and 0.9 which is known for systems with carrier transport. However, the sample milled for four hours presents values of about 0.4 which are found in polymers and glasses at temperatures above the glass transition temperature [67, 102, 103]. This fact points out the amorphous nature of the sample milled for four hours.

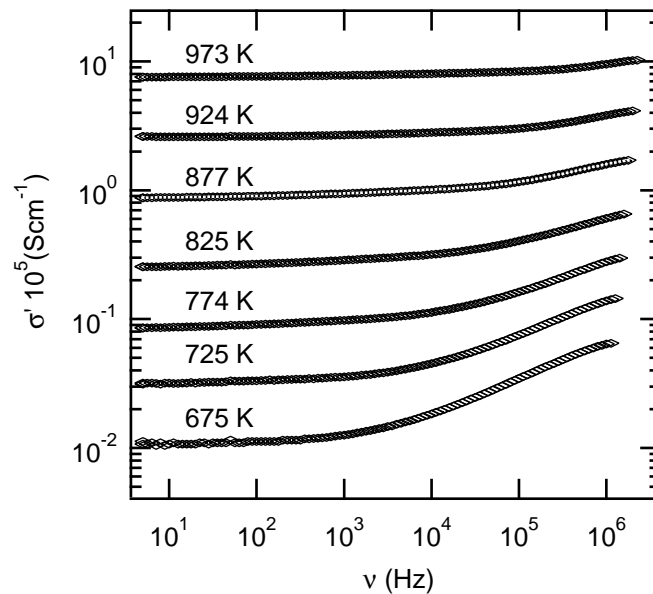


Figure 6.5: Frequency dependence of the conductivity of the microcrystalline anatase sample milled for four hours.

The activation energies are calculated from the Arrhenius plots (Figure 6.6) and are listed in Table 6.2. Clearly, the values are lower than those found for rutile, so that a different conduction mechanism is present in anatase. The unmilled sample has an activation energy of about 0.9 eV. This is in agreement with measurements done by Knauth and Tuller [21], who found that, under the same oxygen partial pressures and similar temperatures, anatase has a p-type conductivity. They proposed the following defect model for the conduction mechanism:

6.1 Conductivity of micro-and nanocrystalline TiO₂



The apparent activation energy is then given by $E_A = \Delta H_{\text{ox}}/4$ which corresponds to $(0.8 \pm 0.1) \text{ eV}$. As expected for p-type conduction, the conductivity is higher under oxygen than under vacuum conditions, in contrast to the results obtained for rutile.

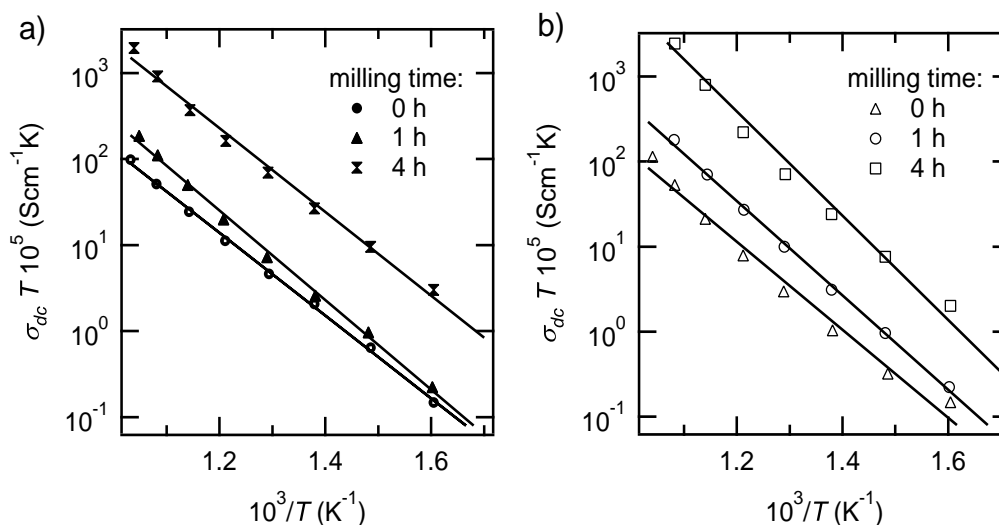


Figure 6.6: Arrhenius representation for the microcrystalline anatase samples under oxygen ($P_{\text{O}_2} = 10^5 \text{ Pa}$) (a) and under vacuum ($P_{\text{O}_2} = 10^2 \text{ Pa}$) conditions (b).

Table 6.2: Activation energies of the microcrystalline anatase samples under different atmospheres calculated from the Arrhenius plots.

milling time (h)	E_A , oxygen (eV)	E_A , vacuum (eV)
0	0.95 ± 0.01	1.02 ± 0.05
1	1.03 ± 0.01	1.09 ± 0.02
4	0.97 ± 0.03	1.21 ± 0.06

With increasing milling time the size of the crystallites diminishes, the volume fraction of grain boundaries increases as well as the number of defects

6.1 Conductivity of micro- and nanocrystalline TiO₂

like titanium interstitials and oxygen vacancies. Because the conductivity increases with increasing milling time (see Figure 6.7), it can be concluded that the grain boundaries have a smaller resistance than the bulk region and therefore, act as fast conduction paths (in contrast to the results obtained for rutile). This has already been observed in other ceramic materials like *e.g.*, CaF₂ [104]. The activation energies of the milled samples are about 1 eV. Since the conduction takes place mainly via highly defective grain boundaries, one may assume that conduction is governed by ionic conductivity, which is known to have an activation energy around 1 eV [21]. The majority species are titanium interstitials which have a larger mobility than oxygen ions in titanium dioxide [13].

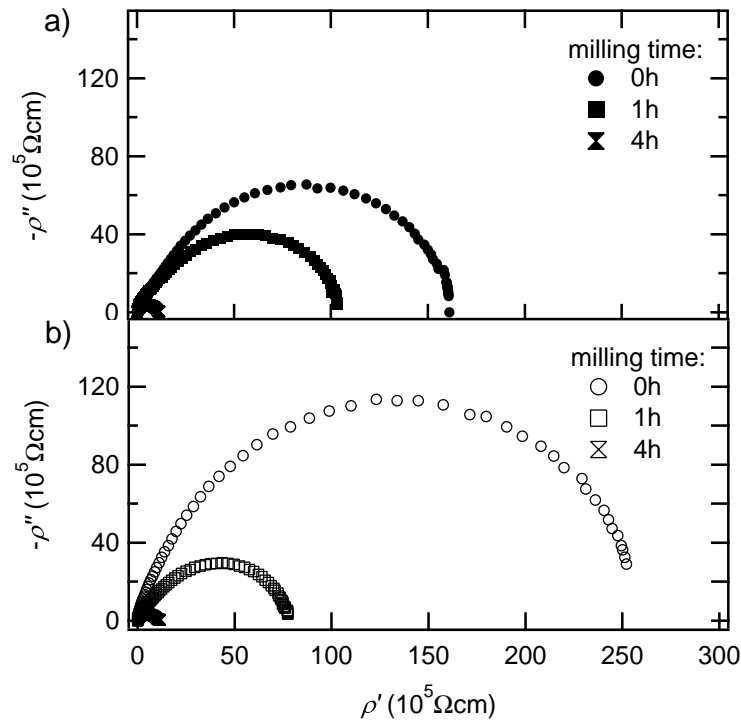


Figure 6.7: Complex plane representation of the resistivity of microcrystalline anatase milled for different times and under different atmospheres: oxygen ($P_{O_2} = 10^5$ Pa) (a) and vacuum ($P_{O_2} = 10^2$ Pa) (b) at 773 K.

The complex plane representation of the resistivity (Figure 6.7) shows a

6.1 Conductivity of micro-and nanocrystalline TiO₂

single semicircle for all milling times and atmospheres. This denotes that the capacitances of the grain boundaries and the bulk region are very similar.

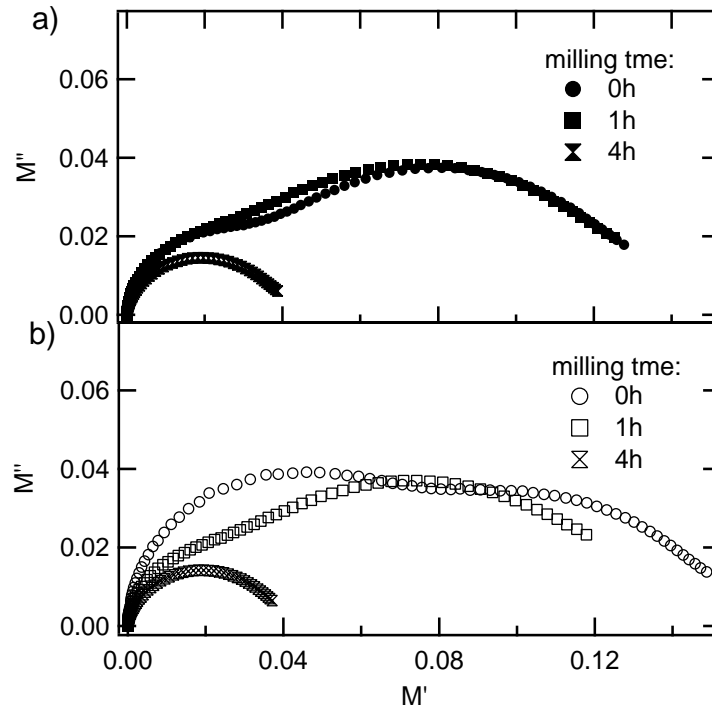


Figure 6.8: Complex plane representation of the modulus of milled microcrystalline anatase milled for different times and under different atmospheres: oxygen ($P_{\text{O}_2} = 10^5$ Pa) (a) and vacuum ($P_{\text{O}_2} = 10^2$ Pa) (b) at 773 K.

In contrast to that finding, the complex plane representation of the modulus (Figure 6.8) shows two overlapping semicircles except for the sample milled for four hours. Such a behavior is found in samples where the resistance of the bulk and the grain boundaries are different. This is in accordance with the assumption that the conductivity is higher in the grain boundaries.

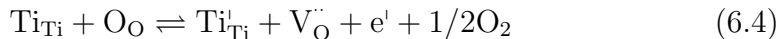
After four hours of milling the contribution of the grain boundaries to the conduction is much higher than that of the bulk, so that only one semicircle can be seen. This fact is also in agreement with the low exponent ($n \simeq 0.4$) found for this sample which denotes the presence of highly defective grain boundaries.

6.1.3 Nanocrystalline anatase

The nanocrystalline anatase samples were also milled between 30 minutes and 4 hours. Similar conductivity spectra like the ones shown for the microcrystalline samples (see Figure 6.2 and Figure 6.6) were recorded under oxygen and under vacuum. The exponent n takes typical values for systems with electronic hopping or ionic conductivity (*i.e.*, $0.5 < n < 0.9$).

The activation energies calculated from Figure 6.9 are listed in Table 6.3. Knauth and Tuller [21] concluded from their measurements, that the conduction mechanism in nanocrystalline anatase is ionic in nature in the region of oxygen partial pressures used here. They found an activation energy of (1.0 ± 0.1) eV in agreement with the values for the unmilled sample. Hoshino *et. al.* [9] found an activation energy of (0.7 ± 0.1) eV for the migration of both tetravalent and trivalent titanium interstitials in TiO₂. Hence, one may assume an ionic conduction mechanism and interstitial titanium ions as the majority species.

As a function of the milling time there is a minimum at about 30 minutes in the activation energy. Since the value still lies in the range of 1 eV, this minimum is assigned to ionic conduction in a highly defective system with lower potential barriers. As one continues milling, the activation energy increases. Obviously, the structure of the crystallites has changed and now another conduction mechanism controls the conductivity. The higher activation energies found may be explained by the following reduction:



with the equilibrium constant

$$K = a^3 P_{\text{O}_2}^{1/2}, \quad (6.5)$$

where a is the activity of the electrons, the titanium interstitials and the oxygen vacancies, and P_{O_2} is the oxygen partial pressure. The enthalpy of this reaction is $\Delta H_{\text{red},2} = 410$ kJ/mol [18] resulting in an apparent activation energy of $E_{\text{A}} = 1.42$ eV. Hence, we conclude that for milling times longer than about 30 minutes, one has n-type conductivity.

From the complex plane diagram of the resistivity (Figure 6.10) two overlapping semicircles can be distinguished. This is possible when the capacitances of the grain boundaries and the bulk are quite different. It is indicated by this fact that the structure of the grain boundaries and the bulk differ

6.1 Conductivity of micro- and nanocrystalline TiO₂

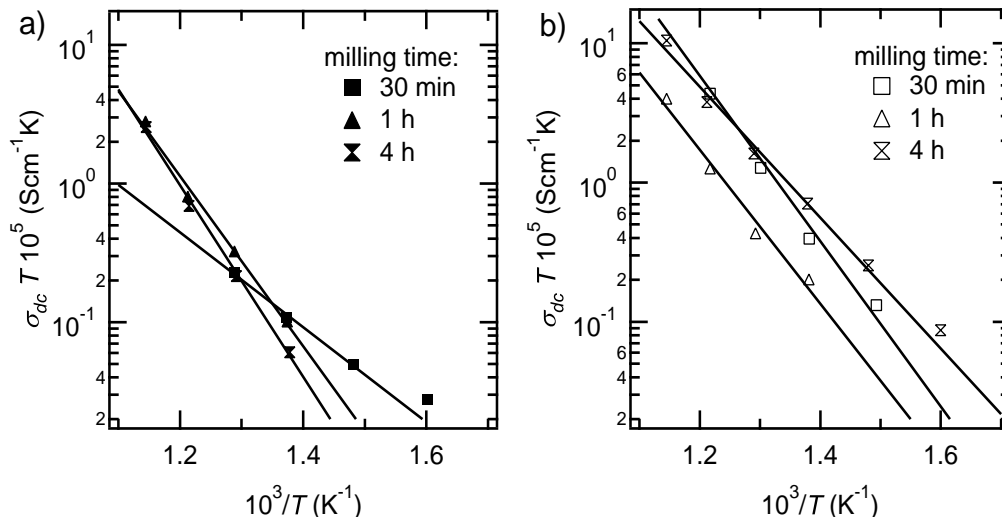


Figure 6.9: Arrhenius representation of nanocrystalline anatase milled for different times and under different atmospheres: oxygen ($P_{O_2} = 10^5$ Pa) (a) and vacuum ($P_{O_2} = 10^2$ Pa) (b).

Table 6.3: Activation energies of the nanocrystalline anatase samples under oxygen and vacuum calculated from the Arrhenius plots shown in Figure 6.9.

milling time (h)	E_A , oxygen (eV)	E_A , vacuum (eV)
0	1.0 ± 0.1	1.2 ± 0.3
0.5	0.68 ± 0.04	1.18 ± 0.07
1	1.22 ± 0.07	1.1 ± 0.1
2	1.3 ± 0.1	1.38 ± 0.01
4	1.37 ± 0.06	0.93 ± 0.05

considerably, probably due to a higher concentration of defects in the grain boundaries or to the presence of a new phase at the surface of the crystallites. The modulus diagram (Figure 6.11) does not allow the differentiation of two semicircles. This is found when the resistance of the bulk and of the grain boundaries are similar or when one of them is much higher. In this case, we know from measurements on milled microcrystalline anatase (see Section 6.1.2) that conduction via grain boundaries is higher.

Figure 6.12 shows that the conductivity increases with milling time (excluding the maximum at about 30 minutes). Since milling does not increase

6.1 Conductivity of micro- and nanocrystalline TiO₂

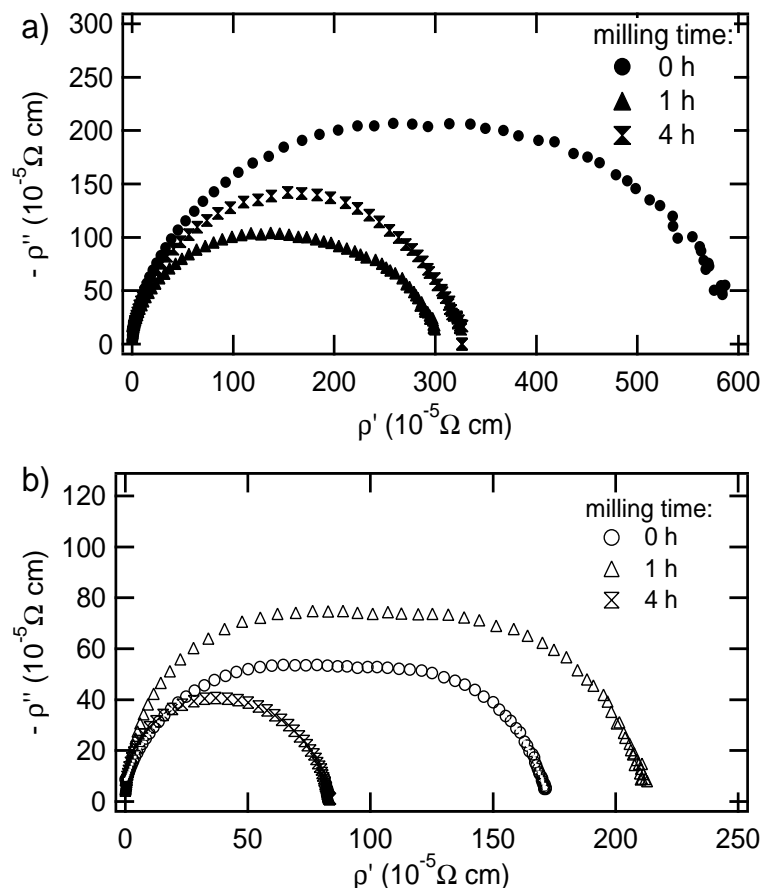


Figure 6.10: Complex plane representation of the resistivity of nanocrystalline anatase for different milling times and measured under oxygen ($P_{\text{O}_2} = 10^5 \text{ Pa}$) (a) and vacuum ($P_{\text{O}_2} = 10^2 \text{ Pa}$) conditions (b) at 873 K.

the volume fraction of grain boundaries one may interpret this increase as due to a higher number of defects at the grain boundaries.

The maximum found in dc conductivity at about 30 minutes milling time may correspond to a phase transition near the surface of the crystallites. After 30 minutes of milling a high concentration of defects is present near the surface of the crystallites. Since the value of the conductivity and the activation energy depend on the oxygen partial pressure, we conclude that we have different mechanisms at each atmosphere. Under 10^5 Pa of oxygen one

6.1 Conductivity of micro- and nanocrystalline TiO₂

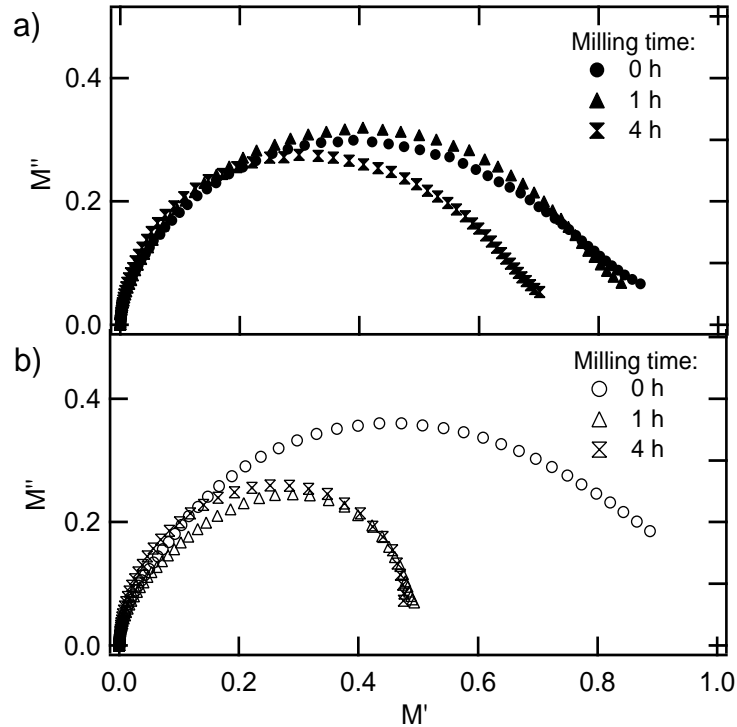


Figure 6.11: Complex plane diagram of the modulus of nanocrystalline anatase milled for different milling times and measured under oxygen ($P_{O_2} = 10^5$ Pa) (a) and under vacuum ($P_{O_2} = 10^2$ Pa) conditions (b) at 873 K.

may assume ionic conductivity because the activation energy ($E_A = (0.68 \pm 0.04)$ eV) is in accordance with literature values for diffusion of titanium interstitials in TiO₂ [9]. Under vacuum conditions ($P_{O_2} = 10^2$ Pa) reduction of the system takes place, leading to an increase of the activation energy and of the conductivity. Both mechanisms occur predominantly near the surface region of the crystallites where the defect concentration is higher. If we continue milling, the defects may associate and build a reduced phase. This new phase may act as a recombination center for the free electrons in the conduction band and/or as a blocking path for the movement of ions, which would explain the decrease in conductivity. The reduction of the system after 30 minutes milling is not so easy due to the presence of a reduced phase near the surface of the crystallites and, hence, the activation energy increases.

6.2 Surface conductivity of TiO₂ single crystal

The maximum found under vacuum at 30 minutes milling time is only supported by one point. However, it is in agreement with the one found under oxygen and with the assumption of a phase transition near the surface of the grains. Therefore, it is regarded as reliable.

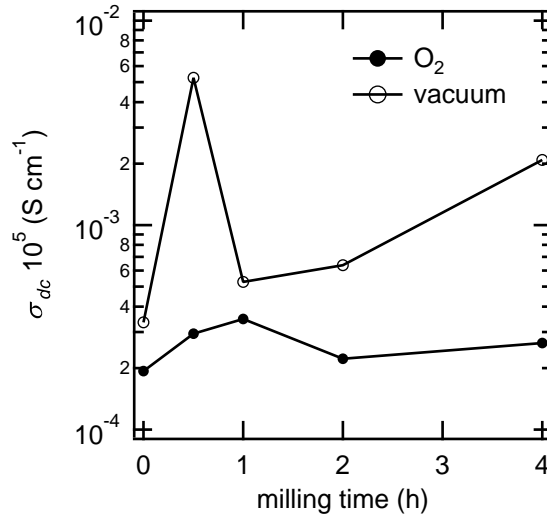


Figure 6.12: Variation of the dc conductivity with the milling time at 873 K under $P_{O_2} = 10^2$ Pa (open circles) and under $P_{O_2} = 10^5$ Pa (dark circles).

6.2 Surface conductivity of TiO₂ single crystal

In addition to the measurements on micro- and nanocrystalline samples, the surface conductivity (in the dark) of a TiO₂ (100) single crystal was studied. For these measurements the cell described in Section 5.2 was used. The measurements were done in a temperature range from 298 K up to 573 K and under two different atmospheres, *i.e.*, oxygen and nitrogen. An alternating voltage of 1 V was applied to the sample in a frequency range from 5 Hz to 100 kHz. Since surface conductivity measurements are very sensitive to humidity, the incoming gas was dried with phosphor pentoxide. The influence of atmosphere, temperature and measuring frequency on the surface conductivity was studied.

6.2 Surface conductivity of TiO₂ single crystal

6.2.1 Influence of atmosphere

It was found that the surface conductivity is very sensitive to the oxygen partial pressure. Upon changing the atmosphere from oxygen to nitrogen (below 5 ppm of oxygen) the surface conductance at 573 K in the dark increases by about three orders of magnitude (0.04 μS - 300 μS) (see Figure 6.13).

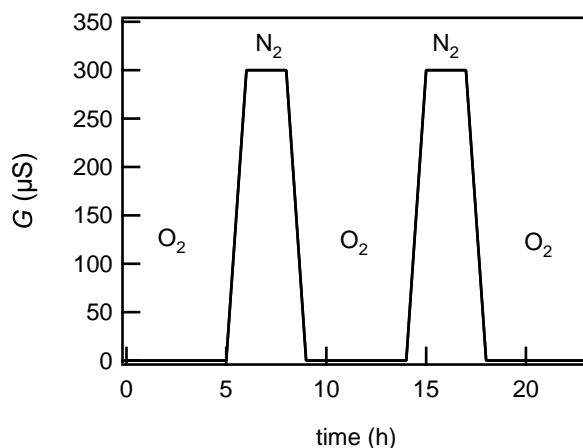


Figure 6.13: Histogram of the influence of the oxygen partial pressure on the surface conductance of TiO₂ (100) single crystal at 300 °C.

The reason for this increase may be related to two different processes. These may be, on the one hand, the desorption of adsorbed oxygen and, on the other hand, a change in the surface structure. The histogram in Figure 6.13 shows that the influence of oxygen/nitrogen on the surface conductance is completely reversible.

6.2.2 Influence of temperature and measuring frequency

The surface conductivity was measured under a constant flow rate (50 ml/min) of oxygen at temperatures between 298 K and 573 K. Under equilibrium conditions, *i.e.*, when the surface conductivity remained constant with time, the frequency dependence was measured. The results are shown in Figure 6.14.

In the low temperature region there is a strong dispersion of the conductivity at low frequencies. This behavior is often observed in surface conductivity measurements [58] and is known as low frequency dispersion (LFD)

6.2 Surface conductivity of TiO₂ single crystal

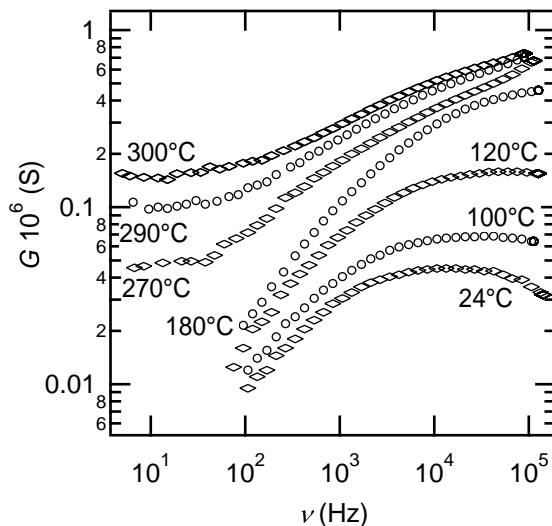


Figure 6.14: Frequency dependence of the surface conductivity of TiO₂ single crystal under oxygen atmosphere, showing LFD behavior at low temperatures.

(see Section 2.5). In the high temperature region one observes the usual behavior of the bulk described with a power law at high frequencies and a dc plateau at low frequencies. The frequency dependence of the real part of the conductivity can be expressed with Equation (2.34):

$$\sigma'(\omega) = A_l \omega^{n_1} + A_h \omega^{n_2}, \quad (6.6)$$

where ω is the angular frequency ($\omega = 2\pi\nu$), the exponent n_1 and the pre-exponential factor A_l describe the relaxation at low frequencies, while n_2 and A_h describe the relaxation at high frequencies.

Figure 6.15 shows the temperature dependence of the surface conductance at a given frequency. With increasing temperature two minima are found for the surface conductivity at $\sim 100^\circ\text{C}$ and at $\sim 200^\circ\text{C}$. At these temperatures the time needed to reach equilibrium is particularly long, and of the order of many hours. The first minimum which shows up at $\sim 100^\circ\text{C}$ may be assigned to the physisorption of oxygen whereas the second one which appears at $\sim 200^\circ\text{C}$ may be due to a further oxidation of the surface or to a change in its structure. While decreasing the temperature the surface remains in a reduced state which indicates the formation of oxygen vacancies at high temperatures.

6.3 Photoconductivity of TiO₂ single crystal

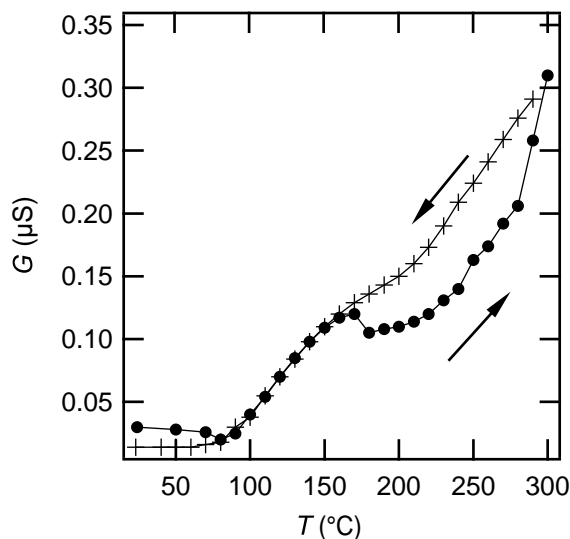


Figure 6.15: Temperature dependence of the surface conductivity of a TiO₂ (100) single crystal under oxygen ($P_{O_2} = 10^5$ Pa).

6.3 Photoconductivity of TiO₂ single crystal

The photoconductivity of a TiO₂ (100) single crystal was measured using the experimental setup described in Section 5.2. The time needed to reach equilibrium after switching on/off the UV light was studied in a temperature range from 298 K up to 573 K. When the conductivity remained constant with time, *i.e.* under steady state conditions, the frequency dependence of the conductivity was recorded. An alternating voltage of 1 V was applied to the single crystal in a frequency range from 5 Hz up to 100 kHz. Two different atmospheres, *i.e.* oxygen and nitrogen, were used to investigate the effect of the ambient gas on the photoconductivity of the material. During these measurements light intensities I from 0.05 W/cm² up to 1.4 W/cm² were used by changing the distance of the light source to the cell.

6.3.1 Influence of atmosphere

The photoconductivity (surface conductivity under illumination) of titanium dioxide varies considerably depending on the atmosphere present in the cell.

6.3 Photoconductivity of TiO₂ single crystal

When the sample is illuminated with UV light under oxygen, the surface conductivity increases by about two orders of magnitude (from 0.04 μS up to 7 μS) (Figure 6.16). Changing the atmosphere to nitrogen (below 5 ppm

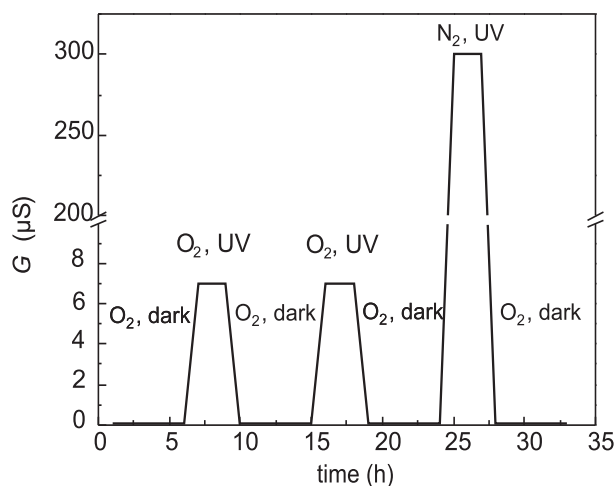


Figure 6.16: Influence of the atmosphere on the photoconductance at 300 °C and a light intensity of 1.4 W/cm².

of oxygen) leads to an even higher value of the surface conductivity which is independent of the illumination (cf. Figure 6.13). As already mentioned in Section 6.2.1, this increase in the photoconductivity can be explained by the desorption of oxygen or/and a change in the surface structure. Under oxygen, the absorption of UV light leads to one or both of these processes whereas under nitrogen the absorption of UV light has a negligible effect on the surface conductivity.

6.3.2 Influence of time

Typical relaxation curves for the rise and decay of the photoconductivity at a given temperature and a given light intensity are shown in Figure 6.17. Similar curves were recorded at different temperatures and light intensities.

The rise curve shows two regimes. First, a fast increase is observed followed by a slower increase of the photoconductivity. The first of these processes reaches equilibrium after some seconds. Since relaxation processes between electrons in the conduction band and holes in the valence band lie

6.3 Photoconductivity of TiO₂ single crystal

in the range of $10^{-14} \text{ s} \leq \tau \leq 10^3 \text{ s}$ [69] and adsorption kinetics take place in the order of seconds or less [71], one can attribute this fast rise to a combination of these processes.

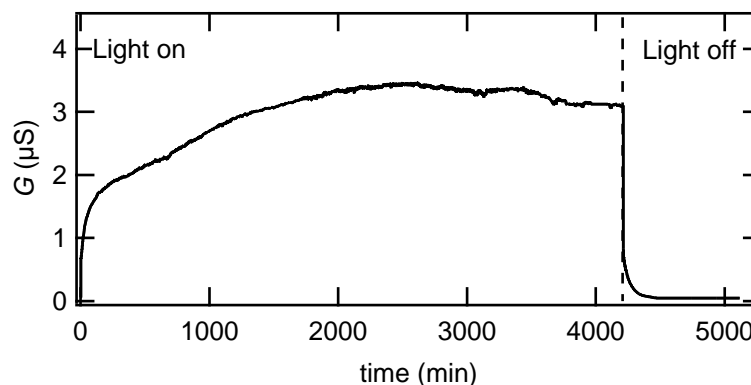
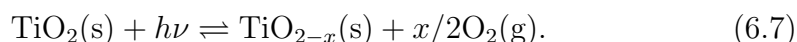


Figure 6.17: Relaxation curves of the photoconductance near the surface of TiO₂ (100) single crystal under oxygen ($P_{\text{O}_2} = 10^5 \text{ Pa}$) at a constant temperature (150 °C) and light intensity (1.4 W/cm²).

The second one, *i.e.*, the slower one takes many hours or even days to reach equilibrium. These long times needed to reach equilibrium reveal the presence of some kind of solid state reactions which also take place in the range of hours. The proposed reaction to explain this slow increase should have free electrons as product species in the conduction band and can therefore be written as follows:



This means that, under illumination, electrons from the lattice oxygens (O^{2-}) are being excited to the conduction band leaving O^- and O species near the surface, which may easily recombine and leave the solid to form $\text{O}_2(\text{g})$. Equation (6.7) is analogous to the thermal formation of oxygen vacancies with the difference that in this case the solid is previously activated by the absorption of photons with an energy corresponding to the band-gap of the catalyst.

The decay of the photoconductivity also shows a fast and a slow regime, which can be explained with the same arguments as for the rise.

6.3 Photoconductivity of TiO₂ single crystal

When equilibrium under illumination was achieved, the frequency dependence of the photoconductivity was recorded. In this case a plateau of dc conductivity is found at all temperatures, as expected for a system with delocalized electrons in the conduction band.

6.3.3 Influence of temperature

Figure 6.18 shows the temperature dependence of the steady state photoconductance. From the peak found at about 200 °C we conclude that there is first-order phase transition [105] at this temperature near the surface of the crystal. Such a phase transition has already been observed in the literature for single crystalline TiO₂ [106].

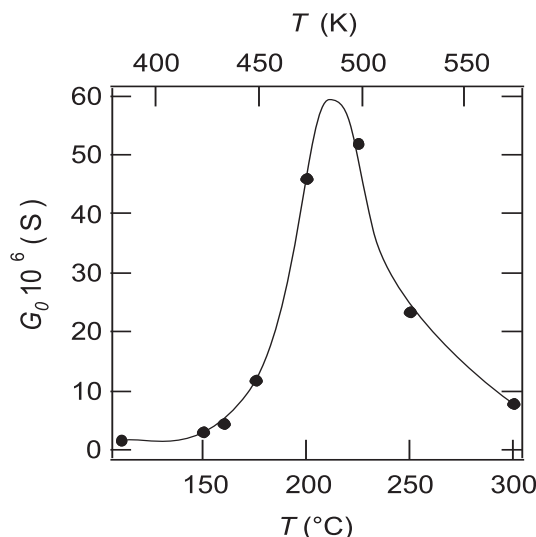


Figure 6.18: Temperature dependence of the steady-state photoconductance under oxygen ($I = 1.4 \text{ W/cm}^2$). The solid line is drawn to guide the eye.

This result supports the idea of a solid state reaction activated by light. Below $\sim 200 \text{ °C}$ one has the formation of oxygen vacancies as described by Equation (6.7), which releases electrons in the conduction band and, hence, increases the photoconductivity. At the transition temperature ($\sim 200 \text{ °C}$) a threshold concentration of oxygen vacancies is achieved which collapses leading to the formation of a reduced phase near the surface. The recombination

6.3 Photoconductivity of TiO₂ single crystal

time is much higher in the phase generated at temperatures above $\sim 200^\circ\text{C}$ resulting in a decrease of the steady state photoconductivity.

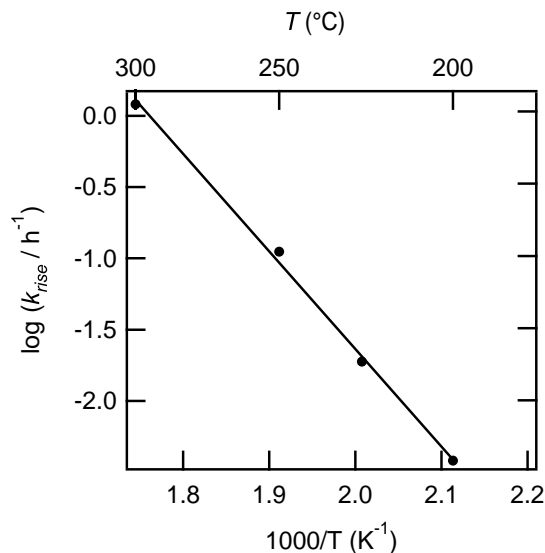


Figure 6.19: Arrhenius plot of the reaction rate for the phase transition above $\sim 200^\circ\text{C}$ under oxygen and a light intensity of $1.4 \text{ W}/\text{cm}^2$. From the slope of the curve $E_A = (1.35 \pm 0.05) \text{ eV}$ is obtained.

The phase formed under illumination is re-oxidized when the light is switched off (see Figure 6.16).

It is known that oxygen vacancies in reduced TiO₂ collapse and form crystallographic shear planes (CSP)(see, *e.g.*, [107]). Therefore, this maximum can be interpreted as a transition between a surface with a high concentration of oxygen vacancies and a surface with crystallographic shear planes.

Figure 6.19 shows an Arrhenius representation of the reaction rate ($k_{\text{rise}} = 1/\tau_{\text{rise}}$) above $\sim 200^\circ\text{C}$. In this temperature region we have the creation of oxygen vacancies followed by a phase transformation. Since the apparent activation energy is $(1.35 \pm 0.05) \text{ eV}$, we may describe the reduction process by Equation (6.4), yielding a value of 390 kJ mol^{-1} for $\Delta H_{\text{red},2}$. This value is close to the value of 410 kJ mol^{-1} found in the literature [18, 19]. Note, that the educt species are activated by the absorption of UV light. The same reaction takes place, to a smaller extent, in the dark above $\sim 200^\circ\text{C}$ (see Figure 6.15). Using the experimental results depicted in Figure 6.14, an

6.3 Photoconductivity of TiO₂ single crystal

apparent activation energy of (1.3 ± 0.1) eV is obtained which corresponds to the value found under illumination.

The time constant of reaction (6.7) changes considerably with temperature (Figure 6.20). For light intensities as high as 1.4 W/cm^2 , applied here, one would expect a constant relaxation time with temperature if only relaxation processes between electrons in the conduction band and holes in the valence band were present [68]. However, a maximum is observed at about $\sim 200^\circ\text{C}$ supporting the idea of a phase transition.

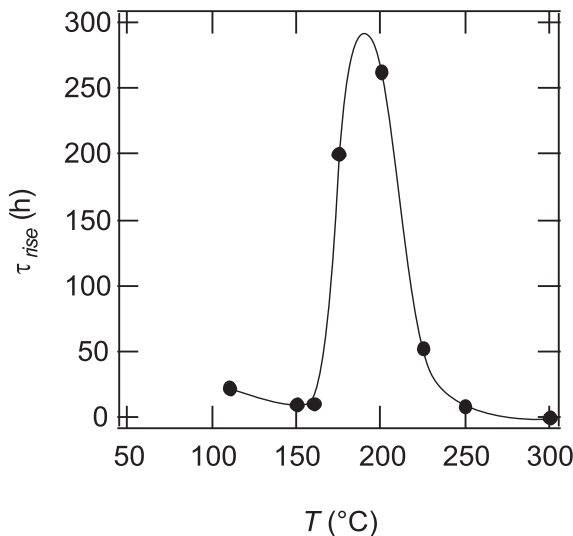


Figure 6.20: Temperature dependence of the time constant for the slow process under oxygen ($P_{\text{O}_2} = 10^5 \text{ Pa}$, $I = 1.4 \text{ W/cm}^2$). The solid line is drawn just to guide the eye.

6.3.4 Influence of light intensity

Photoconductivity measurements were carried out at light intensities from 0.05 W/cm^2 up to 1.4 W/cm^2 . With increasing light intensity more photons are absorbed and the number of excited electrons in the conduction band increases. Therefore, a continuous increase of the photoconductivity with light intensity is expected [68]. Since it is obvious from our measurements, that the photoconductivity shows a singularity at about 475 K (see above), we

6.3 Photoconductivity of TiO₂ single crystal

have studied the influence of light intensity above and below this temperature for comparison.

At lower temperatures (398 K) than 475 K the steady state photoconductance (G_0) increases continuously with light intensity (Figure 6.21). A change in the slope is observed at about 0.2 W/cm² indicating a different recombination mechanism. Similarly, the time needed to reach equilibrium (τ_{rise}) increases monotonically with the light intensity and also changes its slope at about 0.2 W/cm². In this temperature region no phase transition is expected, since both the light intensity and temperature are lower than in Figure 6.18.

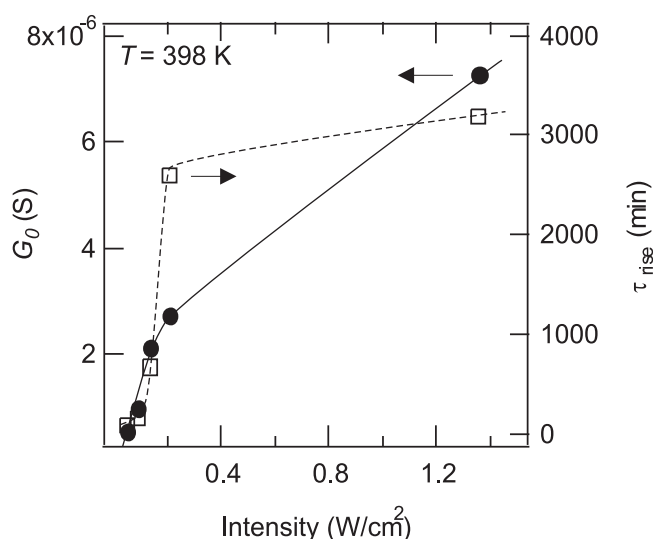


Figure 6.21: Steady state photoconductance (dark circles) and time constant of the rise curve (open squares) versus light intensity at 398 K ($P_{\text{O}_2} = 10^5$ Pa). The solid and dashed lines are drawn to guide the eye. At about 0.2 W/cm² both curves change their slopes, which indicates a different recombination mechanism.

At higher temperatures than 475 K, for example at 573 K, the steady state photoconductance shows a maximum at about 0.4 W/cm² (Figure 6.22). This maximum can be easily explained if the formation of defects (oxygen vacancies) with light absorption (see Equation (6.7)) is assumed. The concentration of defects increases with light intensity until a given threshold value (at 0.4 W/cm²). If the light intensity is increased further, the defects begin

6.3 Photoconductivity of TiO₂ single crystal

to interact with each other and form a reduced phase. The recombination processes are much faster in this new phase and the steady state photoconductivity decreases. The time needed to reach equilibrium (τ_{rise}) shows a similar dependence as the steady state photoconductance (Figure 6.22).

The maximum found in this temperature region for both the steady state photoconductivity and time constant is in accordance with a photoinduced phase transition near the surface region.

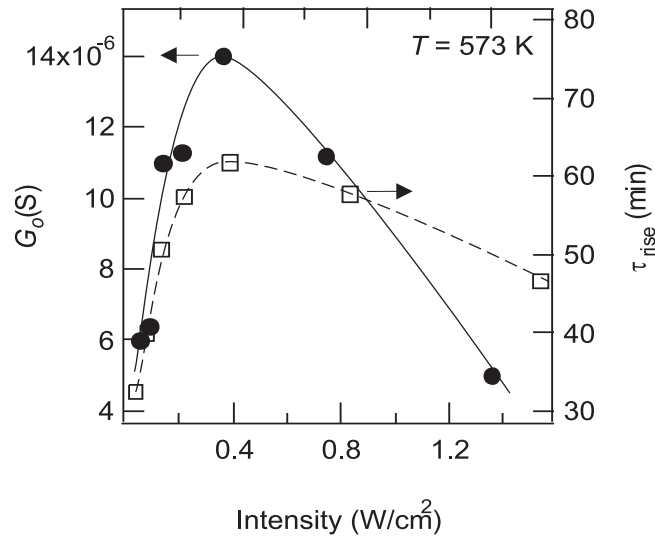


Figure 6.22: Steady state photoconductance (dark circles) and time constant of the rise curve (open squares) versus light intensity at 573 K. The solid and dashed lines are drawn to guide the eye. The maximum at 0.4 W/cm² under oxygen ($P_{\text{O}_2} = 10^5$ Pa) corresponds to a photoinduced phase transition.

Chapter 7

Discussion

7.1 Influence of milling time in micro- and nanocrystalline TiO₂

Different mechanisms govern the conduction processes in titanium dioxide depending on its modification and milling time. We have found the following mechanisms for the unmilled samples in a temperature range from 673 K up to 973 K and oxygen partial pressures between 10² Pa and 10⁵ Pa:

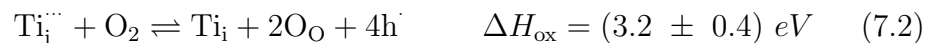
- **Microcrystalline rutile:**

n-type conductivity



- **Microcrystalline anatase:**

p-type conductivity



- **Nanocrystalline anatase:**

Ionic conductivity

With increasing milling time the average crystallite size decreases and the volume fraction of grain boundaries increases. Furthermore, the structure of the grains may also change. XPS and EPR measurements show the formation

7.1 Influence of milling time in micro- and nanocrystalline TiO_2

of defects during milling (Ti^{3+} ions). As already mentioned in Section 4.1 the milling process induces a phase transition in microcrystalline anatase. Correspondingly, the milled nanocrystalline anatase sample present a singularity after about 30 min of milling which may be related to the phase transformation detected by x-ray diffraction in milled microcrystalline anatase. The grain boundaries act as blocking paths in microcrystalline rutile. Hence, the milling process results in a decrease of the conductivity.

It is difficult to obtain information about the properties of the bulk and the grain boundaries from the impedance plots since the two semicircles have similar relaxation frequencies which leads to overlapping semicircles. However, it was possible to model the data of the unmilled and for one hour milled microcrystalline anatase samples with an equivalent circuit. From the models, the conductivities and activation energies of the conduction process in the bulk region and at the grain boundaries can be differentiated.

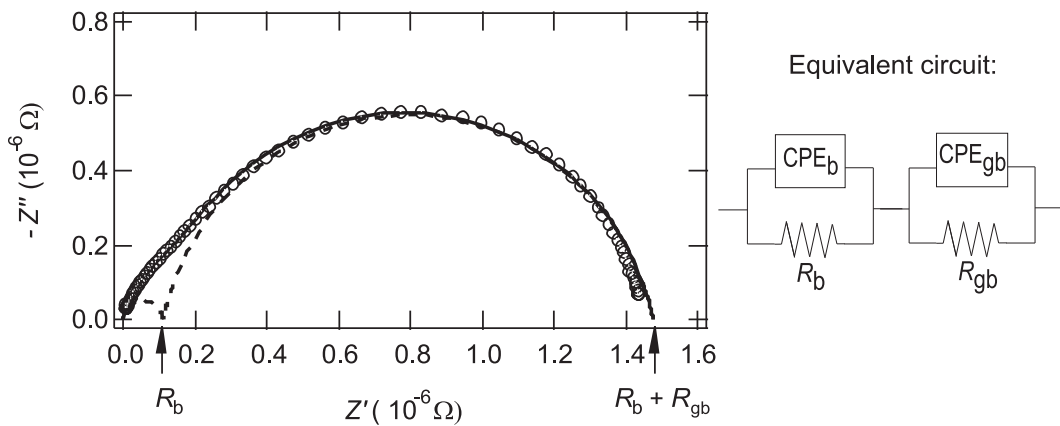


Figure 7.1: Complex plane representation of the impedance of the microcrystalline sample milled for 1 hour. Data were measured at 828 K and under 10^5 Pa of oxygen. The open circles correspond to the measured data. The solid line is the calculated response of the equivalent circuit shown on the right hand side of the figure. The dashed line is calculated considering the response of the bulk and the grain boundaries separately.

Figure 7.1 shows the complex plane representation of the impedance of the one hour milled microcrystalline anatase sample measured at 828 K under 10^5 Pa of oxygen. The calculated response of the equivalent circuit is shown with a solid line. The equivalent circuit was found using a fitting program

7.1 Influence of milling time in micro- and nanocrystalline TiO₂

written in turbo pascal [108]. The contribution of the grain boundaries and of the bulk are described each with a constant phase element (CPE) in parallel with a resistance. The overall response is given by these two contributions in series. Each of the two semicircles drawn by a dashed line are obtained by calculating the response of the grain boundaries or the bulk alone. The small semicircle corresponds to the bulk but, although $R_b < R_{gb}$, this does not imply that $\sigma'_b > \sigma'_{gb}$ (see Section 2.3.2).

Similar fits were found under other conditions. The activation energy at the grain boundaries and in the grain interiors calculated from the Arrhenius plots (Figure 7.2) are listed in Table 7.1.

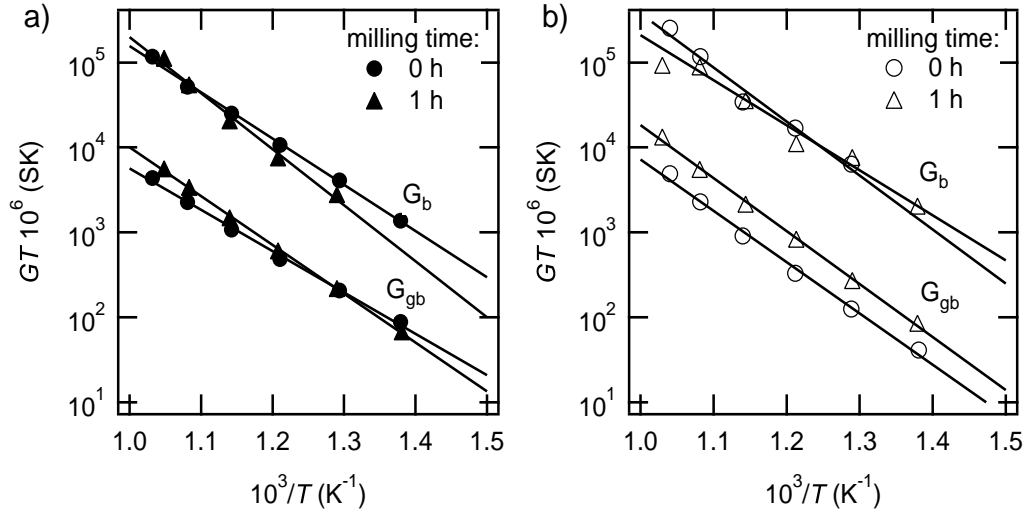


Figure 7.2: Arrhenius representation of the conductance of the grain boundaries (G_{gb}) and of the bulk (G_b) calculated from the fitting process for the unmilled sample and for the sample milled for one hour of microcrystalline anatase under oxygen ($P_{O_2} = 10^5$ Pa) (a) and under vacuum ($P_{O_2} = 10^2$ Pa) (b).

Due to the highly defective structure of the grain boundaries, it is reasonable to assume a higher contribution of ionic conductivity in this region. Similar values are found in the literature for activation energies at the grain boundaries of other ceramic materials such as ZrO₂:Y₂O₃ [59].

A p-type conductivity was assumed for the unmilled sample, which corresponds to literature values [21]. However, the activation energies of this

7.1 Influence of milling time in micro- and nanocrystalline TiO₂

Table 7.1: Activation energies in the bulk ($E_{A,b}$), at the grain boundary region ($E_{A,gb}$) and overall activation energy (E_A) of the unmilled sample and the sample milled for one hour of microcrystalline anatase under oxygen atmosphere ($P_{O_2} = 10^5$ Pa) and vacuum ($P_{O_2} = 10^2$ Pa).

Sample	$E_{A,b}$ (eV)	$E_{A,gb}$ (eV)	E_A (eV)
^a unmilled	0.96 ± 0.02	1.08 ± 0.02	0.95 ± 0.01
^a 1 h milled	1.31 ± 0.07	1.14 ± 0.02	1.03 ± 0.01
^b unmilled	1.3 ± 0.1	1.19 ± 0.04	1.02 ± 0.05
^b 1 h milled	1.05 ± 0.09	1.24 ± 0.02	1.09 ± 0.02

$${}^a P_{O_2} = 10^5 \text{ Pa}, {}^b P_{O_2} = 10^2 \text{ Pa}$$

sample are influenced by the oxygen partial pressure. Therefore, one may conclude that another mechanism contributes to the conduction process in the bulk at low oxygen partial pressures. Since the apparent activation energy for the unmilled sample under vacuum is 1.3 eV, one may conclude that reduction as described by Equation (6.4) takes place in the bulk (near the surface of the grains). The same activation energy is found for grain interiors of the one hour milled sample under oxygen. Hence, one may conclude that after one hour of milling the bulk can be reduced even under oxygen atmosphere. The sample milled for one hour under vacuum has an activation energy of about 1 eV in the bulk region which may be related to defects formed during milling near the surface of the grains where ionic conductivity dominates. XRD measurements show the formation of a high pressure phase of TiO₂ during milling, *i.e.*, TiO₂-II with α -PbO₂ structure. This result was observed by other authors [89] and they proved that the new phase is formed near the surface of the grains. Hence, the activation energy in the bulk region of the one hour milled sample may be affected by the formation of this phase.

The activation energies of the unmilled sample under $P_{O_2} = 10^5$ Pa are quite similar, suggesting that a partial blocking model is appropriate [59] (see Section 2.3.2). The other cases show different activation energies for the grain interior and the grain boundaries which is expected for the brick layer model without easy paths (see Section 2.3.2).

7.2 Influence of illumination in TiO₂ single crystal

UV-light absorption of TiO₂ single crystal has great influence on the structure of the material near the surface region. The changes induced in the solid during this process could be investigated by measuring the photoconductivity of a TiO₂ single crystal in a temperature range from 298 K up to 573 K and under oxygen and nitrogen atmospheres.

The measurements indicate the loss of lattice oxygen during illumination and the conduction mechanism is in agreement with Equation (6.4) (n-type conductivity). A phase transition of the first order is found at about 475 K (see Figure 6.18). A similar curve is found for the temperature dependence of the heat capacity of a two-dimensional lattice of spins calculated with the Ising model [109]. In that case, the curve shows a transition between ferromagnetic and paramagnetic behavior at the Curie temperature [61].

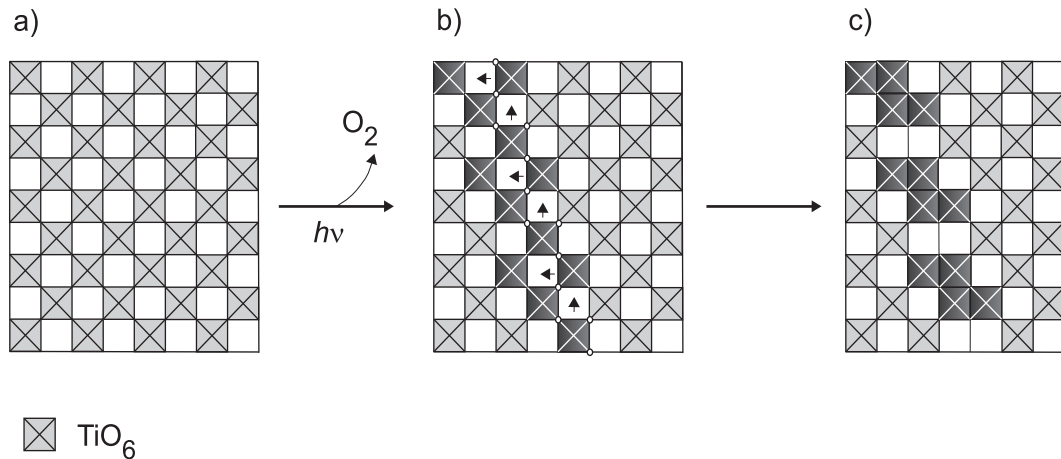


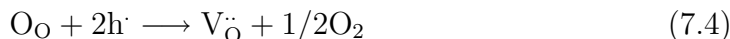
Figure 7.3: Schematic representation of a phase transition under illumination. Ideal titanium dioxide surface with arrays of TiO₆ octahedra (grey squares)(a). Formation of oxygen vacancies upon illumination (b), the dark squares indicate the octahedra with or near missing oxygens. Association of defects to form crystallographic shear planes (CSP) (c).

Conductivity measurements indicate a phase transition at about 475 K. A schematic representation of the process taking place above this temperature is shown in Figure 7.3. Consider the surface of an ideal TiO₂ single crystal (a).

7.3 Comparison with catalytic activity

UV-light absorption favors the release of lattice oxygen from the surface (b). At $T > 475$ K the non-stoichiometry is accommodated by the system forming extended planar defects known as crystallographic shear planes (CSP) (c).

The formation of oxygen vacancies upon absorption of UV light on titanium dioxide has already been reported [110] to explain the observed photoinduced hydrophilicity. The photogenerated electron-hole pairs are assumed to reduce and oxidize the TiO_2 surface itself, converting Ti^{4+} into Ti^{3+} sites, and creating oxygen vacancies as follows:



Surface science studies have also pointed out the creation of Ti^{3+} surface defects by the absorption of UV photons [111] on TiO_2 . Similarly, other methods such as Ar^+ ion bombardment and electron beam exposure can as well generate surface defects [112, 113]. Other oxides like SrTiO_3 also show surface structural changes upon ion bombardment with Ar^+ [114]. In all cases the defects disappear upon exposure to oxygen atmosphere.

These measurements are done under ultrahigh vacuum (UHV) conditions and therefore, provide information about the system in a pressure range away from the one used in practical catalysis. However, these experiments indicate that the surface reduction and oxidation of titanium dioxide upon illumination with UV light are possible events.

7.3 Comparison with catalytic activity

The conductivity measurements described above can be compared with measurements done at the Institut für Technische Chemie (University of Hannover) on the catalytic activity of titanium dioxide [35]. Several correlations are found between the two kinds of measurements which provide a deeper understanding of the catalytic processes.

The quantum yield (see Section 2.7) for the total oxidation of propane with milled microcrystalline rutile and anatase shows a maximum after about 30 minutes of milling (Figure 7.4a and 7.4b, respectively). This result can neither be explained in terms of adsorption processes nor in terms of coke deposit on the surface of the catalyst. The maximum may be related, on

7.3 Comparison with catalytic activity

the one hand, to the new phase detected in milled microcrystalline anatase by XRD and, on the other hand, to the different conduction mechanism found for microcrystalline rutile milled for 30 minutes by means of impedance spectroscopy (conductivity measurements).

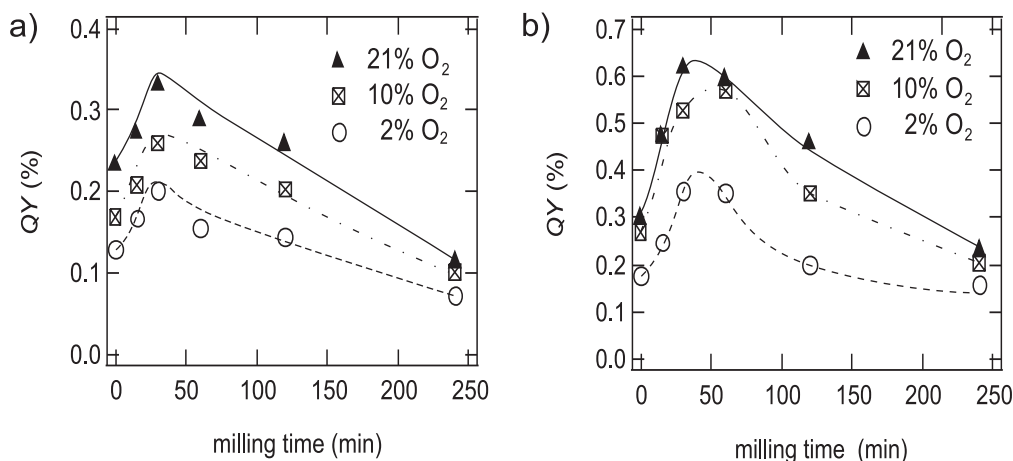


Figure 7.4: Quantum yield for the total oxidation of propane on microcrystalline rutile (a) and anatase (b) at 433 K and for different milling times and oxygen concentrations. Nitrogen was used as a carrier gas and the concentration of propane was 300 ppm [35]. The solid and dashed lines are drawn to guide the eye.

The milled nanocrystalline anatase also presents a maximum of the quantum yield for the total oxidation of propene after about 30 minutes of milling (Figure 7.5). This result correlates with the maximum found in the conductivity of this sample (see Figure 6.12).

After short milling times (below about 30 minutes) the surface area (of the microcrystalline samples) and the number of defects near the surface of the grains increases. For longer milling times than about 30 minutes the surface area is continuously increasing (for the microcrystalline samples) and the defects form a new structure at the surface of the grains which leads to a decrease in the catalytic activity and variations in the conduction processes.

Furthermore, the temperature dependence of the photocatalytic activity shows a maximum at about 475 K (Figure 7.6). Usually, this experimental result is explained by assuming that the observed temperature dependence of the quantum yield is caused by adsorption processes (see, *e.g.*, [2]). How-

7.3 Comparison with catalytic activity

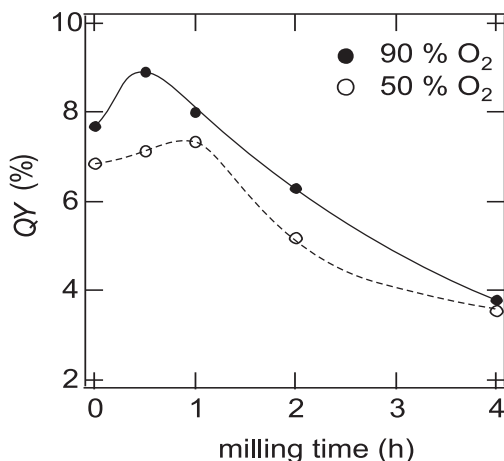


Figure 7.5: Quantum yield of milled nanocrystalline anatase for the total oxidation of propene versus milling time [93]. The solid and dashed lines are drawn to guide the eye.

ever, this assumption is not satisfactory since the catalyst becomes colored at higher temperatures. Under mild oxidation conditions it turns white again, hence, this discoloration cannot be attributed to a coke deposit as assumed by some authors (see, *e.g.*, [115–118]). This result, again, corresponds to the measurements done on the photoconductivity of titanium dioxide (Figure 6.18), confirming the hypothesis of a change in the surface structure of the catalyst.

It is obvious from these results that the defect structure of the material greatly affects its catalytic activity. The energy absorbed by the material during milling or under illumination leads to a modified structure of the catalyst near the surface region where the oxygen ions have a higher mobility due to the formation of defects. These defects collapse at a given threshold concentration which is achieved either after about 30 minutes of milling or at 475 K under illumination with UV light.

Therefore, during the photocatalytic processes the catalyst is reduced due to the absorption of UV light and the presence of hydrocarbons, and re-oxidized by the oxygen present in the atmosphere. The mechanism resembles the one proposed by Mars and van Krevelen (see Section 2.7), but instead of being thermally activated, the catalyst is activated by the absorption of UV light.

7.3 Comparison with catalytic activity

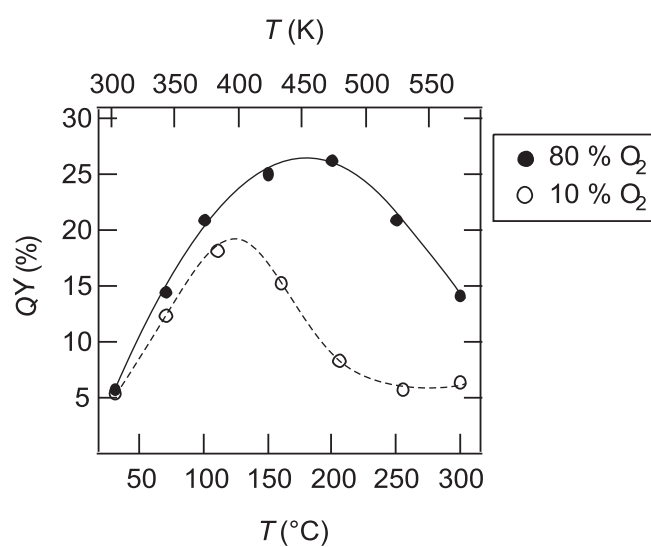


Figure 7.6: Temperature dependence of the quantum yield of microcrystalline titanium dioxide (anatase) for the total oxidation of propene under different oxygen partial pressures [119,120]. The solid and the dashed lines are drawn to guide the eye.

Chapter 8

Conclusion and outlook

In this work the effect of high-energy ball milling (HEBM) on the conductivity of titanium dioxide (rutile and anatase) has been studied. Besides, the variations of the conductivity of TiO_2 under UV-light absorption (photoconductivity) have been investigated. The results have been correlated with catalytic measurements and provide new insights into the processes taking place during photocatalytic reactions.

Conductivity measurements have been proved to be a useful method for characterizing the material under catalytic conditions. However, other characterization techniques such as, for instance, XRD, XPS or EPR may be very useful in providing complementary information about the system, and in confirming assumptions derived from other measurements. In the present case, these methods have been helpful in confirming the appearance of Ti^{3+} ions and the formation of a new phase while milling.

It can be concluded from the results that the mobility of the lattice oxygen ions near the surface region has a great influence on the catalytic activity of the material [120]. Therefore, the catalyst is much more involved in the catalytic processes than thought before. In the case of the total oxidation of propene or propane in the gas phase, the reaction mechanism can be explained neither in terms of adsorption of educt species and desorption of products nor by a Mars-van Krevelen mechanism. From the results of this work one can conclude that the lattice oxygen is activated by the absorption of UV light. After that, the catalyst is easily reduced by the educt species present in the gas phase and re-oxidized by the oxygen in the atmosphere. If the catalyst is too strongly reduced, a phase transition takes place near the

surface which leads to a decrease in the catalytic activity. This may happen, for example, under high UV-light intensities, at elevated temperatures or in an atmosphere with low oxygen content.

Another parameter that should be studied is the wavelength of the light source in photoconductivity measurements. This can be realized by using band pass filters between the light source and the photoconductivity cell. Further information could be obtained from these measurements and comparison with measurements on the catalytic activity at different wavelengths about the properties of the catalyst.

In addition, photoconductivity measurements should be done under reaction conditions, *i.e.*, under an atmosphere with some hydrocarbon and the corresponding concentration of oxygen. If possible, the catalytic activity should be measured at the same time, in order to minimize differences between the samples and measurement conditions.

The measurements done on TiO_2 should be repeated for other catalysts such as, *e.g.*, SnO_2 which has the same crystal structure as titanium dioxide but a considerably lower catalytic activity. Comparisons between results from different catalyst materials should help in understanding their properties.

Appendix A

Measurement bridge

The principle of the completely automatic measurement bridge is represented in Figure A.1 [99].

A sinus generator applies a vector potential \vec{e}_s with a frequency f_s through the sample. The modulator makes sure that the potential applied to R_r has exactly the same frequency. When the current i_d flowing through the null detector is null, at the point S one has (by Kirchhoff's law):

$$i_x = -i_r \Leftrightarrow \frac{\vec{e}_s}{Z_x} = \frac{\vec{e}_r}{R_r} \quad (\text{A.1})$$

If R_r is known, one can calculate Z_x from the vector relation between the two voltages \vec{e}_s and \vec{e}_r :

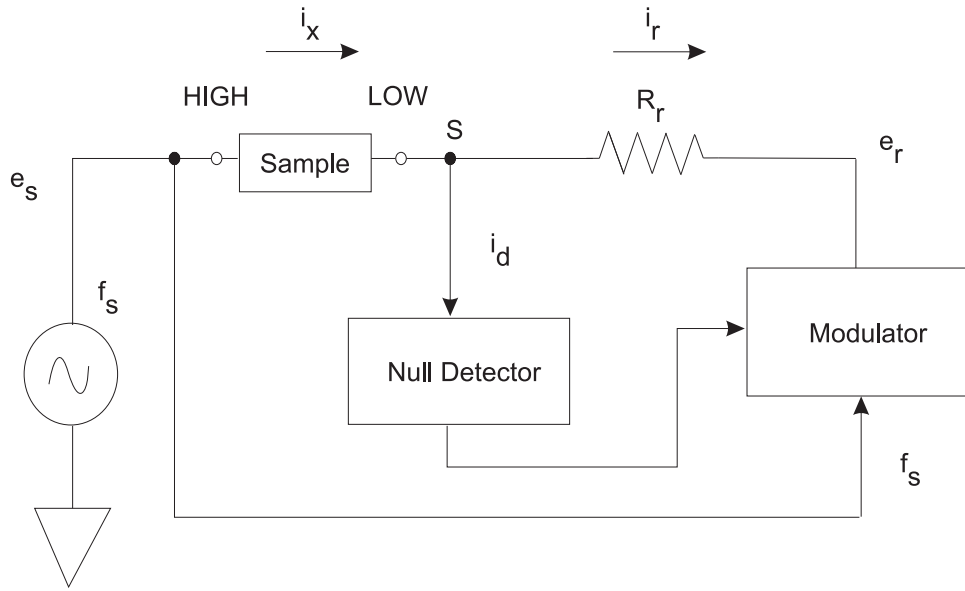
$$Z_x = R_r \cdot \frac{\vec{e}_s}{\vec{e}_r} \quad (\text{A.2})$$

A not balanced current, i_d , controls by a regeneration the amplitude and phase of the test signal \vec{e}_s so that the balanced voltage \vec{e}_r is generated.

In order to measure the impedance one needs to know the vector voltages \vec{e}_s and \vec{e}_r . The detection takes place in the VRD part (vector voltage ration detector) (see Figure A.2) of the measurement bridge.

The VRD has three steps:

- In the process amplifier a signal is selected (\vec{e}_s or \vec{e}_r) and amplified.
- In the phase detector the signals \vec{e}_s and \vec{e}_r are decomposed in their real and imaginary parts.



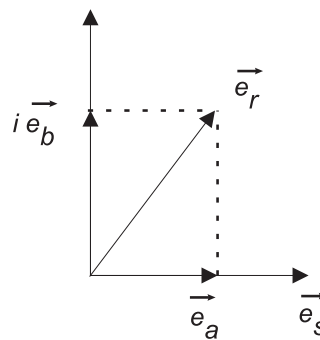
Test Signal Source

Figure A.1: Principle of the measurement bridge.

- In the A-D converter the two components are transformed to a time-domain signal.

The vectors \vec{e}_s and \vec{e}_r are decomposed in its orthogonal components each in relation to the other signal.

$$\vec{e}_r = \vec{e}_a + i\vec{e}_b \quad (\text{A.3})$$



\vec{e}_a and \vec{e}_b are the vector components of \vec{e}_r , which are in phase or 90° displaced from \vec{e}_s .

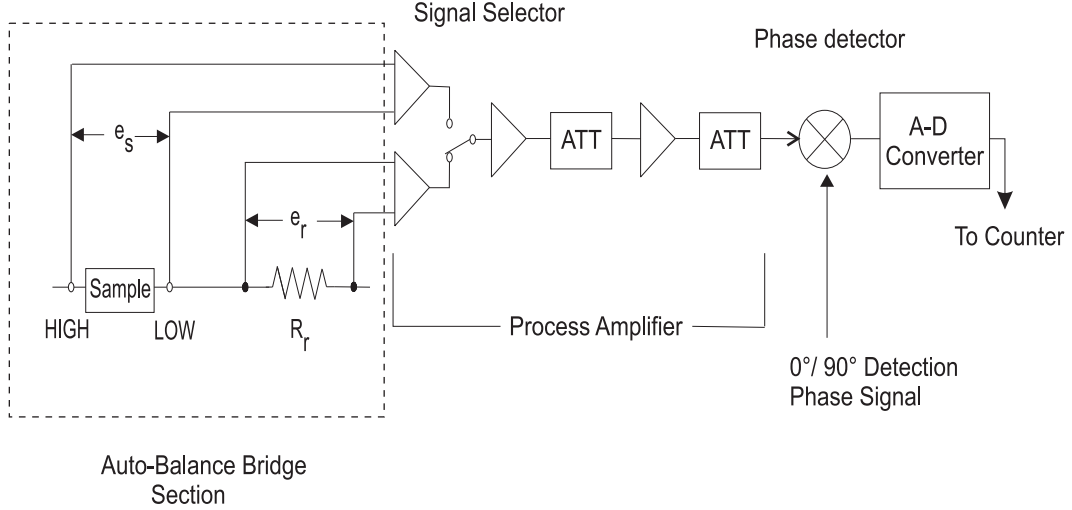


Figure A.2: Vector voltage ratio detector.

To determine the magnitude of the vector components the A-D converter transforms the vector voltages in time periods.

From the four components of the two voltage signals \vec{e}_s and \vec{e}_r one can calculate the real and the imaginary parts of the cell impedance:

$$R = R_r \cdot \frac{\vec{e}_a \cdot \vec{e}_c + \vec{e}_b \cdot \vec{e}_d}{\vec{e}_a^2 + \vec{e}_b^2} \quad (\text{A.4})$$

$$X = R_r \cdot \frac{\vec{e}_a \cdot \vec{e}_d - \vec{e}_b \cdot \vec{e}_c}{\vec{e}_a^2 + \vec{e}_b^2} \quad (\text{A.5})$$

By the R/X and G/B measurements at high ω the signal transmission in the amplifier and the wires in relation to the phase have a non-negligible phase displacement, so that there might be an error in the vector components detection. For this reason the device measures up to 13 MHz.

One can detect with HP 4192 A also the amplitude and phase relation of the voltages \vec{e}_s and \vec{e}_r . For this, the device has two independent voltmeters with separated entrances. It is advantageous to separate the contacts of the two voltmeters section in the cell. That is why a four polar cell is used.

Appendix B

Conductivity of $\text{Ta}_x\text{Ti}_{(1-x)}\text{X}_2$, $\text{X} = \text{S}, \text{Se}$

Introduction

The dc conductivity of transition metal dichalcogenides $\text{Ta}_x\text{Ti}_{(1-x)}\text{S}_2$ and $\text{Ta}_x\text{Ti}_{(1-x)}\text{Se}_2$ was studied at room temperature.

The layered structure of transition metal dichalcogenides is schematically represented in Figure B.1. The host layers are held together by relatively weak forces [121] and the gap between them is called van der Waals gap.

Depending on their coordination the host materials present two types of TX_2 sandwiches (T: transition metal, X: Se, S):

- octahedral coordination of the transition metal atom by the chalcogens.
- trigonal prismatic coordination of the transition metal atom by the chalcogens.

These structures, either with octahedral or with trigonal prismatic coordination, may present different polytypes such as, *e.g.*, 4H_b , 2H or 1T . This kind of nomenclature gives information about:

1. The number of sandwiches required to obtain a unit cell perpendicular to the plane of the layers.
2. The overall symmetry: Trigonal (T), Hexagonal (H) or Rhombohedral (R).

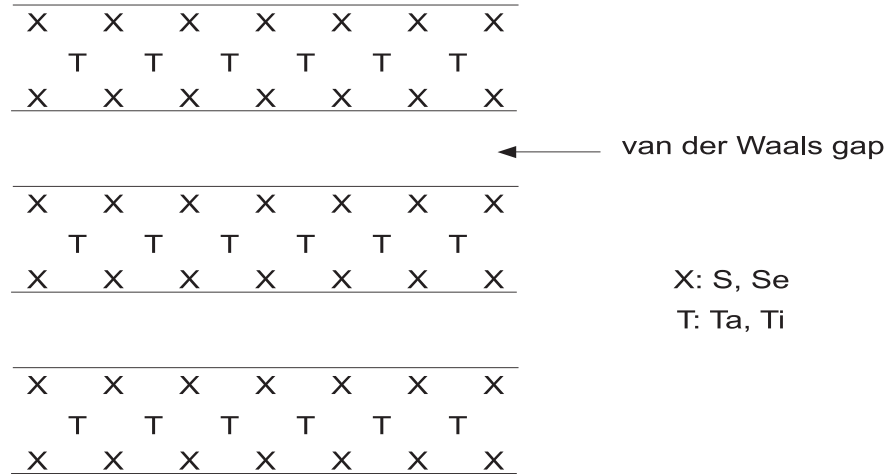


Figure B.1: Schematic representation of the transition metal dichalcogenides layers presenting a sandwich structure.

3. Subscripts are sometimes required to distinguish polytypes (a, b).

Intercalation of tantalum between layers of dichalcogenides TiS_2 and TiSe_2 originates changes in the crystalline structure of the material and in its electronic properties [121] which can be studied by measuring the electrical conductivity.

TiS_2 and TiSe_2

Metals of the Group IV show 1T structure with octahedral coordination of the metal by the chalcogens. This coordination results in the field splitting of the d orbitals. The valence band has chalcogen p character.

When a small amount of excess metal is present TiS_2 presents a small band gap and is a semiconductor. There is no overlap between the upper part of the p valence band and the lower part of the d conduction band in TiSe_2 , which would lead to semimetallic properties. Below 202 K TiSe_2 shows a structural distortion which leads to p-d hybridization. Because of this, electrons and holes are removed and the conductivity decreases.

TaS₂ and TaSe₂

Metals of the group V form polytypes with both octahedral and trigonal prismatic coordination.

1T-TaS₂ and 1T-TaSe₂ (octahedral structures) have a d¹ configuration with a half filled d band, and should show metallic properties. However, the properties are very sensitive to distortions in the structure of the Fermi surface and these materials have lower conductivities than metals even at room temperature.

TaS₂ and TaSe₂ also form 2H-polytypes with trigonal prismatic coordination. The energy difference between 1T- and 2H-polytypes is very small. The Fermi surface of the 1T-polytypes has electron-like character, while the one of 2H-polytypes has a hole-like character. In general the 2H-structures show better metallic properties.

Experimental

The Ta_xTi_(1-x)S₂ and Ta_xTi_(1-x)Se₂ powders were ground in a mortar. In order to measure the conductivity the samples have to be contacted. The contacts were made by pressing platinum powder (Merck, 99.95%) on the samples. For this purpose the same procedure as the one described for the polycrystalline titanium dioxide samples was followed (see Section 3.3).

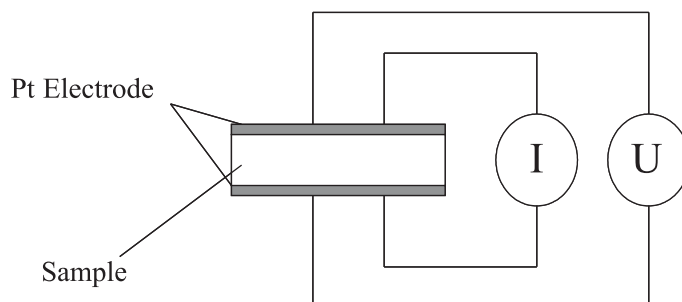


Figure B.2: 4 point configuration for measurements of dc conductivity.

Some measurements were done using the impedance analyzer described in Chapter 5. However, due to the high conductivity of the samples only those with small amount of intercalated tantalum could be measured. The conductivity of the samples with a high amount of intercalated tantalum could not

be measured because of stray capacitances. Since these stray capacitances have only small influence on dc conductivity measurements, the dc conductivity of the samples was determined using this method. With this kind of measurement it has been proved that even by 80% tantalum the samples are not yet metallic but semiconductive.

The dc conductivity of the samples was determined at room temperature by means of a 4 point configuration (Figure B.2). A current I of 1 A was applied to the sample and the voltage U between the electrodes was measured. Using Ohm's law (Equation (B.1)) the conductance G and, through the sample geometry, the conductivity σ of the sample was calculated.

$$G = I/U \tag{B.1}$$

$$\sigma = Gl/A, \tag{B.2}$$

where l is the thickness and A the area of the sample.

Results

The electrical conductivity σ of $\text{Ta}_x\text{Ti}_{(1-x)}\text{S}_2$ and $\text{Ta}_x\text{Ti}_{(1-x)}\text{Se}_2$ is plotted vs. x on a semilogarithmic scale (Figure B.3a) and on a double logarithmic scale (Figure B.3b). These results show that already by small amounts of tantalum (0.25%) the electrical conductivity increases steeply.

After this fast rise the conductivity remains at about 1000 S/m up to $x \simeq 30\%$, for the compound with sulfur. This is followed by a second fast increase of the conductivity up to about 1600 S/m.

The compound with selenium shows a more complicated behavior: after the first increase the conductivity decreases down to about 300 S/m. Afterwards it increases up to 1000 S/m at $x \simeq 50\%$ and decreases again down to 300 S/m at $x \simeq 80\%$.

Discussion

During the intercalation process electrons are transferred from the intercalant species to the host layer [121]. Therefore, the conductivity should increase monotonically with the amount of tantalum. However, the results show more complicated dependencies of the conductivity with x .

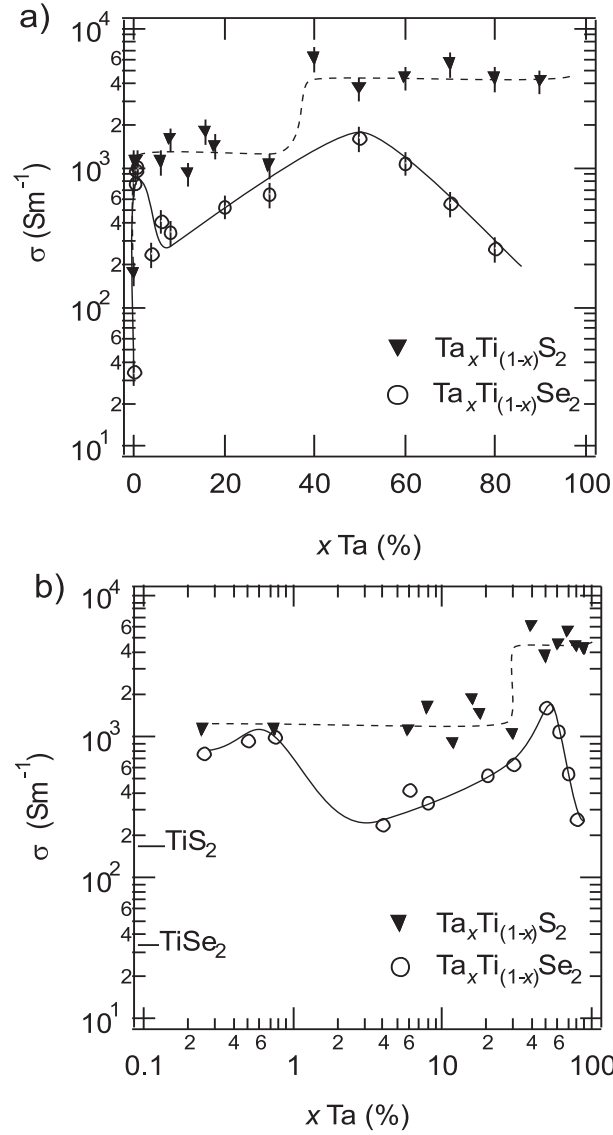


Figure B.3: Electric conductivity of $\text{Ta}_x\text{Ti}_{(1-x)}\text{S}_2$ (dark triangles) and $\text{Ta}_x\text{Ti}_{(1-x)}\text{Se}_2$ (open circles) vs. x in a semilogarithmic plot (a) and in a double logarithmic plot (b) at 298 K and under air. The solid and dashed lines are drawn to guide the eye.

An explanation for this behavior may be found in the structural distortions which are related to the structure of the Fermi surfaces.

TiS₂ crystallizes in the 1T phase and TaS₂ in the 2H modification [122]. In the case of Ta_xTi_(1-x)S₂ one can explain the steep conductivity increase at $x = 0.4$ as a phase transition from octahedral to trigonal prismatic coordination.

Since metals have an electrical conductivity bigger than 10⁶ S/m, one can conclude that these compounds are, at least up to 80% tantalum for Ta_xTi_(1-x)Se₂ and up to 90% tantalum for Ta_xTi_(1-x)S₂, not metallic but semiconductive.

Appendix C

List of publications and conferences

Conferences

Posters

- *Herstellung und Charakterisierung von nanokristallinem TiO₂ für die Photokatalyse*
S. Indris, R. Amade, P. Heitjans, A. Haeger and D. Hesse
Vortragstagung der GDCh-Fachgruppe Festkörperchemie und Materialforschung
Dresden, 24. – 26. September 2002.
Z. Anorg. Allg. Chem. **628**, 2221 (2002)
- *Einfluss von Kugelmahlen auf die Quantenausbeute photokatalysierter Gasphasenreaktionen*
M. Finger, A. Haeger, D. Hesse, S. Indris, R. Amade and P. Heitjans
DECHEMA/ GVC Jahrestagungen
Mannheim, 16. – 18. September 2003.
Chemie Ingenieur Technik **75**, 1043 (2003).
- *Photoconductivity measurements on titanium dioxide single crystal*
R. Amade, P. Heitjans, D. Hesse, A. Haeger and M. Finger
69. Jahrestagung der Deutschen Physikalischen Gesellschaft (DPG)
Berlin, 4. – 9. March 2005.

Presentations

- *Photoconductivity at the surface of TiO₂ single crystal*
R. Amade, P. Heitjans, S. Indris, M. Finger, A. Haeger and D. Hesse
Solid State Ionics: Cross Frontier Problems in Physical Chemistry and
Materials Science
Giessen, 15. – 16. July 2005.

Publications

- *Preparation, Characterization and Catalytic Properties of Nanocrystalline TiO₂*
S. Indris, R. Amade, P. Heitjans, M. Finger, A. Haeger, D. Hesse,
W. Grünert, A. Börger and K. D. Becker
J. Phys. Chem. B, **109**, 23274-23278, (2005).
- *Influence of gas atmosphere and temperature on the conductivity and the photoconductivity of TiO₂ single crystal in the surface region*
R. Amade, P. Heitjans, S. Indris, M. Finger, A. Haeger and D. Hesse
Phys. Chem. Chem. Phys., **8**, 777-782, (2006).

Bibliography

- [1] A. L. Linsebigler, G. Lu, and J. T. Yates, Jr., *Chem. Rev.* **95**, 735 (1995).
- [2] J.-M. Herrmann, *Top. Cat.* **34**, 49 (2005).
- [3] J.-M. Herrmann, *Helv. Chim. Act.* **84**, 2731 (2001).
- [4] M. R. Hoffmann, S. T. Martin, W. Choi, and D. W. Bahnemann, *Chem. Rev.* **95**, 69 (1995).
- [5] A. Hagfeldt and M. Grätzel, *Chem. Rev.* **95-68**, 49 (1995).
- [6] N. Golego, S. A. Studenikin, and M. Cocivera, *J. Electrochem. Soc.* **147**, 1592 (2000).
- [7] R. M. Geatches, A. V. Chadwick, and J. D. Wright, *Sens. Act. B* **4**, 467 (1991).
- [8] G. Grubert, M. Stockenhuber, O. P. Tkachenko, and M. Wark, *Chem. Mater.* **14**, 2458 (2002).
- [9] K. Hoshino, N. L. Peterson, and C. L. Wiley, *J. Phys. Chem. Solids* **46**, 1397 (1985).
- [10] P. Kofstad, *J. Phys. Chem. Solids* **23**, 1579 (1962).
- [11] R. N. Blumenthal, J. Coburn, J. Baukus, and W. M. Hirthe, *J. Phys. Chem. Solids* **27**, 643 (1966).
- [12] R. N. Blumenthal, J. Baukus, and W. M. Hirthe, *J. Electrochem. Soc.: Solid State Science* **114**, 172 (1967).

BIBLIOGRAPHY

- [13] F. Millot et al., *Prog. Solid St. Chem.* **17**, 263 (1987).
- [14] T. Bak, J. Nowotny, M. Rekas, and C. C. Sorrell, *J. Phys. Chem. Solids* **64**, 1043 (2003).
- [15] T. Bak, J. Nowotny, M. Rekas, and C. C. Sorrell, *J. Phys. Chem. Solids* **64**, 1057 (2003).
- [16] T. Bak, J. Nowotny, M. Rekas, and C. C. Sorrell, *J. Phys. Chem. Solids* **64**, 1069 (2003).
- [17] D. K. Moore, D. J. Cherniak, and E. B. Watson, *Am. Miner.* **83**, 700 (1998).
- [18] D. Eder and R. Kramer, *Phys. Chem. Chem. Phys.* **5**, 1314 (2003).
- [19] J.-F. Marucco, J. Gautron, and P. Lemasson, *J. Phys. Chem. Solids* **42**, 363 (1981).
- [20] J. Nowotny et al., *Ceram. Int.* **24**, 571 (1998).
- [21] P. Knauth and H. L. Tuller, *J. App. Phys.* **85**, 897 (1999).
- [22] J. Nowotny, M. Radecka, and M. Rekas, *J. Phys. Chem. Solids* **58**, 927 (1997).
- [23] E. Iguchi and K. Yajima, *J. Phys. Soc. Jap.* **32**, 1415 (1972).
- [24] J. Yahia, *Phys. Rev.* **130**, 1711 (1963).
- [25] N. Ait-Yones, F. Millot, and P. Gerdanian, *Solid State Ionics* **12**, 431 (1984).
- [26] N. Ait-Yones, F. Millot, and P. Gerdanian, *Solid State Ionics* **12**, 437 (1984).
- [27] U. Balachandran and N. G. Eror, *J. Mat. Sci.* **23**, 2676 (1988).
- [28] W. Hotan, W. Göpel, and R. Haul, *Surf. Sci.* **83**, 162 (1979).
- [29] Y. W. Chung, W. J. Lo, and G. A. Somorjai, *Surf. Sci.* **64**, 588 (1977).
- [30] W. J. Lo, Y. W. Chung, and G. A. Somorjai, *Surf. Sci.* **71**, 199 (1978).

BIBLIOGRAPHY

- [31] G. W. Clark and L. L. Kesmodel, *Ultramicroscopy* **41**, 77 (1992).
- [32] P. Zschack, J. B. Cohen, and Y. W. Chung, *Surf. Sci.* **262**, 395 (1992).
- [33] M. A. Henderson, *Surf. Sci.* **419**, 174 (1999).
- [34] M. A. Henderson, W. S. Epling, C. L. Perkins, C. H. F. Peden, and U. Diebold, *J. Phys. Chem. B* **103**, 5328 (1999).
- [35] A. Haeger, PhD thesis, University of Hannover, in preparation.
- [36] M. Finger, A. Haeger, and D. Hesse, *Chem. Eng. Technol.* **28**, 1 (2005).
- [37] A. C. Fisher, L. M. Peter, E. A. Ponomarev, A. B. Walker, and K. G. U. Wijayantha, *J. Phys. Chem.* **104**, 949 (2000).
- [38] C. J. Barbé et al., *J. Am. Ceram. Soc.* **80**, 3157 (1997).
- [39] R. Kern, R. Sastrawan, J. Ferber, R. Stangl, and J. Luther, *Electrochim. Acta* **47**, 4213 (2002).
- [40] D. Cahen, G. Hodes, M. Grätzel, J. F. Guillemoles, and I. Riess, *J. Phys. Chem. B* **104**, 2053 (2000).
- [41] R. R. Addiss, Jr. and F. G. Wakim, *Phot. Sci. Eng.* **13**, 111 (1969).
- [42] H. Gleiter, *Adv. Mat.* **4**, 474 (1992).
- [43] W. Winterer, *Nanocrystalline Ceramics - Synthesis and Structure*, Springer - Verlag, Berlin, 2002.
- [44] R. W. Siegel, *Encyclopedia of Applied Physics*, volume 11, VCH, New York, 1994.
- [45] I. W. Chen and X. H. Wang, *Nature* **404**, 168 (2000).
- [46] J. Schoonman, *Solid State Ionics* **135**, 5 (2000).
- [47] W. Puin and P. Heitjans, *Nanostructured Materials* **6**, 885 (1995).
- [48] P. Heitjans and S. Indris, *J. Phys.: Condens. Matter* **15**, R1257 (2003).
- [49] H. L. Tuller, *J. Electroceram.* **1**, 211 (1997).

BIBLIOGRAPHY

- [50] W. Puin, S. Rodewald, R. Ramlau, P. Heitjans, and J. Maier, *Solid State Ionics* **131**, 159 (2000).
- [51] P. Mondal, A. Klein, W. Jaegermann, and H. Hahn, *Solid State Ionics* **118**, 331 (1999).
- [52] H. Gleiter, *Prog. Mat. Sci.* **33**, 223 (1989).
- [53] J. Ying and T. Sun, *J. Electroceram.* **1**, 219 (1997).
- [54] X. Liu et al., *Mat. Sci. Eng.* **A326**, 235 (2002).
- [55] H.-J. Fecht, *Nanostruct. Mat.* **6**, 33 (1995).
- [56] A. K. Jonscher, *Dielectric Relaxation in Solids*, Chelsea Dielectric Press, London, 1983.
- [57] G. B. Arfken and H. J. Weber, *Mathematical Methods for Physicists*, Harcourt/ Academic Press, San Diego, 1996.
- [58] A. K. Jonscher, *Universal Relaxation Law*, Chelsea Dielectric Press, London, 1996.
- [59] J. R. Macdonald (Ed.), *Impedance Spectroscopy - Emphasizing Solid Materials and Systems*, John Wiley Sons, New York, 1987.
- [60] I. M. Hodge, M. D. Ingram, and A. R. West, *J. Electroanal. Chem.* **74**, 125 (1976).
- [61] A. R. West, *Basic Solid State Chemistry*, John Wiley Sons, Chichester, 1987.
- [62] K. Funke, *Prog. Solid St. Chem.* **22**, 111 (1993).
- [63] J. E. Bauerle, *J. Phys. Chem. Solids* **30**, 2657 (1969).
- [64] W. D. Kingery, H. K. Bowen, and D. Uhlmann, *Introduction to Ceramics*, John Wiley Sons, New York, 1976.
- [65] M. Henzler and W. Göpel, *Oberflächenphysik des Festkörpers*, B. G. Teubner Studienbücher, Stuttgart, 1994.
- [66] A. K. Jonscher, *Phil. Mag. B* **38**, 587 (1978).

BIBLIOGRAPHY

- [67] K. L. Ngai, A. K. Jonscher, and C. T. White, *Nature* **277**, 185 (1979).
- [68] S. M. Rywkin, *Photoelektrische Erscheinungen in Halbleitern*, Akademie - Verlag, Berlin, 1965.
- [69] R. H. Bube, *Photoconductivity of Solids*, John Wiley Sons, New York, 1960.
- [70] C. N. Satterfield, *Heterogeneous Catalysis in Practice*, McGraw-Hell, New York, 1994.
- [71] J. M. Thomas and W. J. Thomas, *Principles and Practice of Heterogeneous Catalysis*, VCH Verlagsgesellschaft mbH, Weinheim, 1997.
- [72] M. Schiavello, editor, *Photoelectrochemistry, Photocatalysis and Photoreactors*, D. Reidel Publishing Company, 1985.
- [73] D. F. Ollis and H. Al-Ekabi, editors, *Photocatalytic Purification and Treatment of Water and Air*, Elsevier Science Publishers B. V., 1993.
- [74] M. Scheller, *Photokatalytische Oxidation von Alkenen und Alkanen mit Sauerstoff an belichtetem Titandioxid*, PhD thesis, University of Hannover, 2001.
- [75] A. Gajović, M. Stubičar, M. Ivanda, and K. Furić, *J. Molec. Struct.* **563-564**, 315 (2001).
- [76] J. Staun Olsen, L. Gerward, and J. Z. Jiang, *High Pressure Research* **22**, 385 (2002).
- [77] S. Andersson, B. Collén, U. Kuylenstierna, and A. Magnéli, *Act. Chim. Scand.* **11**, 1641 (1957).
- [78] R. F. Bartholomew and D. R. Frankl, *Phys. Rev.* **187**, 829 (1966).
- [79] P. G. Wahlbeck and P. W. Gilles, *J. Am. Cer. Soc.* **49**, 181 (1966).
- [80] M. A. Barteau, *Chem. Rev.* **96**, 1413 (1996).
- [81] A. F. Hollemann and E. Wiberg, *Lehrbuch der Anorganischen Chemie*, Walter de Gruyter, Berlin, 1985.
- [82] S. Indris, D. Bork, and P. Heitjans, *J. Mat. Synth. Proc.* **8**, 245 (2000).

BIBLIOGRAPHY

- [83] H. P. Klug and L. E. Alexander, *X - Ray Diffraction Procedures*, Wiley, New York, 1959.
- [84] H. Neff, *Grundlagen und Anwendung der Röntgen-Feinstruktur-Analyse*, R. Oldenbourg, München, 1962.
- [85] B. E. Warren, *X-ray Diffraction*, Dover Publications, New York, 1969.
- [86] K. Sugiyama and Y. Takeuchi, *Zeit. Krist.* **194**, 305 (1991).
- [87] E. Sanchez et al., *J. Sol. Sta. Chem.* **122**, 309 (1996).
- [88] S. Bégin-Colin, T. Giroto, G. Le Caër, and A. Mocellin, *J. Sol. Sta. Chem.* **149**, 41 (2000).
- [89] T. Giroto, S. Bégin Colin, X. Devaux, G. Le Caër, and A. Mocellin, *J. Mat. Synth. Proc.* **8**, 139 (2000).
- [90] Y. L. Chen, M. Zhu, M. Qi, D. Z. Yang, and H. J. Fecht, *Mat. Sci. For.* **179-181**, 133 (1995).
- [91] J. Eckert, J. C. Holzer, C. E. Krill, and W. Johnson, *J. Mater. Res.* **7**, 1751 (1992).
- [92] S. Indris et al., *J. Phys. Chem. B* **109**, 23274 (2005).
- [93] M. Finger, Einfluss des kugelmahlens auf die katalytische und photokatalytische aktivität von nanokristallinem titandioxid am beispiel der totaloxidation von kohlenwasserstoffen, 2003, Diploma thesis, University of Hannover.
- [94] S. Brunauer, P. H. Emmett, and E. Teller, *J. Am. Chem. Soc.* **60**, 309 (1938).
- [95] C. P. Slichter, *Principles of Magnetic Resonance*, Springer - Verlag, Berlin Heidelberg, 1978.
- [96] C. Dyrek and R. N. Schindler, *Z. Naturforsch. N. F.* **32A**, 501 (1977).
- [97] E. M. Serwicka, *Z. Phys. Chem.* **166**, 249 (1990).

BIBLIOGRAPHY

- [98] S. Indris, *Perkolation von Grenzflächen in nanokristallinen keramischen Kompositen. Li-Ionenleitfähigkeit und ^7Li -NMR-Relaxation*, PhD thesis, University of Hannover, 2001.
- [99] Hewlett Packard, *Operation and Service Manual. Model 4192A LF Impedance Analyzer*, 1986.
- [100] M. Honda, *The Impedance Measurement Handbook. A Guide to Measurement Technology and Techniques*, Hewlett Packard, 1986.
- [101] A. K. Jonscher, *Nature* **267**, 673 (1977).
- [102] K. L. Ngai, *J. Non-Cryst. Solids* **203**, 232 (1996).
- [103] C. A. Angell, *Chem. Rev.* **90**, 523 (1990).
- [104] W. Puin, *Ionendynamik in nanokristallinem CaF_2 - untersucht mit NMR- und Impedanzspektroskopie*, PhD thesis, University of Hannover, 1993.
- [105] R. S. Berry, S. A. Rice, and J. Ross, *Physical Chemistry*, Oxford University Press, 2000.
- [106] V. E. Henrich, G. Dresselhaus, and H. J. Zeiger, *Phys. Rev. Lett.* **36**, 1335 (1976).
- [107] L. A. Bursill and D. J. Smith, *Nature* **309**, 319 (1976).
- [108] B. A. Boukamp, *Equivalent Circuit, Users Manual*, University of Twente, 1989.
- [109] L. Onsager, *Phy. Rev.* **65**, 117 (1944).
- [110] M. Miyauchi, A. Nakajima, A. Fujishima, K. Hashimoto, and T. Watanabe, *Chem. Mater.* **12**, 3 (2000).
- [111] A. N. Shultz et al., *Surf. Sci.* **339**, 114 (1995).
- [112] L.-Q. Wang, D. R. Baer, and M. H. Engelhard, *Surf. Sci.* **320**, 295 (1994).
- [113] L.-Q. Wang, D. R. Baer, M. H. Engelhard, and A. N. Shultz, *Surf. Sci.* **344**, 237 (1995).

BIBLIOGRAPHY

- [114] V. E. Henrich, G. Dresselhaus, and H. J. Zeiger, *Phys. Rev. B* **17**, 4908 (1978).
- [115] Y. Luo and D. F. Ollis, *J. Cat.* **163**, 1 (1996).
- [116] L. Cao et al., *J. Cat* **196**, 253 (2000).
- [117] S. Sitkiewitz and A. Heller, *New J. Chem.* **20**, 233 (1996).
- [118] A. V. Voronstov, E. N. Kurkin, and E. N. Savinov, *J. Cat.* **186**, 318 (1999).
- [119] A. Haeger, O. Kleinschmidt, and D. Hesse, *Chem. Eng. Technol.* **27**, 1019 (2004).
- [120] R. Amade et al., *Phys. Chem. Chem. Phys.* **8**, 777 (2006).
- [121] R. H. Friend and A. D. Yoffe, *Adv. Phys.* **36**, 1 (1987).
- [122] U. Hotje, R. Wartchow, and M. Binnewies, *Z. Anorg. Allg. Chem.* **631**, 403 (2005).

Curriculum vitae

Personal

Name : Roger Amade Rovira
Date and Place of Birth : October 24, 1979, Barcelona, Spain
Nationality : Spanish

Education

1985-1997 Primary, Secondary and High School in Barcelona, Spain
1997-2002 Student of Chemistry at the University of Barcelona (UB), Spain
07/02 Diploma in Chemistry
09/02-present PhD Student at the University of Hannover, Institute of Physikalische Chemie und Elektrochemie

Study Abroad

09/95-07/96 Exchange student at the Rockbrook Park School in Dublin, Ireland
02/02-08/02 Erasmus student at the University of Hannover, Germany

